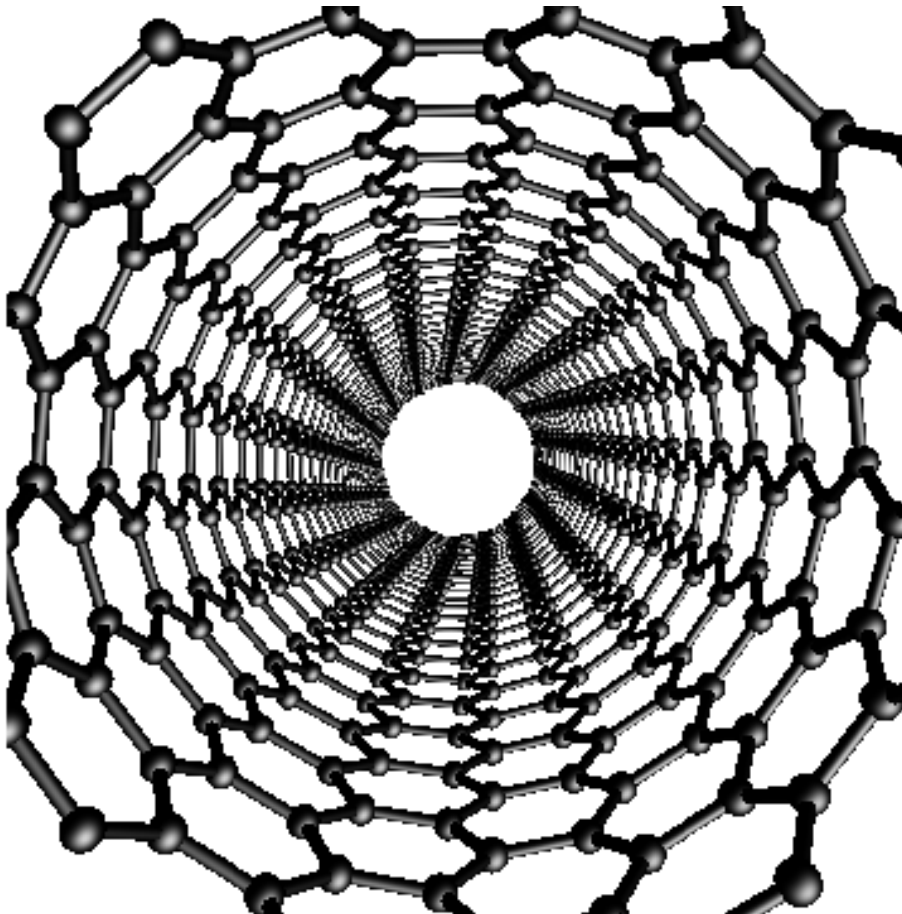


**Phonon-Induced Ultrafast Relaxation Processes and
Local Enhancement of Electric Fields:
A Theoretical Work on Semiconducting Carbon
Nanotubes and Nanostructured Electrodes**

by Christopher Köhler



**Phonon-Induced Ultrafast Relaxation Processes and
Local Enhancement of Electric Fields:
A Theoretical Work on Semiconducting Carbon
Nanotubes and Nanostructured Electrodes**

**Vorgelegt von Diplom-Physiker
Christopher Köhler
aus Erfurt**

von der Fakultät II – Mathematik und Naturwissenschaften
der Technischen Universität Berlin
zur Erlangung des akademischen Grades
Doktor der Naturwissenschaften

— Dr. rer. nat. —
genehmigte Dissertation

Promotionsausschuss

- Vorsitzender: Prof. Dr. rer. nat. Marga Cornelia Lensen, TU Berlin
1. Gutachter: Prof. Dr. rer. nat. Andreas Knorr, TU Berlin
2. Gutachter: Prof. Dr. rer. nat. Ermin Malić, Chalmers University of Technology

Tag der wissenschaftlichen Aussprache: 11.09.2015

Berlin, 2016
D 83

Abstract

This thesis studies ultrafast relaxation processes in semiconducting single-walled carbon nanotubes (SWCNTs) related to the fundamental process of photoluminescence excitation (PLE) and pump-probe experiments. Using carbon nanotube Bloch equations within the density matrix formalism we resolve ultrafast relaxation dynamics in momentum and time. This microscopic view elucidates the pathway of optically generated non-equilibrium carriers via intra- and intersubband scattering with optical and acoustic phonons approach to equilibrium within the lowest lying conduction subbands. Our analytical solutions of the Boltzmann-like scattering equations have successfully explained the influence of the tube intrinsic intersubband gap and subband curvature. In addition, the derived tube and phonon-mode specific electron-phonon matrix elements emphasize the influence of the coupling strength. Our model demonstrates that intersubband scattering is only possible with a sufficiently large energy provided by an optical phonon mode. Furthermore, we show that these optical phonons dominate during the intra-subband relaxation within the first hundred femtoseconds, while acoustic phonons with their small continuous energy primarily govern the relaxation towards equilibrium. The derived dynamics enabled us to extract relaxation times that exhibited clearly different timescales: processes driven by optical phonons occur within a few hundred femtoseconds, while those driven by acoustic phonons acting towards the band edge take up to a few picoseconds. Compared to experimental pump-probe studies on semiconducting SWCNTs, we find that the calculated relaxation times in the picosecond range fit very well with the observed initial decay time from the measured multiexponential differential transmission curves. Using our theoretical model we ascribed the observed picosecond relaxation time to intraband scattering about the band edge with acoustic phonons. Our approach allows us to study a large number of nanotubes, predicting a strong diameter and a weak chirality dependence of the relaxation times. A recent pump-probe study tuning the excitation and probe energy resonant around the optical transitions E_{22} and E_{11} observed a slowing-down of probing towards E_{11} in excellent agreement with our model.

We also studied the effects of field enhancements of nanostructured hybrid electrode surfaces that has been fruitfully utilized to analyze biological systems in surface-enhanced Raman (SE(R)R) spectroscopy studies. The complete Maxwell equations were solved using finite-element methods with a view toward topology optimization for field enhancement in experimentally investigated hybrid systems. With field distribution calculations we comprehensively describe the observed effects in SE(R)RS experiments for probe-molecules adsorbed to a multilayered (Ag – SiO₂ – Pt) electrode. Our results have enabled experimentalists to understand the nature of defects in the Pt film, which generate localized surface plasmons (LSPs) and field hot spots rising the average SE(R)RS enhancement to approx. 80%. Our model successfully predicted a recent experimental study on a semiconductive nanostructured titanium dioxide (TiO₂) electrode. The observed rising enhancement factor dependence on the anodization voltage may be straightforwardly rationalized from our calculations revealing that the this trend originates from the increasing anisotropy in the surface morphology.

In summary, this thesis contributes to the understanding of the fundamental PLE process and also unfolds the relevant phonon scattering channels of the observed relaxation time behavior in two-color pump-probe studies by affording microscopically resolved relaxation dynamics in semiconducting single-walled carbon nanotubes. Additionally, our field enhancement calculations of nanostructured electrodes reveal the underlying mechanisms that shall enable the optimization of hybrid devices for surface chemistry and biological application.

Zusammenfassung der Dissertation

*Phonon-Induced Ultrafast Relaxation Processes and Local Enhancement of Electric Fields:
A Theoretical Work on Semiconducting Carbon Nanotubes and Nanostructured Electrodes*

Die vorgelegte Dissertation beschäftigt sich mit ultraschnellen Relaxationsprozessen in halbleitenden einwandigen Kohlenstoffnanoröhrchen (SWCNTs) und trägt bei zum Verständnis des fundamentalen Prozesses der Photolumineszenz-Anregung sowie korrespondierenden Pump-Probe-Experimenten.

Durch die Herleitung von Kohlenstoffnanoröhrchen-Bloch-Gleichungen, die auf dem Formalismus der Dichtematrix basieren, wird eine in Impuls und Zeit aufgelöste ultraschnelle Relaxationsdynamik erzeugt. Die mikroskopische Betrachtungsweise erlaubt es den Bewegungsverlauf von optisch angeregten Nichtgleichgewichts Ladungsträgern ins Gleichgewicht nachzuvollziehen. Dieser wird von Intra- und Intersubband-Streuprozessen mit optischen und akustischen Phononen innerhalb der energetisch niedrigsten beiden Leitungsbänder bestimmt. Die analytischen Lösungen der Boltzmann-ähnlichen Streugleichungen erlauben die Interpretation der Relaxationsdynamik, durch die jedem Nanoröhrchen eigene Bandlücke und Krümmung der Subbänder. Darüber hinaus wird mittels der spezifischen Nanoröhrchen und der Phononenmoden hergeleiteten Elektron-Phonon-Matrixelemente der Einfluss der Kopplungsstärke hervorgehoben. Unser Modell zeigt auf, dass Intersubband-Streuung nur mit einer ausreichend großen Energie möglich ist, wie sie von einer optischen Phononenmode zur Verfügung gestellt wird. Weiterhin wird gezeigt, dass jene optischen Phononen bei der Intersubband-Relaxation während der ersten hundert Femtosekunden dominieren, während akustische Phononen durch ihre kleine kontinuierliche Energie in erster Linie die Relaxation ins Gleichgewicht führen. Die numerisch simulierte Dynamik ermöglicht es, Relaxationszeiten zu extrahieren, die deutlich unterschiedliche Zeitskalen aufweisen: Durch optische Phononen getriebene Prozesse treten innerhalb weniger hundert Femtosekunden auf, während die durch akustische Phononen in Richtung Bandkante ablaufenden Relaxationszeiten bis zu einigen Pikosekunden reichen. Im Vergleich zu experimentellen Pump-Probe-Studien an halbleitenden SWCNTs stellt sich heraus, dass die berechneten Relaxationszeiten im Bereich von Pikosekunden sehr gut mit der beobachteten anfänglichen Abklingzeit der gemessenen multi-exponentiellen differentiellen Transmissionskurven übereinstimmen. Mit unserem theoretischen Modell können wir die beobachtete Pikosekunden-Relaxationszeit Intraband-Streuprozessen mit akustischen Phononen nahe der Bandkante zuordnen. Unser Ansatz ermöglicht es uns darüber hinaus, eine große Anzahl von Nanoröhrchen zu studieren, woraus sich die Vorhersage einer starken Durchmesser- und einer schwachen Chiralitätsabhängigkeit der Relaxationszeiten ergibt. In einer aktuellen Pump-Probe-Studie, in der die Pump- und Probe-Energie resonant um die optischen Übergänge E_{22} und E_{11} variiert wurde, konnte eine Verlangsamung der Relaxationszeiten bei der Ausrichtung der Probe-Energie zu E_{11} beobachtet werden, was hervorragend mit unserem Modell übereinstimmt.

Desweiteren wurden die Auswirkungen von Feldverstärkungen an nanostrukturierten Oberflächen von Hybridelektroden untersucht, die erfolgreich eingesetzt werden können, um biologische Systeme in oberflächenverstärkten Raman-(SE(R)R)-Spektroskopie-Studien zu analysieren. Die

vollständigen Maxwell-Gleichungen wurden hierbei unter Verwendung von Finite-Elemente-Methoden im Hinblick auf die Optimierung der Topologie zur Feldverstärkung in den experimentell untersuchten Hybridsystemen gelöst. Mit Berechnungen zur elektrischen Feldverteilung beschreiben wir ausführlich die beobachteten Effekte in SE(R)RS-Experimenten für Probenmoleküle, adsorbiert an einer mehrschichtigen (Ag – SiO₂ – Pt) Elektrode. Unsere Ergebnisse ermöglichten es den Experimentatoren, den Einfluß der Fehlstellen in der Pt-Film-Oberfläche zu verstehen, die ihrerseits lokalisierte Oberflächenplasmonen (LSPs) und Field Hotspots erzeugten, wodurch die durchschnittliche SE(R)RS-Verstärkung 80 % erreichte. Das entwickelte Modell wurde daraufhin erfolgreich in einer fortführenden aktuellen experimentellen Studie an halbleitenden nanostrukturierten Titandioxid (TiO₂) Elektroden erweitert. Die beobachtete ansteigende Verstärkung in Abhängigkeit von der Anodisierungsspannung kann direkt aus den Berechnungen abgeleitet werden, wobei sich herausstellt, dass dieser Trend der zunehmenden Anisotropie der Oberflächenmorphologie zu Grunde liegt.

Danksagungen

Zuvorderst bin ich selbstverständlich meinem Doktorvater Andreas Knorr zu Dank verpflichtet. Sein steter Glauben an das Gelingen und den Erfolg dieser Arbeit waren für mich mindestens ebenso wichtig, wie sein praktischer Rat und sein Einsatz zur weitergehenden Finanzierung meiner wissenschaftlichen Studien. Es gehört sicher zu den inneren Gesetzmäßigkeiten eines jeden Promotionsvorhabens, dass man als Doktorand erst zum Zeitpunkt der mühevollen Fertigstellung der eigenen Arbeit so recht zu begreifen beginnt, von welcher richtungsweisenden und in vielerlei Hinsicht sogar vorentscheidenden Bedeutung, die einst in jugendlicher Unbekümmertheit getroffene Wahl des eigenen Doktorvaters tatsächlich war. Heute weiß ich, wäre meine Wahl anders ausgefallen, der Weg in der Physik wäre für mich ganz sicher nicht so weit zu gehen gewesen, wie unter seiner Führung und Anleitung.

Mein Dank gilt ebenso sehr Ermin Malic, der mich seit meinem ersten Kontakt mit Carbon Nanotubes über die Jahre hinweg hervorragend bei meiner Arbeit unterstützte. Zum einen hat er durch seine profunden Kenntnisse in CNTs erheblich dazu beigetragen, dass viele entscheidende Ideen der vorliegenden Arbeit überhaupt derart weit entwickelt werden konnten. Zum anderen bin ich mit Blick auf seine stets kollegiale und vertrauensvolle Betreuung mindestens ebenso dankbar für sein stets bewundernswert vorgelebtes Exempel an Zielstrebigkeit und klaren Arbeitsstrukturen, von dem ich in nicht unerheblichem Maße profitieren konnte.

Ebenso danke ich natürlich auch Frau Prof. Dr. Marga Lensen für ihre Bereitschaft zur Übernahme des Vorsitzes der Prüfungskommission.

Die Arbeit wäre in der vorliegenden Form nicht möglich gewesen, ohne die überaus hilfreiche Unterstützung und Kooperation vieler von mir überaus geschätzter Kollegen aus diversen Fachgebieten. Mein Dank gebührt deshalb den folgenden hier in hoffentlich verzeihlicher Kürze aufgezählten Kollegen:

Olga A. Dyatlova und Prof. Ulrike Woggon für die Pump-probe Studien und die daraus resultierende wechselseitige Stimulation von Theorie und Experiment.

Mein besonderer Dank gilt Prof. Dr. Inez Marita Weidinger, Hoang Khoa Ly und Xiao Xia Han und Prof. Dr. Peter Hildebrandt für die SE(R)R Experimente und die erfolgreiche Zusammenarbeit im Unicat Cluster. Prof. Dr. Hildebrandt möchte hierbei auch eigens noch einmal ausdrücklich für die von ihm ermöglichte Abschlußfinanzierung meiner Arbeit danken.

Antonio Setaro bin ich gleich in mehrfacher Hinsicht zu Dank verpflichtet: Einerseits ist es ihm mit seinen π -Hybriden gelungen, eine hilfreiche Brücke zwischen Feldverstärkungseffekten und Nanotubes zu schlagen, andererseits war er mir als Freund in seiner schier endlosen Hilfsbereitschaft und Ausdauer eine überaus wichtige Stütze, während der schwierigsten Phasen meiner Arbeit.

Dank gebührt zu gleichen Teilen auch Franz Schulze, Matthias-Rene Dachner, Sven Moritz Hein und Tobias Watermann, für die von ihnen bereitwillig übernommene Aufgabe des mühevollen Korrekturlesens.

Für eine wunderbare Zeit von immerhin sechs Jahren, mit zahllosen Hilfestellungen und Ratschlägen - nicht immer allein nur fachlicher Art - sei zudem der gesamten AG Knorr in aller Herzlichkeit gedankt:

Carsten Weber, Ermin Malic, Marten Richter, Frank Milde, Alexander Carmele, Julia Kabuß, Torben Winzer, Franz Schulze, Evgeny Bobkin, Thi Uyen-Khanh Dang, Felix Schlosser, Alexander Wilms, Sven Moritz Hein, Faris Kadi, Florian Wendler, Gunnar Berghäuser, Sandra Kuhn, Sverre Theuerholz, Pierce Munelly, Markus Krecik, Nicholas Naumann, Judith Specht, Anke Zimmermann und Michael Gegg. Insbesondere danke ich rückblickend meinem Freund Tobias Watermann, der mir in meinen Anfangstagen, noch während meiner Diplomzeit, den Weg zur Numerik in C++ wies, und mit dem ich bis heute immer noch die Freude am Fliegenfischen teile.

Frau Ludwig und Herrn Kolbow danke ich für ihr meisterhaftes und zuverlässiges Wirken an der Front der bürokratischen Abläufe.

Ein spezieller Dank geht auch an die Mitarbeiter der Fachbibliothek Physik Frau Inge Langenscheidt-Martens und Herrn Michael Jurk.

Zuletzt erlaube ich mir, meiner gesamten Familie aus tiefstem Herzen zu danken. Dieser Dank gilt natürlich vor allem meinen Eltern, Martina und Bernd und meinen Grosseltern Werner und Ilse sowie meiner Tante Christine, die mich über all die Jahre hinweg bedingungslos unterstützt haben. Nicht zu vergessen, möchte ich auch meinen in die Familie hinzugekommenen Schwiegereltern in St. Petersburg Vassily Makarowitsch und Ludmila für Ihre immer währende tatkräftige Unterstützung danken.

Unmöglich in Worte zu fassen ist hingegen der Dank, der meiner Frau Tatjana gebührt. Ihr und unseren beiden Söhnen, Roman und Daniel, soll diese Arbeit deshalb in Liebe gewidmet sein.

List of Publications

- O. A. Dyatlova, C. Köhler, P. Vogel, E. Malic, R. Jain, K. Tvrdy, M. Strano, E. Malic, A. Knorr, and U. Woggon
"Relaxation dynamics of carbon nanotubes of enriched chiralities"
Phys. Rev. B 90, 155402 (2014)
- C. Köhler, T. Watermann, and E. Malic
"Time- and momentum-resolved phonon-induced relaxation dynamics in carbon nanotubes"
J. Phys.: Cond. Matter 25 (2013)
- X. X. Han, C. Köhler, J. Kozuch, U. Kuhlmann, L. Paasche, A. Sivanesan, I. M. Weidinger, and P. Hildebrandt
"Potential-Dependent Surface-Enhanced Resonance Raman Spectroscopy at Nanostructured TiO_2 : A Case Study on Cytochrome b_5 "
Small Vol 9, 4175-4183 (2013)
- O. A. Dyatlova, C. Köhler, E. Malic, J. Gomis-Bresco, J. Maultzsch, A. Tsagan-Mandzhiev, T. Watermann, A. Knorr, and U. Woggon
"Scattering of electrons with acoustic phonons in single-walled carbon nanotubes"
Conference on Lasers and Electro-Optics (CLEO) (2012)
- C. Köhler, T. Watermann, and E. Malic
"Relaxation dynamics via acoustic phonons in carbon nanotubes"
Phys. Status Solidi (b) (2012)
- O. A. Dyatlova, C. Köhler, E. Malic, J. Gomis-Bresco, J. Maultzsch, A. Tsagan-Mandzhiev, T. Watermann, A. Knorr, and U. Woggon
"Ultrafast Relaxation Dynamics via Acoustic Phonons in Carbon Nanotubes"
Nano Lett. 12, 2249 (2012)
- K. Ly, C. Köhler, A. Fischer, J. Kabuß, F. Schlosser, M. Schoth, A. Knorr, and I. M. Weidinger
"Induced surface enhancement in coral Pt island films attached to nanostructured Ag electrodes"
Langmuir 28, 5819 (2012)
- C. Köhler, T. Watermann, A. Knorr, and E. Malic
"Microscopic study of temporally resolved carrier relaxation in carbon nanotubes"
Phys. Rev. B 84, 153407 (2011)
- E. Malic, E. Bobkin, T. Winzer, C. Köhler, and A. Knorr,
"Microscopic theory of ultrafast processes in carbon nanomaterials"
Proc. SPIE 7937, 79371R (2011)

List of Conference Contributions

- C. Köhler, T. Watermann, E. Malic, A. Knorr
"Theory of Temporally Resolved Electron-Phonon Relaxation Dynamics in Carbon Nanotubes"
2 nd Polish-German Workshop on the Optical Properties of Nanostructures; 14 - 16 February 2011; Breslau/Wroclaw, Poland
- K Ly, A. Fischer, C. Köhler, J. Kabuß, F. Schlosser, A. Knorr, P. Hildebrandt, I. M. Weidinger
"SER active Pt-Ag Hybrid Device for Probing Pt-Catalyzed Reactions."
International Symposium on Relations between Homogeneous and Heterogeneous Catalysis; 11 - 16 September 2011; FU Berlin, Germany
- C. Köhler, T. Watermann, E. Malic, A. Knorr
"Theory of temporally resolved electron-phonon relaxation dynamics in carbon nanotubes "
International Winterschool (IWEPM12); March 2012; Kirchberg, Austria
- Olga A. Dyatlova, Christopher Köhler, Ermin Malic, Jordi Gomis-Bresco, Janina Maultzsch, Andrey Tsagan-Mandzhiev, Tobias Watermann, Andreas Knorr, Ulrike Woggon
"Scattering of electrons with acoustic phonons in single-walled carbon nanotubes" Conference on Lasers and Electro-Optics (CLEO); May 2012; San Jose, USA

Contents

1	Preliminaries	1
2	Theoretical Foundation of the Dynamical Equations	5
2.1	Hamiltonians Introducing the Model System	6
2.2	Calculation of the Dynamics within the Heisenberg Picture	8
2.2.1	Free Carrier and Optical Coupling	8
2.2.2	Relaxation Dynamics with Electron - Phonon Scattering Rates	9
2.2.3	Boltzmann Scattering Terms - Fermi's Golden Rule and Pauli Blocking	12
2.3	Analytical Solution of the Dynamics	15
2.3.1	Scattering Prefactors and Jump Amplitudes - The Influence of Subband Curvature -	15
2.3.2	Electron Dynamics	16
2.4	At a Glance	17
3	Launching the Carbon Nanotube	19
3.1	Microscopic Properties of Carbon Nanotubes: Electronic, Phononic and Optical Features	20
3.1.1	Electronic System	20
3.1.2	Entering the Reciprocal Space - On the Way to One Dimension	24
3.1.3	From Graphene to Carbon Nanotubes - Reducing the Dimension through Zone-Folding	25
3.1.4	Density of states (DOS) in One Dimension	32
3.1.5	Family Patterns: Metallic versus Semiconducting CNTs	33
3.2	Phonon Modes - Optical and Acoustic Dispersions	34
3.3	Matrix Elements Describing the Coupling	35
3.3.1	Between External Fields and the Nanotube: Optical Matrix Element (OME)	35
3.3.2	Within the Nanotube: Electron-Phonon Coupling (EPC)	36
3.4	At a Glance	38
4	Relaxation Dynamics in Semiconducting Nanotubes	39
4.1	Experimental Techniques on Nanotubes	40
4.1.1	Photoluminescence Excitation (PLE)	40

CONTENTS

4.1.2	Ultrafast Pump-Probe Experiments	43
4.1.3	Dielectric Screening in Single Walled Carbon Nanotubes	47
4.2	Carrier Relaxation Dynamics via Electron-Phonon Scattering	48
4.2.1	Simulation of the Excitation	48
4.2.2	Relaxation Channels in Semiconducting Carbon Nanotubes	49
4.2.3	Intrasubband Scattering: One-Color Pump-Probe	51
4.2.4	Excitation Energy	54
4.2.5	Dependence on Diameter and Chirality	55
4.3	Intra- and Intersubband Dynamics-Two Color Pump-Probe Studies	57
4.3.1	Relaxation Dynamics of the Semiconducting (23,0) Zig-Zag Tube	57
4.3.2	Excitation Energy	60
4.3.3	Diameter and Chirality Dependence	63
4.4	An Experimental Motivated Two Color Pump-Probe Study	68
4.4.1	Modeling the Experiment	68
4.4.2	Detuning of the Probe Energy	70
4.4.3	Detuning of the Pump Energy	72
4.5	At a Glance	73
5	Field Enhancement Calculations of Plasmonic and Non-Plasmonic Electrodes	75
5.1	Enhancement of the Electric Field	76
5.1.1	Time-Harmonic Maxwell Equations	76
5.1.2	An Electronic Gas in Motion: Collective Behavior of Electronic Density Fluctuations	77
5.1.3	Classification of Plasmons	79
5.2	Numerical Simulation of Field Enhancement using the Finite Element Method	80
5.2.1	Simulation of a Single Nanosphere	80
5.2.2	Two Coupled Multilayered Nanospheres	81
5.3	Surface Enhanced Resonant Raman Spectroscopy	81
5.4	A Nanostructured Multilayer Electrode : Field Enhancement via Plasmonic Material Features	83
5.5	A Study of a Nanostructured (TiO ₂) Electrode: Field Enhancement by Raising the Anisotropy of the Morphology	86
5.6	At a Glance	89
6	Photoluminescence Enhancement of CNTs via Coupling to Noble Metal Nanoparticles	
	-An Outlook-	91
6.1	π -Hybrids Exhibiting Novel Properties of Enhancement Mechanisms	92
6.2	Discussion of the Origins of the Observed Effects	94
6.2.1	Enhancement Effect	95
6.2.2	Energy Shift of the E_{11} Transition	96

6.3	At a Glance	97
7	Conclusion	99
8	Appendix	103
8.1	Approximations	103
8.1.1	Instantaneous Scattering-Markovian Dynamics	103
8.1.2	Bath Approximation for the Phononic System	104
8.2	Phonon Dynamics	105
8.2.1	Optical Modes	105
8.2.2	Acoustic Modes	106
8.3	Solution of the δ -Function	107
8.4	Basic Constants Used in the Thesis	108

CONTENTS

If it disagrees with experiment, it's wrong. In that simple statement is the key to science. It doesn't make any difference how beautiful your guess is, it doesn't matter how smart you are who made the guess, or what his name is... If it disagrees with experiment, it's wrong. That's all there is to it [1].

R. P. Feynman

1

Preliminaries

Carbon nanotubes are low-dimensional carbon nanostructures [2], first synthesized and observed 1991 by Iijima [3]. They are viewed as rolled-up cylinders of graphene of sp^2 bonded carbon atoms [4] being hollow in contrast to the earlier invented carbon fibers. While their length can reach up from micro- to centimeters their diameters are ranging down to one nanometer, CNTs bridge the quantum microscopic world with the macroscopic one. Through this confinement the carriers have only the possibility to move freely along the cylindrical tube axis [2]. Therefore, they are a perfect one-dimensional system to study basically the interactions between electrons and phonons for example. The rolling up of CNTs imposes additional periodic boundary conditions to the wave functions implied in the systems, selecting only some of the electronic states that are present in graphene. Thus, even if graphene is a semi-metal, CNTs can be either metallic or even semiconducting, depending upon the chiral vector \mathbf{c} . Semiconducting CNTs exhibit emission of photons due to the band-to-band radiative recombination of the electron-hole pair. This makes them very relevant for optoelectronic fundamental and applied research [5]. Furthermore, they inherit from graphene its exceptional properties: They have a remarkably high stiffness, extremely good conduction and electron mobility [6, 7, 8]. Carbon fibers and graphite had been employed since the 1970s due to their strength-to-weight ratio in e.g. manufacturing fly rods [9] and aircraft construction [10]. Recently carbon fibers have been replaced in the F-35 Lightning II stealth fighter by CNTs, since they are "widely considered one of the strongest materials ever invented - several times stronger than carbon fiber reinforced plastic (CFRP), yet lighter by about 25-30%" [10]. Carbon nanotubes are further used in miniaturizing electronics designing novel field-effect transistors [11, 12] or serving as data storage devices [13]. Time resolved photoluminescence spectroscopy is one of the most important techniques of characterizing carbon nanotubes [14]. In this sense a thorough microscopic understanding of the ultrafast relaxation dynamics of non-equilibrium carriers is a

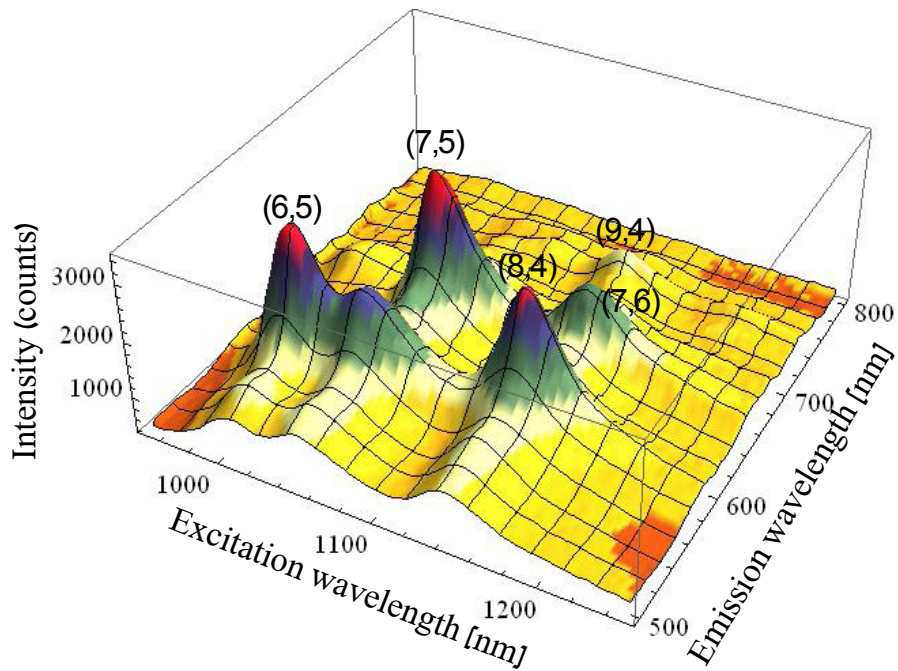


Figure 1.1: The process of photoluminescence excitation (PLE) given by photo absorption at the E_{22} and photo emission at the E_{11} transition. These transitions being unique for a certain (n_1, n_2) species, allows the clear identification of different CNTs. Through the confinement in one dimension the PLE chart shows sharp peaks for the different chiralities. The measured intensity of the emission is plotted over the excitation and emission wavelength. The PLE map uncover the semiconducting $(7,5)$, $(7,6)$, $(6,5)$, $(9,4)$ and $(8,4)$ CNTs contained in the sample.

prerequisite for the creation of optoelectronic devices based on CNTs [15, 16]. From our work we ruled out which relaxation channels for the phonon-induced non-radiative relaxation dynamics are relevant and how they can be addressed to the observed relaxation times of corresponding pump-probe experiments [16, 17]. Besides ultrafast relaxation dynamics of nanostructures, field enhancement via plasmons for example is another current prospering research topic in physics. Possible material applications are developed utilizing enhancement mechanisms between solids on the nanoscale like quantum dots, graphene or carbon nanotubes with noble metal nanoparticles of different shapes. Combining a metal nanosphere with one-dimensional quantum dots led to the novel concept of the SPASER [18]. Bringing a two-dimensional graphene layer together with plasmonic nanostructures increased the efficiency of photo-detectors up to 20 times [19]. In novel π -hybrid structures from Au nanorods with single walled carbon nanotubes [20] the quantum yield within the photoluminescence process was observed to be 18 times larger in comparison to the usually lower one of the "naked" tube. Surface enhanced Raman spectroscopy (SE(R)RS) is a well established method to detect biological molecules [21]. Since the Raman signal of these molecules

is in general very low, the generation of high electric fields at the surface of an underlying electrode is the key-feature for an enhanced scattered Raman signal. Therefore, the knowledge of the origin and mechanism of such enhancement effects is pointing the way how to nanostructure and optimize these electrodes.

The thesis is structured as follows: In chapter 2 we explain the theoretical basics using density matrix theory and derive analytically the equations of motion for the polarization and occupation probabilities leading to a dynamical picture. Chapter 3 introduces the structural and electronic properties of carbon nanotubes and present their optical and electron-phonon matrix elements. The following chapter 4 contains our work on the phonon-induced relaxation dynamics of semiconducting CNTs contributing to the understanding of photoluminescence excitation and pump-probe spectroscopy experiments. We simulate the intraband dynamics of optically excited non-equilibrium with optical and acoustic with a single-band model and compare our results with experimental differential transmission curves. As a result we assign the experimental fast relaxation time component in the picosecond range to intraband scattering with acoustic phonons. We further extend the system to a two-band model enabling intersubband scattering channels with optical phonons. From this, we investigate the full relaxation dynamics in recent two-color pump-probe studies uncovering the underlying microscopic scattering mechanisms leading to the observed dependencies for tuning the pump and probe energies around the optical E_{22} and E_{11} transitions. Chapter 5 introduces the reader to field enhancements of nanostructured electrodes. The experimental observed effects are rationalized by the performed calculations by solving the full Maxwell equations within a finite-element method. We reveal two effects: field enhancement through the excitation of localized surface plasmons as also the influence of increasing the anisotropy of the surface morphology. The last chapter 6 brings the both topics of this thesis together. Providing an outlook on forward going investigations by introducing novel π -hybrids of Setaro et al. , composed of gold nanorods attached to carbon nanotubes. The experimentally observed specific enhancements within PLE measurements and the measured blue-shift are discussed on the gained insights of our investigations in the previous chapters.

2

Theoretical Foundation of the Dynamical Equations

To obtain insight into the relaxation processes taking place in the relevant conduction subbands between the process of absorption and emission of the photoluminescence excitation, cp. Chap. 4, one would like to know the dynamics of the excited electrons, i.e. the temporal evolution of their occupation probabilities. In this thesis we make use of the density matrix theory. Established by John v. Neumann [22] in the year 1927 with "the translation of statistical mechanics concepts into the language of quantum mechanics" [23] it was also introduced independently by Lev. D. Landau and Felix Bloch [24, 25]. It provides for example the calculation of microscopic quantities like the polarization and occupation probabilities for electrons and phonons. From the interaction of electrons and phonons the dynamics of both quasiparticles can be calculated and studied. The results give access to time and momentum resolved carrier dynamics. The displayed relaxation behavior includes how the carrier distributions scatter from one point of energy to the next under phonon absorption or emission within energy and momentum conserving Markovian processes. From the dynamics of the carrier occupation probabilities we further extract relaxation times which can be compared to experiment. The relaxation times depend on the electronic structure of the solid, which in our case is the band structure of carbon nanotubes and the coupling between the interacting quasiparticles. The scattering partners for the carrier relaxation being optical and acoustic phonons leading to relaxation times ranging from femto- to picoseconds, respectively.

2.1 Hamiltonians Introducing the Model System

The investigation of the temporal evolution of the microscopic polarization, electronic and phonon occupations are based on the Hamilton operator in second quantization [26, 27]

$$H = H_{\text{car}} + H_{\text{phon}} + H_{\text{car-phon}} + H_{\text{car-lf}}, \quad (2.1)$$

including the free-carrier H_{car} and free phonon H_{phon} parts, the carrier-phonon interaction $H_{\text{car-phon}}$ and carrier light field coupling $H_{\text{car-lf}}$ within a semi-classical treatment.

The free contributions state:

$$H_{\text{car}} + H_{\text{phon}} = \hbar \left(\sum_{\lambda \mathbf{k}} \omega_{\mathbf{k}}^{\lambda} a_{\lambda \mathbf{k}}^{\dagger} a_{\lambda \mathbf{k}} + \sum_{\gamma \mathbf{q}} \omega_{\mathbf{q}}^{\gamma} b_{\mathbf{q} \gamma}^{\dagger} b_{-\mathbf{q} \gamma} \right), \quad (2.2)$$

with the unperturbed free electron and phonon energies $\epsilon_{\mathbf{k}}^{\lambda} = \hbar \omega_{\mathbf{k}}^{\lambda}$ and $\epsilon_{\mathbf{q}}^{\gamma} = \hbar \omega_{\mathbf{q}}^{\gamma}$, respectively. The operators $a_{\lambda \mathbf{k}}^{\dagger}$ and $a_{\lambda \mathbf{k}}$ create and annihilate an electron with the wave vector \mathbf{k} in an electronic subband λ . Similarly, $b_{\mathbf{q} \gamma}^{\dagger}$ and $b_{-\mathbf{q} \gamma}$ create and annihilate a phonon in the mode γ with the wave vector \mathbf{q} . These operators have to satisfy the following anti-commutator relations for fermions (e.g. electrons or holes):

$$\left[a_x, a_y \right]_{+} = \delta_{xy} \quad \left[a_x^{(\dagger)}, a_y^{(\dagger)} \right]_{+} = 0, \quad (2.3)$$

and the commutator relations for bosons (e.g. phonons):

$$\left[b_x, b_y \right]_{-} = \delta_{xy} \quad \left[b_x^{(\dagger)}, b_y^{(\dagger)} \right]_{-} = 0, \quad (2.4)$$

whereby the commutator is defined as $\left[b_x, b_y \right]_{-} = b_x b_y - b_y b_x$ and the anti-commutator as $\left[a_x, a_y \right]_{+} = a_x a_y + a_y a_x$. To couple the system to an external light field (e.g. a laser) a semi-classical carrier-light coupling is used which will now be derived in more detail following the book of Scully [28]:

The carrier light field Hamiltonian is based on the fundamental interaction of a carrier, for example an electron in an external electromagnetic field expressed by the gauge invariant vector $\mathbf{A}(\mathbf{r}, t)$ and scalar $\phi(\mathbf{r}, t)$ potential called minimal coupling:

$$\mathfrak{H}_{\text{car-lf}} = \frac{1}{2m_e} [\mathbf{p} - e_0 \mathbf{A}(\mathbf{r}, t)]^2 + e_0 \phi(\mathbf{r}, t) + V(\mathbf{r}), \quad (2.5)$$

with the electronic charge e_0 and mass m_e (being the rest mass, since the calculations are non-relativistic). The canonical momentum operator is denoted by $\mathbf{p} = -i\hbar \nabla_{\mathbf{r}}$ [29] and $V(\mathbf{r})$ is an internal electrostatic potential being the atomic binding potential of carbon in case of nanotubes (graphene respectively). Choosing the radiation gauge, i.e. $\nabla \cdot \mathbf{A} = 0$ and $\phi = 0$ leads to the above mentioned unperturbed carrier Hamiltonian in first quantization $\mathfrak{H}_{\text{car}} = \frac{\mathbf{p}^2}{2m_e} + V(\mathbf{r})$ and

the atom-field part $\mathcal{H}_{\text{car-lf}} = -\frac{e_0}{m_e} \mathbf{p} \mathbf{A}(\mathbf{r}, t) + \frac{e_0^2}{2m_e} \mathbf{A}(\mathbf{r}, t)^2$. Under the assumption that $\mathbf{A}(\mathbf{r}, t)$ takes only small values one can neglect the quadratic term $\mathbf{A}(\mathbf{r}, t)^2$. Applying the formalism of second quantization [30]:

$$\langle \Psi^+(\mathbf{r}, t) | -\frac{e_0}{m_e} \mathbf{p} \mathbf{A}(\mathbf{r}, t) | \Psi(\mathbf{r}, t) \rangle, \quad (2.6)$$

under the usage of the Heisenberg field operators

$$\Psi^{(\dagger)}(\mathbf{r}, t) = \sum_{\lambda \mathbf{k}} \Phi_{\lambda \mathbf{k}}^{(*)}(\mathbf{r}) a_{\lambda \mathbf{k}}^{(\dagger)}(t), \quad (2.7)$$

leads to the semi-classical light matter Hamiltonian

$$H_{\text{car-lf}} = i\hbar \frac{e_0}{m_e} \sum_{\lambda \lambda'} \sum_{\mathbf{k} \mathbf{k}'} \mathbf{M}_{\mathbf{k} \mathbf{k}'}^{\lambda \lambda'} \mathbf{A}(t) a_{\lambda \mathbf{k}}^\dagger a_{\lambda' \mathbf{k}'}, \quad (2.8)$$

with the vector potential $\mathbf{A}(t)$ in dipole approximation. Within this approximation the photonic wave vector is assumed to be too small to transfer a momentum to the electrons. Therefore, only vertical ($\mathbf{k} = \mathbf{k}'$) optical transitions between the valence and conduction bands are considered. The vector potential $\mathbf{A}(\mathbf{r}, t)$ can be assumed to be position independent by fixing $\mathbf{r} = \mathbf{r}_0$, which is in the simplest case setting $\mathbf{r}_0 = 0$ and therefore $\mathbf{A}(\mathbf{r}, t) \approx \mathbf{A}(t)$. The optical matrix element $\mathbf{M}_{\mathbf{k} \mathbf{k}'}^{\lambda \lambda'} = \langle \Phi_{\mathbf{k}}^\lambda(\mathbf{r}) | \nabla_{\mathbf{r}} | \Phi_{\mathbf{k}'}^{\lambda'}(\mathbf{r}) \rangle$ expresses the transition between the electronic Bloch wave functions for a crystal with N atoms which in momentum space are given via:

$$\phi_{\mathbf{k}}^\lambda(\mathbf{r}) = \frac{1}{\sqrt{N}} \sum_{\mathbf{R}_j} e^{i\mathbf{k} \mathbf{R}_j} \varphi(\mathbf{r} - \mathbf{R}_j), \quad (2.9)$$

with \mathbf{R}_j running over all lattice vectors and φ being the atomic wave functions of carbon, cp. section 3.1.3.

The carrier-phonon interaction is described through

$$H_{\text{car-phon}} = \sum_{\lambda \lambda'} \sum_{\mathbf{k} \gamma \mathbf{q}} \left(g_{\mathbf{k} \mathbf{q}}^{\lambda \lambda' \gamma} a_{\lambda \mathbf{k} + \mathbf{q}}^\dagger a_{\lambda' \mathbf{k}} b_{\gamma \mathbf{q}} + h.c. \right), \quad (2.10)$$

with the electron-phonon matrix element $g_{\mathbf{k} \mathbf{q}}^{\lambda \lambda' \gamma}$. The general form of the carrier phonon interaction $H_{\text{car-phon}}$ and the free phonon Hamiltonian H_{phon} is independent from the mode (acoustic or optical) and from the coupling (via a deformation potential or the polar Fröhlich coupling) [31]. Since, within the described tight-binding approach, cp. section 3.1.3, the valence and conduction bands are assumed to be symmetric in the optically relevant region. We therefore estimate the dynamics of electrons and holes around the K -point to be identical.

2.2 Calculation of the Dynamics within the Heisenberg Picture

The dynamics of a microscopic quantity represented by a time-dependent operator $X = X(t)$ are calculated in the Heisenberg picture, i.e. the operators are time dependent while the spatial dependencies are included in the matrix elements which is expressed by letting the nabla operator $\nabla_{\mathbf{r}}$ act on the electronic wave functions $\phi_{\mathbf{k}}^{\lambda}(\mathbf{r})$. Applying the Ehrenfest Theorem [32] by considering the expectation value we yield the temporal evolution, i.e. the dynamics of the desired microscopic quantity:

$$d_t \langle X \rangle = \frac{1}{i\hbar} \langle [X, H]_- \rangle + \langle \partial_t X \rangle, \quad (2.11)$$

with the commutator relation $[X, H]_- := XH - HX$. Because the observables do not have an explicit time dependence the partial derivation vanishes. Equation (2.11) will be in the following referred to as the Heisenberg equation of motion.

2.2.1 Free Carrier and Optical Coupling

The dynamics for the free carrier energy and the interaction with an external field H_{car-lf} within the semi-classical treatment is calculated for the microscopic polarization $p_{\mathbf{k}} = \langle a_{i\mathbf{k}}^{\dagger} a_{j\mathbf{k}} \rangle$ and the population probabilities $\rho_{\mathbf{k}}^l = \langle a_{l\mathbf{k}}^{\dagger} a_{l\mathbf{k}} \rangle$ where i and j label the valence and conduction subbands V_s and C_s respectively with $s = 1, 2, \dots$, while l runs over both subband species. The polarization according to [31] is defined by creating an electron within the valence while annihilating one simultaneously in the conduction band. The dynamical equations reads:

$$d_t p_{\mathbf{k}} = -i\Delta\omega_{\mathbf{k}} p_{\mathbf{k}} + \Omega_{\mathbf{k}}^{C_s V_s} (\rho_{\mathbf{k}}^{V_s} - \rho_{\mathbf{k}}^{C_s}), \quad (2.12)$$

$$d_t \rho_{\mathbf{k}}^{C_s} = 2\Im \left\{ \left[\Omega_{\mathbf{k}}^{C_s V_s} \right]^* p_{\mathbf{k}} \right\} = -d_t \rho_{\mathbf{k}}^{V_s}, \quad (2.13)$$

with the band gap $\Delta\omega_{\mathbf{k}} = \left\{ \frac{\epsilon_{\mathbf{k}}^{C_s} - \epsilon_{\mathbf{k}}^{V_s}}{\hbar} \right\}$ and the Rabi frequency $\Omega_{\mathbf{k}}^{C_s V_s}(t) = i \frac{e_0}{m_e} \mathbf{M}_{\mathbf{k}}^{C_s V_s} \cdot \mathbf{A}(t)$.

In the following we will use the common abbreviation for the total time derivation $d_t x := \dot{x}$. Referring to the mirror symmetry between the valence and conduction bands in the vicinity of the K-point the equations for the population dynamics are assumed to be $\rho_{\mathbf{k}}^{C_s} = -\rho_{\mathbf{k}}^{V_s}$ with respect to the Fermi energy, which means that while electrons scatter via interacting with phonons towards the band edge of the conduction, holes scatter towards the band edge of the respective valence bands. Switching to the electron-hole picture the electron (hole) populations are identified with the populations of the conduction (valence) band $\rho_{\mathbf{k}}^e = \rho_{\mathbf{k}}^{C_s}$ and $\rho_{\mathbf{k}}^h = 1 - \rho_{\mathbf{k}}^{V_s}$ [33] leading to:

$$\dot{p}_{\mathbf{k}} = -i\Delta\omega_{\mathbf{k}} p_{\mathbf{k}} - i\Omega_{\mathbf{k}}^{C_s V_s} (1 - \rho_{\mathbf{k}}^e - \rho_{\mathbf{k}}^h). \quad (2.14)$$

Assuming that the density of electrons and holes in the conduction and valence bands are equal we define $\rho_{\mathbf{k}}^{C_s} := \rho_{\mathbf{k}}^e = \rho_{\mathbf{k}}^h$. With this, we have the equations for the polarization and electronic

occupations:

$$\dot{p}_{\mathbf{k}} = -i\Delta\omega_{\mathbf{k}}p_{\mathbf{k}} - i\Omega_{\mathbf{k}}^{C_s V_s}(1 - 2\rho_{\mathbf{k}}^{C_s}), \quad (2.15)$$

$$\dot{\rho}_{\mathbf{k}}^{C_s} = 2\Im\left\{\left[\Omega_{\mathbf{k}}^{C_s V_s}\right]^* p_{\mathbf{k}}\right\}, \quad (2.16)$$

for optical coupling between the valence and conduction bands. The further hole-phonon dynamic within the valence bands does not influence the electron-phonon scattering processes in the conduction bands (neglecting phonon induced dephasing processes, where the dynamic of the valence bands couples to the polarization) since it only affects the initial optical coupling process between the valence and conduction bands via the polarization.

2.2.2 Relaxation Dynamics with Electron - Phonon Scattering Rates

Including the electron-phonon interaction $H_{\text{car-phon}}$ the equations for the polarization and occupations, cp. Eq. (2.15 – 2.16) are expanded by scattering and dephasing terms $\dot{\rho}_{\mathbf{k}}^l|_{sc}$, $\dot{p}_{\mathbf{k}}|_{deph}$ describing the non-radiative relaxation dynamics during and after the non-linear optical excitation of the solid, cp. Eq. (2.17-2.18). It further allows to calculate the dynamics of the phonon occupations $n_q^\gamma = \langle b_{q\gamma}^\dagger b_{-q\gamma} \rangle$ for arbitrary phonon modes labeled by γ , cp. Eq. (2.19). In sum we get a system of coupled differential equations [34, 35]:

$$\dot{p}_{\mathbf{k}} = -i\Delta\omega_{\mathbf{k}}p_{\mathbf{k}} + i\Omega_{\mathbf{k}}^{C_s V_s}(1 - 2\rho_{\mathbf{k}}^l) - \dot{p}_{\mathbf{k}}|_{deph}, \quad (2.17)$$

$$\dot{\rho}_{\mathbf{k}}^l = 2\Im\left\{\left[\Omega_{\mathbf{k}}^{C_s V_s}\right]^* p_{\mathbf{k}}\right\} + \dot{\rho}_{\mathbf{k}}^l|_{sc}, \quad (2.18)$$

$$\dot{n}_{\mathbf{q}}^\gamma = \dot{n}_{\mathbf{q}}^\gamma|_{sc}. \quad (2.19)$$

Inserting the Hamiltonian for carrier-phonon interaction in Eq. (2.11) yields the equations of motion (EOM) of the respective dephasing and scattering terms leading to phonon assisted density matrices which can be solved under the Markov and factorization approximations. Phonon-assisted density matrices [36] are introduced by taking the expectation value of electron-phonon interaction Hamiltonian:

$$\langle H_{\text{car-phon}} \rangle = \sum_{\lambda\lambda'\mathbf{k}} \sum_{\gamma\mathbf{q}} \left[g_{\mathbf{k}\mathbf{q}}^{\lambda\lambda'\gamma} A_{\mathbf{k}+\mathbf{q}\mathbf{k}\mathbf{q}}^{\lambda\lambda'\gamma} + g_{\mathbf{k}\mathbf{q}}^{*\lambda\lambda'\gamma} E_{\mathbf{k}\mathbf{k}+\mathbf{q}\mathbf{q}}^{*\lambda\lambda'\gamma} \right]. \quad (2.20)$$

This defines the phonon assisted absorption and emission being of hermitian character, i.e. $A^* = E$. Throughout the thesis we will abbreviate the absorption and emission density matrices with:

$$A_{\mathbf{k}+\mathbf{q}\mathbf{k}\mathbf{q}}^{\lambda\lambda'\gamma} := \langle a_{\lambda\mathbf{k}+\mathbf{q}}^\dagger a_{\lambda'\mathbf{k}} b_{\gamma\mathbf{q}} \rangle \quad E_{\mathbf{k}\mathbf{k}+\mathbf{q}\mathbf{q}}^{\lambda\lambda'\gamma} := \langle a_{\lambda\mathbf{k}}^\dagger a_{\lambda'\mathbf{k}+\mathbf{q}} b_{\gamma\mathbf{q}}^\dagger \rangle. \quad (2.21)$$

They describe two microscopically different scattering processes: Absorption and Emission of a phonon by raising or lowering the energetic state and momentum of an electron. These processes are

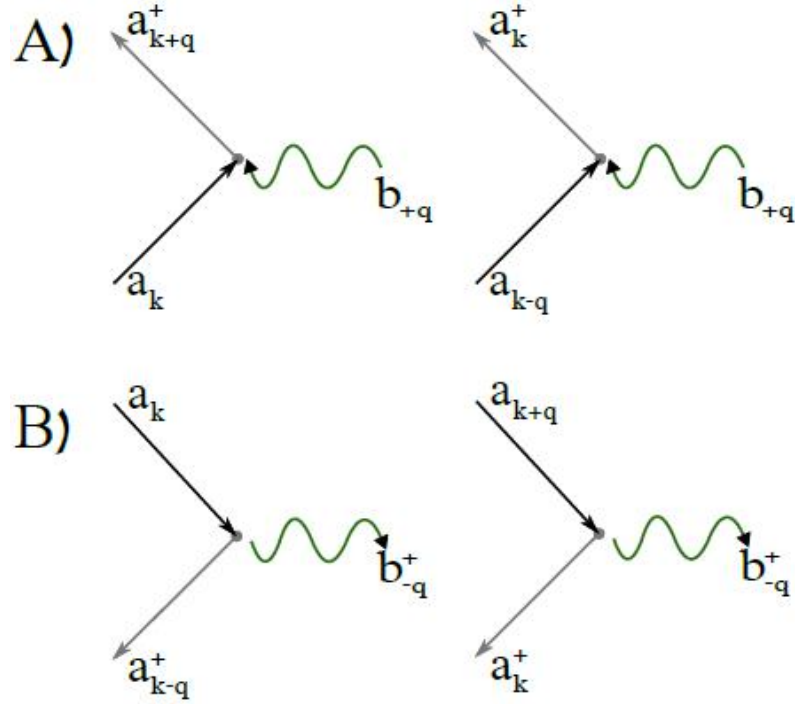


Figure 2.1: Scattering vertices between electrons and phonons: A) Absorption of a phonon ($+\mathbf{q}, +\hbar\omega$), leads to a lifting of the electron into a higher energy state and gaining positive momentum. B) The inverse scattering process of phonon emission ($-\mathbf{q}, -\hbar\omega$) lowers the electronic state by losing momentum.

usually visualized by a Vertex displaying the energy and momentum conservation of the respective process (see Ref. [30]), cp. Fig. 2.1. These mixed quantities lead to second order contributions which are obtained through repeated usage of Eq. (2.11). They will occur in the equations for the electronic populations and the dephasing of the polarization through phonon scattering. To emphasize the basic procedure for the following considerations we rewrite the assisted quantities in a more general way:

$$A_{\mathbf{123}}^{xyz} := \langle a_{x\mathbf{1}}^\dagger a_{y\mathbf{2}} b_{z\mathbf{3}} \rangle \quad E_{\mathbf{123}}^{xyz} := \langle a_{x\mathbf{1}}^\dagger a_{y\mathbf{2}} b_{z\mathbf{3}}^\dagger \rangle, \quad (2.22)$$

with xyz labeling the energies and $\mathbf{123}$ the electronic and phononic momenta. In first order the factorization of the assisted density matrices yields expectation values of one phononic creation and annihilation operator, i.e. coherent phonons:

$$\langle a_{x\mathbf{1}}^\dagger a_{y\mathbf{2}} b_{z\mathbf{3}} \rangle = \langle a_{x\mathbf{1}}^\dagger a_{y\mathbf{2}} \rangle \langle b_{z\mathbf{3}} \rangle \delta_{xy} \delta_{\mathbf{12}}. \quad (2.23)$$

Considering a homogeneous system the bosonic wave vector equals zero, i.e. no momentum can be transferred to the fermionic system. On the next stage scattering processes including momentum

transfer can be described through the dynamics of A and E. The reapplication of Eq. (2.11) with $H_{\text{car-phon}}$ with the assisted densities matrices produces different kinds of expectation values: mixed ones consisting of two fermionic and two bosonic and one with four fermionic creation and annihilation operators. The latter can be split up using the Hartree-Fock factorization:

$$\langle a_A^\dagger a_B^\dagger a_C a_D \rangle \approx \langle a_A^\dagger a_D \rangle \langle a_B^\dagger a_C \rangle - \langle a_A^\dagger a_C \rangle \langle a_B^\dagger a_D \rangle. \quad (2.24)$$

Therefore, the temporal evolution of the electron-phonon scattering contributions A and E, cp. Eqs. (2.22) are given as:

$$\begin{aligned} i\hbar d_t A_{123}^{xyz} &= [\varepsilon_2^y - \varepsilon_1^x + \hbar\omega_3^z] A_{123}^{xyz} \\ &+ \sum_{\lambda} g_{2,1-q,3}^{*\lambda yz} \langle a_{x1}^\dagger a_{\lambda 1} \rangle [n_3^z + 1] \\ &- \sum_{\lambda'} g_{1-q,2,3}^{*\lambda' z} \langle a_{\lambda' 2}^\dagger a_{y2} \rangle n_3^z \\ &- \sum_{\lambda\lambda'} g_{1-q,2,3}^{*\lambda\lambda' z} \langle a_{x1}^\dagger a_{\lambda 1} \rangle \langle a_{\lambda' 2}^\dagger a_{y2} \rangle, \end{aligned} \quad (2.25)$$

$$\begin{aligned} i\hbar d_t E_{123}^{xyz} &= [\varepsilon_2^y - \varepsilon_1^x - \hbar\omega_3^z] E_{123}^{xyz} \\ &- \sum_{\lambda} g_{1,2-q,3}^{\lambda xz} \langle a_{\lambda 2}^\dagger a_{y2} \rangle [n_3^z + 1] \\ &+ \sum_{\lambda'} g_{1,2-q,3}^{y\lambda' z} \langle a_{x1}^\dagger a_{\lambda' 1} \rangle n_3^z \\ &+ \sum_{\lambda\lambda'} g_{1,2-q,3}^{\lambda\lambda' z} \langle a_{\lambda 2}^\dagger a_{y2} \rangle \langle a_{x1}^\dagger a_{\lambda' 1} \rangle. \end{aligned} \quad (2.26)$$

Neglecting memory effects, i.e. applying the Markov Approximation, cp. Chap. 8.1.1, these equations can be integrated directly. Therefrom, δ -functions arise which conserve the momentum dependent energies via absorption or emission of phonons. Inserting the integrated scattering terms into the EOMs on the first stage Boltzmann-like equations for carrier-phonon interaction can be derived. This gives us access to the microscopic carrier dynamics of the electron-phonon induced dephasing and scattering for the polarization and occupations, respectively:

$$\dot{\rho}_{\mathbf{k}}|_{\text{deph}} = \frac{1}{i\hbar} \sum_{q\gamma} \sum_{\lambda\lambda'} \left[+g_{\mathbf{k}-q\mathbf{q}}^{j\lambda'\gamma} A_{\mathbf{k}\mathbf{k}-q\mathbf{q}}^{i\lambda'\gamma} - g_{\mathbf{k}\mathbf{q}}^{\lambda i\gamma} A_{\mathbf{k}+q\mathbf{q}\mathbf{q}}^{\lambda j\gamma} + g_{\mathbf{k}\mathbf{q}}^{*\lambda j\gamma} E_{\mathbf{k}\mathbf{k}+q\mathbf{q}}^{i\lambda\gamma} - g_{\mathbf{k}-q\mathbf{q}}^{*i\lambda'\gamma} E_{\mathbf{k}-q\mathbf{q}\mathbf{q}}^{\lambda' j\gamma} \right], \quad (2.27)$$

$$\dot{\rho}_{\mathbf{k}}^l|_{\text{sc}} = \frac{1}{i\hbar} \sum_{q\gamma} \sum_{\lambda\lambda'} \left[+g_{\mathbf{k}+q\mathbf{q}}^{l\lambda'\gamma} A_{\mathbf{k}\mathbf{k}-q\mathbf{q}}^{i\lambda'\gamma} - g_{\mathbf{k}\mathbf{q}}^{\lambda l\gamma} A_{\mathbf{k}+q\mathbf{q}\mathbf{q}}^{\lambda l\gamma} + g_{\mathbf{k}\mathbf{q}}^{*\lambda l\gamma} E_{\mathbf{k}\mathbf{k}+q\mathbf{q}}^{l\lambda\gamma} - g_{\mathbf{k}-q\mathbf{q}}^{*l\lambda'\gamma} E_{\mathbf{k}-q\mathbf{q}\mathbf{q}}^{\lambda' l\gamma} \right]. \quad (2.28)$$

Analogously the temporal evolution of the phonon distributions can be calculated:

$$\dot{n}_{\mathbf{q}}^\gamma|_{\text{sc}} = \frac{1}{i\hbar} \sum_{\lambda\lambda'\mathbf{k}} \left[+g_{\mathbf{k}-q}^{*\lambda\lambda'\gamma} E_{\mathbf{k}\mathbf{k}-q}^{\lambda'\lambda\gamma} - g_{\mathbf{k}-q}^{\lambda\lambda'\gamma} A_{\mathbf{k}-q\mathbf{q}\mathbf{q}}^{\lambda\lambda'\gamma} \right]. \quad (2.29)$$

2.2.3 Boltzmann Scattering Terms - Fermi's Golden Rule and Pauli Blocking

From the temporal integration of the assisted density matrices within the Markov Approximation the scattering terms for the dephasing of the polarization, as well as the electronic and phonon occupation dynamics have been derived. The dephasing in the polarization splits up into a diagonal and an off-diagonal term driven by $p_{\mathbf{k}}$ and $p_{\mathbf{k}'}$

$$\dot{p}_{\mathbf{k}}|_{deph} = \mathfrak{T}_{\mathbf{k}} p_{\mathbf{k}} + \mathfrak{U}_{\mathbf{k}} p_{\mathbf{k}'}, \quad (2.30)$$

with

$$\mathfrak{T}_{\mathbf{k}} = \frac{\pi}{\hbar} \sum_{\mathbf{q}\gamma\pm} \sum_{\lambda\lambda'}^{C_2V_2} |g_{\mathbf{k}-\mathbf{q}}^{\lambda\lambda\gamma}|^2 \delta(\varepsilon_{\mathbf{k}'}^{\lambda'} - \varepsilon_{\mathbf{k}}^{\lambda} \mp \hbar\omega_{\mathbf{q}}^{\gamma}) V_{\mathbf{k}'\mathbf{q}}^{\lambda'\gamma\pm}, \quad (2.31)$$

$$\mathfrak{U}_{\mathbf{k}} = \frac{\pi}{\hbar} \sum_{\mathbf{q}\gamma\pm} \sum_{\lambda\lambda'}^{V_2C_2} |g_{\mathbf{k}-\mathbf{q}}^{\lambda\lambda'\gamma}|^2 \delta(\varepsilon_{\mathbf{k}'}^{\lambda'} - \varepsilon_{\mathbf{k}}^{\lambda} \mp \hbar\omega_{\mathbf{q}}^{\gamma}) W_{\mathbf{k}\mathbf{q}}^{\lambda\gamma\pm}, \quad (2.32)$$

containing Pauli blocking terms and phonon emission and absorption contributions:

$$V_{\mathbf{k}'\mathbf{q}}^{\lambda'\gamma\pm} := \tilde{n}_{\mathbf{q}\pm}^{\gamma} \rho_{\mathbf{k}'}^{\lambda'} + \tilde{n}_{\mathbf{q}\mp}^{\gamma} (1 - \rho_{\mathbf{k}'}^{\lambda'}), \quad (2.33)$$

$$W_{\mathbf{k}\mathbf{q}}^{\lambda\gamma\pm} := \tilde{n}_{\mathbf{q}\pm}^{\gamma} (1 - \rho_{\mathbf{k}}^{\lambda}) + \tilde{n}_{\mathbf{q}\mp}^{\gamma} \rho_{\mathbf{k}}^{\lambda}, \quad (2.34)$$

with the emission and absorption of a phonon respectively $\tilde{n}_{\mathbf{q}\pm}^{\gamma} = n_{\mathbf{q}}^{\gamma} + \frac{1}{2} \pm \frac{1}{2}$ and $\mathbf{k}' = \mathbf{k} \pm \mathbf{q}$. For the occupations of the electrons in the respective subbands we yield the microscopic Boltzmann equation [37]:

$$\dot{\rho}_{\mathbf{k}}^l|_{sc} = -\frac{2\pi}{\hbar} \sum_{\mathbf{q}\gamma\mp} \sum_{\lambda} |g_{\mathbf{k}'\mathbf{q}}^{l\lambda\gamma}|^2 \delta(\varepsilon_{\mathbf{k}'}^{\lambda'} - \varepsilon_{\mathbf{k}}^l \mp \hbar\omega_{\mathbf{q}}^{\gamma}) F_{\mathbf{k}\mathbf{k}'\mathbf{q}}^{l\lambda\gamma\mp} \quad (2.35)$$

with

$$F_{\mathbf{k}\mathbf{k}'\mathbf{q}}^{l\lambda\gamma\mp} := \tilde{n}_{\mathbf{q}\mp}^{\gamma} \rho_{\mathbf{k}}^l (1 - \rho_{\mathbf{k}'}^{\lambda'}) - \tilde{n}_{\mathbf{q}\pm}^{\gamma} \rho_{\mathbf{k}'}^{\lambda'} (1 - \rho_{\mathbf{k}}^l), \quad (2.36)$$

under the premiss that $l \neq \lambda$. For the numerical calculations within the thesis we will treat the phonons as a bath being approximated by the Bose-Einstein distribution $n_{q_0}^{\Gamma\text{TO}} = \left(1 - e^{-\frac{\hbar\omega_0^{\Gamma\text{TO}}}{k_B T}}\right)^{-1}$

at room temperature ($T = 300\text{K}$) with the constant phonon energy $\hbar\omega_0^{\Gamma\text{TO}} = 192\text{meV}$ around the Γ -point. The equations of motion and their analytical solutions for the phonon dynamics can be found in the Appendix. To identify the scattering terms included in the Boltzmann equation we rewrite Eq. (2.35) explicitly, aiming on the second lowest conduction subband C_2 (for the lowest

subband the equations are symmetric replacing C_2 by C_1):

$$\dot{\rho}_k^{C_2} = \frac{-2\pi}{\hbar} \sum_{q\gamma} \left\{ \underbrace{|g_{k+q}^{C_2\gamma}|^2 \delta(\varepsilon_{k+q}^{C_2} - \varepsilon_k^{C_2} - \hbar\omega_q^\gamma) \left[n_q^\gamma \rho_k^{C_2} (1 - \rho_{k+q}^{C_2}) - (n_q^\gamma + 1) \rho_{k+q}^{C_2} (1 - \rho_k^{C_2}) \right]}_{(1)} \right. \\ \left. + \underbrace{|g_{k-q}^{C_2\gamma}|^2 \delta(\varepsilon_{k-q}^{C_2} - \varepsilon_k^{C_2} + \hbar\omega_q^\gamma) \left[(n_q^\gamma + 1) \rho_k^{C_2} (1 - \rho_{k-q}^{C_2}) - n_q^\gamma \rho_{k-q}^{C_2} (1 - \rho_k^{C_2}) \right]}_{(2)} \right\}, \quad (2.37)$$

$$\dot{\rho}_k^{C_2} = \frac{-2\pi}{\hbar} \sum_{q\gamma} \left\{ \underbrace{|g_{k+q}^{C_2C_1\gamma}|^2 \delta(\varepsilon_{k+q}^{C_1} - \varepsilon_k^{C_2} - \hbar\omega_q^\gamma) \left[n_q^\gamma \rho_k^{C_2} (1 - \rho_{k+q}^{C_1}) - (n_q^\gamma + 1) \rho_{k+q}^{C_1} (1 - \rho_k^{C_2}) \right]}_{(3)} \right. \\ \left. + \underbrace{|g_{k-q}^{C_2C_1\gamma}|^2 \delta(\varepsilon_{k-q}^{C_1} - \varepsilon_k^{C_2} + \hbar\omega_q^\gamma) \left[(n_q^\gamma + 1) \rho_k^{C_2} (1 - \rho_{k-q}^{C_1}) - n_q^\gamma \rho_{k-q}^{C_1} (1 - \rho_k^{C_2}) \right]}_{(4)} \right\}, \quad (2.38)$$

where we split up the equations for the dynamics of the electron occupation $\rho_k^{C_2}$ into intra (ia) - and intersubband (ie) scattering terms. We have therefore four terms describing the scattering between the three energy states $\varepsilon_{\mathbf{k}+\mathbf{q}}$, $\varepsilon_{\mathbf{k}}$ and $\varepsilon_{\mathbf{k}-\mathbf{q}}$: two intra- ((1) and (2)) and two intersubband ((3) and (4)) terms respectively, cp. Fig. 2.2. Every single term contains a scattering process under phonon emission to a lower energetic state and phonon absorption to a higher one, whereby the first is governed with $(n_q^\gamma + 1)$ and the latter with (n_q^γ) . The $(1 - \rho_k^{C_s})$ terms ensure the Pauli Principle, resulting in the condition that the state of in-scattering has to be empty.

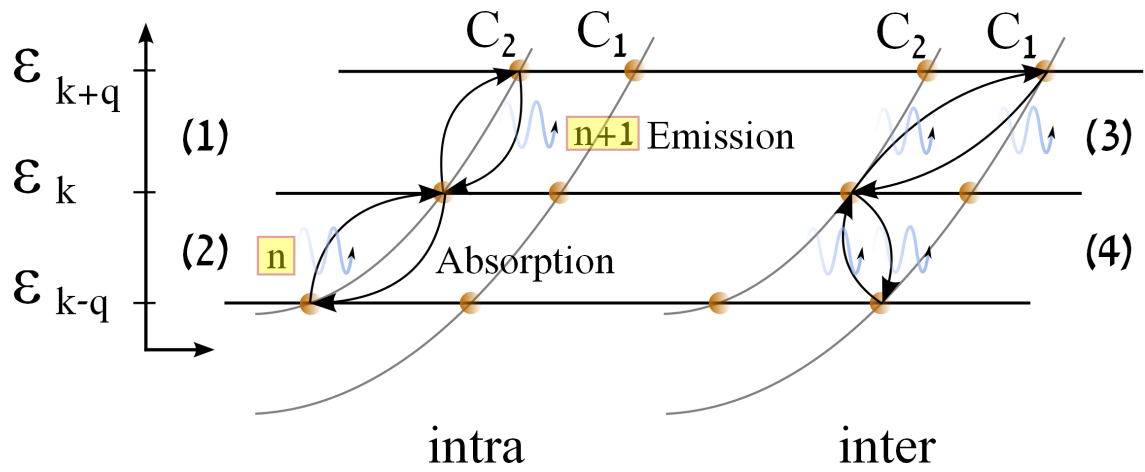


Figure 2.2: Sketch of the energy and momentum conserved electron relaxation processes under phonon emission and absorption expressed by the δ -function in Eq. 2.35. Intra- (left) and intersubband (right) scattering within and between the lowest lying conduction subbands C_1 and C_2 are visualized.

2.3 Analytical Solution of the Dynamics

The equations of motion (2.30,2.35) will be solved analytically to the stage where only the time integration is the numerical task within a Runge-Kutta Algorithm. This leads beside a fast computation time to a deeper insight into the physical mechanisms of the dynamics and the impact of arising scattering prefactors. For the principal derivation we refer the interested reader to the Appendix.

2.3.1 Scattering Prefactors and Jump Amplitudes - The Influence of Subband Curvature -

The derived equations for semiconductors of arbitrary dimension will be now applied to the structure of carbon nanotubes regarding the one dimensional confinement aspect of electrons and phonons. We limit the possibilities of subband couplings to the modeling of photoluminescence excitation and pump-probe experiments, taking into account the two lowest conduction C_1, C_2 and highest lying valence subbands V_1, V_2 . According to the procedure described in the previous section we rewrite the occurring energy conserving δ -functions in the equations (2.30,2.35,8.13) by assuming a parabolic band structure in the vicinity of the K-point $\epsilon_{k\pm q}^l = \alpha_l k^2$. Solving the δ -function for q leads to a quadratic equation exhibiting zero points q_0 . The analytical solutions for the polarization state:

$$\dot{\rho}_k|_{deph} = -\frac{L}{\hbar} \sum_{\gamma\mp} \left(\mathfrak{T}_k(q_0) p_k + \mathfrak{U}_k(q_0) p_{k'} \right), \quad (2.39)$$

with the analytically solved terms for diagonal and off-diagonal dephasing:

$$\mathfrak{T}_k(q_0) = |g_{q_0}^\gamma|^2 \frac{1}{|\mathfrak{Y}_{k\mp}^{\lambda\gamma}|} V_{k\tilde{k}q_0}^{l\gamma\pm} \quad \mathfrak{U}_k(q_0) = |g_{q_0}^\gamma|^2 \frac{1}{|\mathfrak{W}_{k\mp}^{\lambda\gamma}|} W_{k\tilde{k}q_0}^{l\gamma\pm}, \quad (2.40)$$

with $\tilde{k} = k \mp q_0$.

The carrier occupations for conduction band electrons are derived,

$$\dot{\rho}_k^l|_{sc} = -\frac{L}{\hbar} \sum_{\gamma\mp} \left(\mathfrak{I}\mathfrak{A}_k(q_0) + \mathfrak{I}\mathfrak{E}_k(q_0) \right), \quad (2.41)$$

containing intra- and interband scattering:

$$\mathfrak{I}\mathfrak{A}_k(q_0) = |g_{\tilde{k}}^{l\gamma}|^2 \frac{1}{|\mathfrak{X}_{k\mp}^{l\gamma}|} X_{k\tilde{k}q_0}^{l\gamma\pm} \quad \mathfrak{I}\mathfrak{E}_k(q_0) = \sum_{\lambda} |g_{\tilde{k}}^{l\lambda\gamma}|^2 \frac{1}{|\mathfrak{Y}_{k\mp}^{l\lambda\gamma}|} Y_{k\tilde{k}q_0}^{l\lambda\gamma\pm}, \quad (2.42)$$

whereby the latter one has to be summed up over the next lying subband $\lambda \neq l$.

2.3.2 Electron Dynamics

Optical Modes-Constant Jump Amplitudes

Within the same electronic subband, i.e. for intrasubband scattering the evaluation of the energy conservation within the δ -function with constant phonon energies results in the zero points:

$$q_0^{\Gamma\text{TO}} = q_{k\mp}^{l\Gamma\text{TO}} = \pm k \pm \sqrt{k^2 \mp \frac{\varepsilon_{q_0}^{\Gamma\text{TO}}}{\alpha_l}}, \quad (2.43)$$

with the associated scattering prefactors

$$\mathfrak{W}_{k\mp}^{\Gamma\text{TO}} = \mathfrak{X}_{k\mp}^{l\Gamma\text{TO}} = 2\alpha_l \sqrt{k^2 \mp \frac{\varepsilon_{q_0}^{\Gamma\text{TO}}}{\alpha_l}}, \quad (2.44)$$

resembling the quadratic dependence of the electronic dispersion. The scattering efficiency depends on the specific tubes through the corresponding diameter d and the band structure parameters entering in the scattering prefactor $\mathfrak{X}_{k\mp}^{l\Gamma\text{TO}}$.

For intersubband scattering processes with different subband curvatures $\alpha_\lambda \neq \alpha_{\lambda'}$ we derive

$$q_0^{\Gamma\text{TO}} = q_{k\mp}^{l\lambda\Gamma\text{TO}} = \pm k \pm \sqrt{\frac{\alpha_l}{\alpha_\lambda} k^2 \mp \frac{1}{\alpha_\lambda} \left(\varepsilon_{q_0}^{\Gamma\text{TO}} + \left(c_l^\mp \Delta \varepsilon^{l\lambda} \right) \right)}, \quad (2.45)$$

with $c_l^\mp = \mp$ standing for the upper and $c_l^\mp = \pm$ for the lower subband. The energetic gap between the subbands is denoted by $\Delta \varepsilon^{l\lambda} = \varepsilon_k^l - \varepsilon_k^\lambda$. The prefactor follows analogously

$$\mathfrak{W}_{k\mp}^{\lambda\Gamma\text{TO}} = \mathfrak{W}_{k\mp}^{l\lambda\Gamma\text{TO}} = 2\alpha_\lambda \sqrt{\frac{\alpha_l}{\alpha_\lambda} k^2 \mp \frac{1}{\alpha_\lambda} \left(\varepsilon_{q_0}^{\Gamma\text{TO}} + \left(c_l^\mp \Delta \varepsilon^{l\lambda} \right) \right)}. \quad (2.46)$$

Acoustic Modes - Linear Jump Dependence

For acoustic phonons we assume a linear phonon dispersion around the Γ -point [38],cp. Fig. 4.10:

$$\hbar \omega_q^{\Gamma\text{LA}} = \hbar c_s |q| \approx \beta^{\Gamma\text{LA}} |q|, \quad (2.47)$$

with the velocity of acoustic phonons $c_s = 2 \times 10^4 \frac{m}{s}$ and the reduced Planck constant $\hbar = 0.658 \text{ eV fs}$ the slope is $\beta^{\Gamma\text{LA}} = 0.013 \text{ eV nm}$. This leads to the condition that a scattering event with acoustic phonons is only possible when the linear phonon dispersion cuts the parabolic approximated electronic band structure. From this we derive the zero points

$$q_0^{\Gamma\text{LA}} = q_{k\mp}^{l\Gamma\text{LA}} = \pm 2k \mp \frac{\beta^{\Gamma\text{LA}}}{\alpha_l}, \quad (2.48)$$

with the according linear scattering prefactors

$$\boxed{\mathfrak{X}_{k\mp}^{\Gamma LA} = \pm 2\alpha_l k \mp \beta^{\Gamma LA}}. \quad (2.49)$$

They explicitly display that the scattering efficiency for acoustic phonons depends on the relation between the slope $\beta^{\Gamma LA}$ of the phononic and the curvature α_l of the electronic dispersion. In contrast to optical phonons the absolute value dependence for the acoustic mode leads to four different phonon occupation functions:

$$n_{q_0}^{\Gamma LA-up} = \left[\exp \left(\frac{\beta^{\Gamma LA}}{k_B T} \left| -2k \pm \frac{\beta^{\Gamma LA}}{\alpha_l} \right| \right) \right]^{-1}, \quad (2.50)$$

$$n_{q_0}^{\Gamma LA-down} = \left[\exp \left(\frac{\beta^{\Gamma LA}}{k_B T} \left| 2k \mp \frac{\beta^{\Gamma LA}}{\alpha_l} \right| \right) \right]^{-1}, \quad (2.51)$$

which take into account the up and down scattering process and also that the slope β can have positive and negative sign.

2.4 At a Glance

On the basis of the density matrix theory we derived coupled equations of motion for the microscopic polarization p_k and occupations ρ_k^l for carriers within the conduction and valence subbands to describe the non-radiative relaxation dynamics in carbon nanotubes. Due to the confinement to one-dimension we were able to further solve the equations of motion analytically beyond the occurring delta-functions in the Boltzmann scattering terms. From this, we yield scattering prefactors which will be of importance for the upcoming interpretation of the relaxation dynamics.

2.4. *AT A GLANCE*

3

Launching the Carbon Nanotube

The solids at the heart of this thesis are single-walled carbon nanotubes or briefly CNTs. They have polarized the attention of the physics and material science community since Iijima synthesized and observed them 23 years ago in 1991 [3]. CNTs are tiny hollow cylinders obtained by cutting graphene in specific direction for a certain length and rolling it up. Exposing a high aspect ratio with diameters of few nanometers and lengths of micro- to centimeters, CNTs bridge the microscopic quantum world with the macroscopic one. The rolling up process of CNTs imposes additional periodic boundary conditions to the wave functions implied in the systems, selecting only some of the electronic states that are present in graphene. Thus, even if graphene is a semi-metal, CNTs can be either metallic or even semiconducting, depending upon their chiral vector \mathbf{c} . Semiconducting CNTs exhibit emission of photons due to the band-to-band radiative recombination of the electron-hole pair. This makes them highly relevant for fundamental and applied research in optoelectronics.

3.1 Microscopic Properties of Carbon Nanotubes: Electronic, Phononic and Optical Features

The investigation of the electron and phonon dynamics, i.e. their interaction via scattering leading to relaxation dynamics gives insight into non-radiative ultrafast processes. These are the essential processes which occur between optical excitation and radiative recombination in semiconducting nanostructures. We will investigate such processes from non-equilibrium into equilibrium driven by electron-phonon interaction enabling intra- and intersubband relaxation. Therefore, the knowledge of the electronic band structure, the phononic dispersion relations and the coupling elements between the involved quasi-particles in carbon nanotubes is needed. These properties differ from other nanostructures since every single tube has its own one-dimensional features which will be emphasized in our calculations through their specific band edge energies $\epsilon_{k_0}^l$ and curvatures of the subbands α_l .

3.1.1 Electronic System

Graphene is Rolled Up - Structure Through Symmetry

To understand the properties of CNTs we have to start with graphene, the material that is wrapped up into a cylinder forming the tube. Of course this is not the way nanotubes are fabricated but the concept leads to workable results. As a consequence of the process of rolling up the two dimensional graphene layer, the created carbon nanotube is one-dimensional. The term "one-dimensional" is related to the degrees of freedom for quasi-particles within the solid. Since the

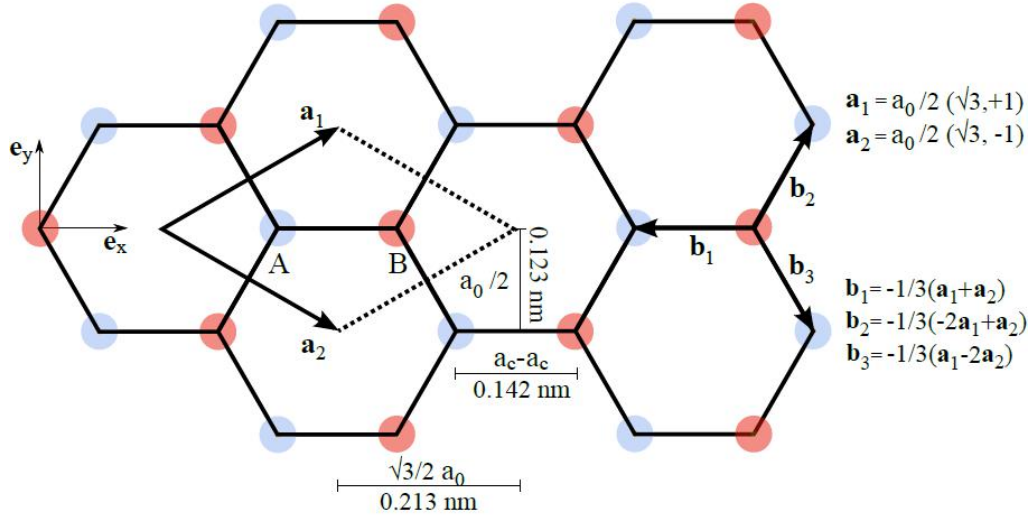


Figure 3.1: Vector relations of graphene in the direct lattice. The lattice vectors \mathbf{a}_1 and \mathbf{a}_2 span the unit cell containing two carbon atoms labeled A and B.

tube is about a few nanometers in its diameter and up to several micrometers in length, the motion of carriers is confined to one dimension.

In graphene the unit cell is spanned by two lattice vectors

$$\mathbf{a}_1 = \frac{a_0}{2} \left(\sqrt{3}, +1 \right) \quad \mathbf{a}_2 = \frac{a_0}{2} \left(\sqrt{3}, -1 \right), \quad (3.1)$$

with the lattice constant $a_0 = \sqrt{3}a_{c-c} = |\mathbf{a}_1| = |\mathbf{a}_2| = 0.246 \text{ nm}$, where $a_{c-c} = 0.142 \text{ nm}$ is the nearest neighbor distance between two carbon atoms in graphite [39], cp. Fig. 3.1. A CNT can be described by either its diameter d and chiral angle ϑ or its chiral indices n_1, n_2 . These two properties will play a key role in the individual behavior of relaxation processes for every single tube, determining the electronic properties as also appearing in the electron-phonon coupling. We will derive in the next sections the dependency of collective patterns on the diameter and the chiral angle. Both structural properties d and ϑ are contained in the chiral vector along which the graphene sheet is rolled up into the tube, cp. Fig. 3.2. It is composed as a linear combination of the graphene basis vectors \mathbf{a}_1 and \mathbf{a}_2

$$\mathbf{c} = n_1 \mathbf{a}_1 + n_2 \mathbf{a}_2, \quad (3.2)$$

via the scalar valued chiral indices (n_1, n_2) . These two indices represent the full information of a nanotube both geometric and electronic. The absolute value of \mathbf{c} represents the circumference of a CNT. Since the diameter of a cylinder is proportional to its circumference $d = \frac{c}{\pi}$ and the absolute value of the chiral vector is

$$c = |\mathbf{c}| = |n_1 \mathbf{a}_1 + n_2 \mathbf{a}_2| = a_0 \sqrt{N_{12}}, \quad (3.3)$$

the diameter can be written with the chiral indices

$$d = \frac{a_0}{\pi} \sqrt{N_{12}}, \quad (3.4)$$

with $N_{12} := n_1^2 + n_1 n_2 + n_2^2$. The angle $\vartheta = \angle(\mathbf{c}, \mathbf{a}_1)$ enclosing the chiral with the direction of the graphene lattice vector is called chiral angle. This angle defines in which direction the graphene sheet is rolled up. From the scalar product of these two vectors

$$\mathbf{c} \cdot \mathbf{a}_1 = |\mathbf{c}| |\mathbf{a}_1| \cos \vartheta, \quad (3.5)$$

we can express the chiral angle

$$\vartheta = \arccos \left[\frac{n_1 + \frac{1}{2}n_2}{\sqrt{N_{12}}} \right], \quad (3.6)$$

like for the diameter via the chiral indices n_1, n_2 .

Perpendicular to the chiral vector \mathbf{c} , the smallest corresponding graphene lattice vector \mathbf{a} defines

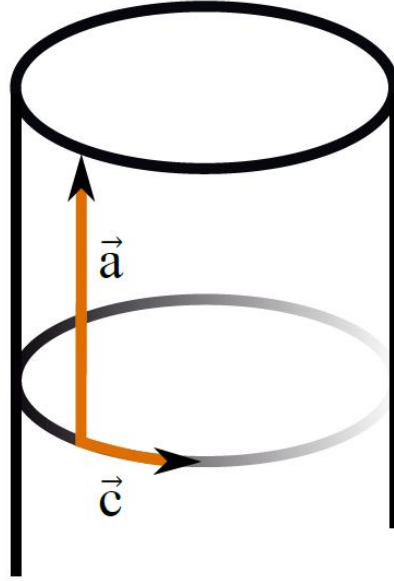


Figure 3.2: The geometrical relations between the translational period \mathbf{a} and the circumference vector \mathbf{c} .

via its absolute value the repeated translational period along the tube axis, cp. Fig. 3.2. This vector can be also determined by the chiral indices n_1, n_2

$$\mathbf{a} = -\frac{1}{\gcd \mathfrak{R}} \left([2n_2 + n_1] \mathbf{a}_1 - [2n_1 + n_2] \mathbf{a}_2 \right), \quad (3.7)$$

with the integer

$$\mathfrak{R} = \begin{cases} 3, & \text{if } \frac{(n_1 - n_2)}{3 \gcd} \in \mathbb{Z} \\ 1, & \text{if } \frac{(n_1 - n_2)}{3 \gcd} \notin \mathbb{Z}, \end{cases} \quad (3.8)$$

where \gcd abbreviates the greatest common divisor between the chiral indices n_1, n_2 . Thus the translational period is given through

$$a = |\mathbf{a}| = \frac{a_0 \sqrt{3N_{12}}}{\gcd \mathfrak{R}}. \quad (3.9)$$

The number of graphene hexagons in the nanotube unit cell N_{hexa} can be derived from the ratio between the area of the nanotube and the graphene unit cell

$$\frac{|\mathbf{a} \times \mathbf{c}|}{|\mathbf{a}_1 \times \mathbf{a}_2|} = \frac{|\mathbf{a}| \cdot |\mathbf{c}| \sin \frac{\pi}{2}}{|\mathbf{a}_1 \times \mathbf{a}_2|} = \frac{\sqrt{3}a_0 N_{12}}{\gcd \mathfrak{R}} \frac{2}{\sqrt{3}a_0} = \frac{2N_{12}}{\gcd \mathfrak{R}} = N_{hexa}. \quad (3.10)$$

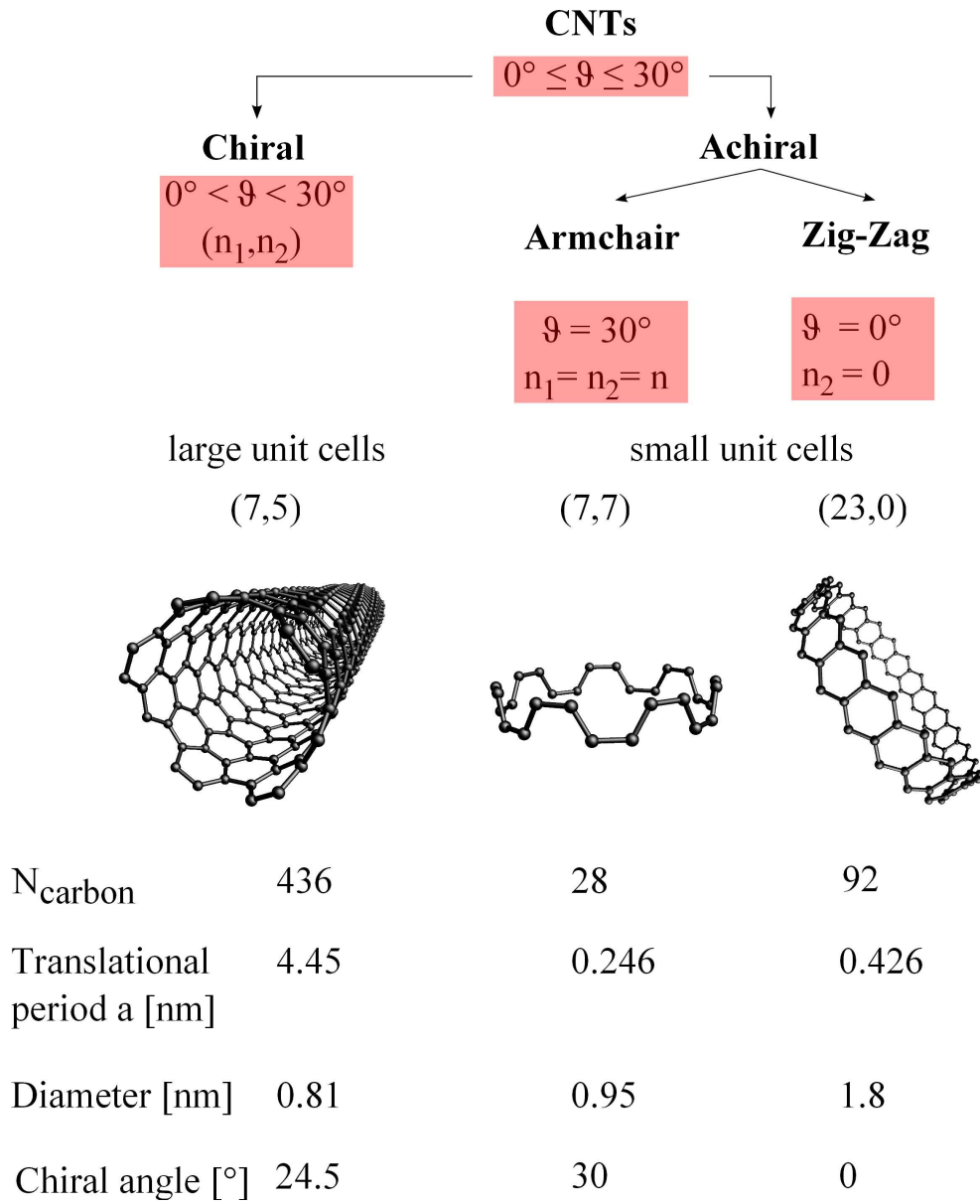


Figure 3.3: Classification of carbon nanotubes via their chiral angles ϑ into chiral and achiral tubes, whereby the latter cover the special case of $\vartheta = 0^\circ$ and $\vartheta = 30^\circ$ called zig-zag and armchair tubes according to the form of their unit cell edges.

Because the graphene unit cell contains only two carbon atoms localized at the positions $\frac{1}{3}(\mathbf{a}_1 + \mathbf{a}_2)$ and $\frac{2}{3}(\mathbf{a}_1 + \mathbf{a}_2)$ the number of carbon atoms in it follows directly

$$N_{\text{carbon}} = 2N_{\text{hexa}} = \frac{4N_{12}}{\text{gcd } \mathfrak{R}}. \quad (3.11)$$

3.1. MICROSCOPIC PROPERTIES OF CARBON NANOTUBES: ELECTRONIC, PHONONIC AND OPTICAL FEATURES

The value of the chiral angle ϑ ranges from 0° to 30° . Therefore, CNTs are classified into three structured types through their chiral angle. The tubes with an angle between $0^\circ < \vartheta < 30^\circ$ are called chiral tubes. On the other hand we have two types of high symmetry for tubes that have a ϑ at the upper or lower limit of the range of the chiral tubes. Zig-Zag tubes with $n_2 = 0$ and $\vartheta = 0^\circ$ and armchair tubes with $n_1 = n_2$ and $\vartheta = 30^\circ$. The names originate from the edge of the unit cells that resembles armchair or zig-zag chains. These two types build the group of the so called achiral tubes in contrast of the chiral ones. The achiral CNTs have small unit cells and therefore contain $4n$ carbon atoms, while the chiral tubes can be more extended and contain hundreds of atoms. For example the achiral (23,0) tube contains 84 and in opposite the chiral (7,5) tube 436 carbon atoms within its unit cell.

3.1.2 Entering the Reciprocal Space - On the Way to One Dimension

To realize the one dimensionality for CNTs one has to think in the reciprocal space which is a mathematical construction described first by Josiah Willard Gibbs 1881 in his book 'Vector Analysis' as the reciprocal system which was further developed in crystallography to the reciprocal lattice. In solid state theory this conception has been extended to the reciprocal space to describe the quantum mechanical behavior of the so called quasi-particles, e.g. electrons and phonons within the solid. It will also be the key for understanding the energy and momentum conservation

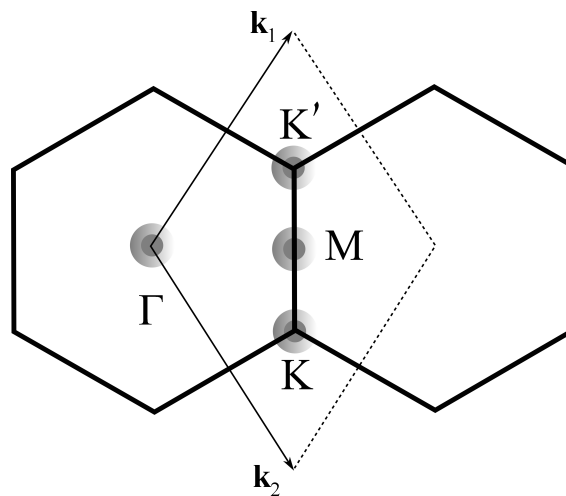


Figure 3.4: Reciprocal lattice of graphene displaying the Brillouin Zone and with the high symmetry points Γ , M , K and K' spanned by \mathbf{k}_1 and \mathbf{k}_2 .

underlying the scattering processes. Straight forward we obtain the reciprocal lattice vectors from the direct lattice vectors, cp. Eq. (3.1):

$$\mathbf{k}_1 = \frac{2\pi}{a_0} \left(\frac{1}{\sqrt{3}}, +1 \right) \quad \mathbf{k}_2 = \frac{2\pi}{a_0} \left(\frac{1}{\sqrt{3}}, -1 \right). \quad (3.12)$$

Keeping on with the notation and composition of the book of Reich *et al.* [7] we review the quantized wave vector \mathbf{k}_\perp being perpendicular and the continuous reciprocal lattice vector \mathbf{k}_z being parallel to the tube axis:

$$\mathbf{k}_\perp = \frac{1}{\text{gcd } N_{\text{hexa}} \mathfrak{R}} \left([2n_1 + n_2] \mathbf{k}_1 + [n_1 + 2n_2] \mathbf{k}_2 \right) \quad \mathbf{k}_z = \frac{1}{N_{\text{hexa}}} \left(-n_2 \mathbf{k}_1 + n_1 \mathbf{k}_2 \right). \quad (3.13)$$

The absolute value of both vectors is given through

$$|\mathbf{k}_\perp| = \frac{2\pi}{|\mathbf{c}|} m \quad |\mathbf{k}_z| = \frac{2\pi}{|\mathbf{a}|}, \quad (3.14)$$

with m labeling the subbands arising from the quantization of \mathbf{k}_\perp within the zone-folding approach which will be described in the following section.

3.1.3 From Graphene to Carbon Nanotubes - Reducing the Dimension through Zone-Folding

Since a CNT is based on graphene, which is rolled up into a cylinder, its electronic band structure is derived from that of graphene. The process of rolling up introduces periodic boundary conditions that are described through the zone-folding approximation [7, 2]. We will discuss this concept more detailed at the end of this section. The derivation of the energy dispersion relation of graphene in tight-binding and nearest neighbor approximation is presented in a very clear way in the previous quoted Ref. [7] and we will summarize here. The access to the band structure of a solid like graphene can be attributed to the solution of the time independent Schrödinger Equation

$$H \psi_{\mathbf{k}}(\mathbf{r}) = \varepsilon_{\mathbf{k}} \psi_{\mathbf{k}}(\mathbf{r}), \quad (3.15)$$

for an electron in a periodic potential. In our case this is the periodic lattice potential of the ionic cores of carbon. The solution is an eigenvalue problem of the perturbed Hamiltonian with the \mathbf{k} wave vector dependent eigenvalues $E_{\mathbf{k}}$ and the eigenfunctions $\psi_{\mathbf{k}}(\mathbf{r})$ which are a linear combination of the electronic wave functions

$$\psi_{\mathbf{k}}(\mathbf{r}) = \sum_j^{A,B} C_{\mathbf{k}}^j \Phi_{\mathbf{k}}^j(\mathbf{r}), \quad (3.16)$$

with j running over the two sublattices A and B contained in the unit cell. Within the tight-binding approximation [40, 41] the superposition of wave functions for isolated carbon atoms can be

3.1. MICROSCOPIC PROPERTIES OF CARBON NANOTUBES: ELECTRONIC, PHONONIC AND OPTICAL FEATURES

expressed by the linear combination of the atomic wave functions φ :

$$\Phi_{\mathbf{k}}^j(\mathbf{r}) = \frac{1}{\sqrt{N}} \sum_{\mathbf{R}_j}^N e^{i\mathbf{k}\cdot\mathbf{R}_j} \cdot \varphi(\mathbf{r} - \mathbf{R}_j), \quad (3.17)$$

where N is the number of unit cells in the crystal and \mathbf{R}_j are the lattice vectors in real space. This implies that we assume the electrons to be tightly bound to their atomic nuclei. Starting from isolated atoms with defined eigenfunctions and ϵ -values their wave functions overlap by decreasing the distance between them, which shapes the chemical bonds and forms the crystal. As a result of this process, the electronic energies broaden and build up continuous bands. We simplify the last equation to the unit cell of graphene. If we substitute the eigenfunctions $\psi_{\mathbf{k}}(\mathbf{r})$ in the Schrödinger Equation by the combination of the electronic wave functions and multiplying both sides with two equivalent Bloch functions $\Phi_{\mathbf{k}}^A$ and $\Phi_{\mathbf{k}}^B$ for the two sublattices, we obtain a system of two linear equations:

$$C^A [H_{\mathbf{k}}^{AA} - \epsilon_{\mathbf{k}} S_{\mathbf{k}}^{AA}] + C^B [H_{\mathbf{k}}^{AB} - \epsilon_{\mathbf{k}} S_{\mathbf{k}}^{AB}] = 0, \quad (3.18)$$

$$C^A [H_{\mathbf{k}}^{BA} - \epsilon_{\mathbf{k}} S_{\mathbf{k}}^{BA}] + C^B [H_{\mathbf{k}}^{BB} - \epsilon_{\mathbf{k}} S_{\mathbf{k}}^{BB}] = 0, \quad (3.19)$$

with the interacting matrix elements $H_{ij} = \langle \varphi_i | H | \varphi_j \rangle$ of the Hamiltonian and the overlap between the Bloch functions $S_{ij} = \langle \varphi_i | \varphi_j \rangle$. This linear equation system has a non trivial solution only if the secular determinant vanishes $|H - \epsilon_{\mathbf{k}}^j S| = 0$. By the fact that the atoms in the graphene unit cell are equivalent, we yield a symmetric situation and the matrix elements simplify to $H^{AA} = H^{BB}$, $H^{AB} = (H^{BA})^*$ and $S^{AA} = S^{BB}$, $S^{AB} = (S^{BA})^*$. Therefore, the secular equation can be written as

$$\begin{vmatrix} H_{\mathbf{k}}^{AA} - \epsilon_{\mathbf{k}} S_{\mathbf{k}}^{AA} & H_{\mathbf{k}}^{AB} - \epsilon_{\mathbf{k}} S_{\mathbf{k}}^{AB} \\ (H_{\mathbf{k}}^{AB})^* - \epsilon_{\mathbf{k}} (S_{\mathbf{k}}^{AB})^* & H_{\mathbf{k}}^{AA} - \epsilon_{\mathbf{k}} S_{\mathbf{k}}^{AA} \end{vmatrix} = 0. \quad (3.20)$$

Evaluating this 2×2 determinant and using the quadratic formula yields the eigenvalues for the conduction and the valence band

$$\epsilon_{\mathbf{k}}^{C,V} = \Omega \mp \sqrt{\Omega^2 - |H^{AA}|^2 + |H^{AB}|^2}, \quad (3.21)$$

with

$$\Omega = \frac{H^{AA} S^{AA} - \Re\{H^{AB} (S^{AB})^*\}}{|S^{AA}|^2 - |S^{AB}|^2}. \quad (3.22)$$

Neglecting the overlap between the wave functions, i.e. setting $S^{AA} = 1$ and $S^{AB} = 0$ we yield the formula for the band structure of graphene

$$\epsilon_{\mathbf{k}}^{C,V} = H^{AA} \pm |H^{AB}|, \quad (3.23)$$

which was first derived 1947 by Wallace [42]. Applying the nearest-neighbor approximation, which will describe in the following in more detail we can assume that $H_{\mathbf{k}}^{AA} = const. = H^{AA}$ since only

the self interaction of atom A has to be taken into account. The crossing of the π and π^* bands at the K-point at the Fermi energy E_F leads to

$$H^{AA} - |H_{\mathbf{k}}^{AB}| = H^{AA} + |H_{\mathbf{k}}^{AB}| = E_F = 0, \quad (3.24)$$

yielding the band structure of graphene in tight-binding and nearest-neighbor approximation:

$$\epsilon_{\mathbf{k}}^{C,V} = \mp |H_{\mathbf{k}}^{AB}|. \quad (3.25)$$

Nearest-Neighbor Approximation

The unit cell of graphene contains two atoms labeled A and B, respectively, cp. Fig. 3.1. Using the symmetry that the two atoms are equal we now expand the theory by taking the interaction of the first nearest-neighbors into account. For atom A the matrix element which is given via its self-interaction and summation over all other atoms A' in the crystal [7]:

$$H^{AA} = \langle \psi_A | H | \psi_{A'} \rangle = \frac{1}{N} \sum_{\mathbf{R}_A} \sum_{\mathbf{R}_{A'}} \langle e^{i\mathbf{k} \cdot \mathbf{R}_A} \varphi(\mathbf{r} - \mathbf{R}_A) | H | e^{i\mathbf{k} \cdot \mathbf{R}_{A'}} \varphi(\mathbf{r} - \mathbf{R}_{A'}) \rangle, \quad (3.26)$$

resembled by the summation over all A atoms. We consider the interaction with the three B atoms shown in Fig. 3.1 which belong to sublattice B. Therefore, the second sum contains only the term with $\mathbf{R}_{A'} = \mathbf{R}_A$ which simplifies the equation to

$$H^{AA} = \frac{1}{N} \sum_{\mathbf{R}_A} e^{i\mathbf{k} \cdot (\mathbf{R}_A - \mathbf{R}_A)} \langle \varphi_A(\mathbf{r} - \mathbf{R}_A) | H | \varphi_A(\mathbf{r} - \mathbf{R}_A) \rangle =: \epsilon_{2p}. \quad (3.27)$$

This shows that H^{AA} is constant within the interaction of the first nearest neighbors. By knowing the Hamiltonian and the atomic orbitals φ_A it is possible to calculate ϵ_{2p} . The matrix element between the atoms A and B can be approximated by

$$H^{AB} = \langle \varphi_A | H | \varphi_B \rangle \approx \frac{1}{N} \sum_{\mathbf{R}_A} \sum_{\mathbf{R}_i=1,2,3} e^{i\mathbf{k} \cdot (\mathbf{R}_A - \mathbf{R}_i)} \langle \varphi_A(\mathbf{r} - \mathbf{R}_A) | H | \varphi_A(\mathbf{r} - \mathbf{R}_i) \rangle, \quad (3.28)$$

whereby the second sum runs over all three nearest neighbors of atom A. Considering the vectors \mathbf{b}_i connecting the atom located at \mathbf{r}_0 with its three nearest neighbors at \mathbf{r}_i , cp. Fig. 3.1 being a linear combination of the graphene lattice vectors \mathbf{a}_1 and \mathbf{a}_2 yields:

$$H^{AB} = \gamma_0 \sum_{j=1}^3 e^{i\mathbf{k} \cdot \mathbf{b}_j}, \quad (3.29)$$

with the carbon-carbon interaction energy $\gamma_0 =: \langle \varphi_A(\mathbf{r} - \mathbf{R}_A) | H | \varphi_A(\mathbf{r} - \mathbf{R}_B) \rangle$ being constant because the distances for all first three nearest-neighbors are equal. We further define the nearest

3.1. MICROSCOPIC PROPERTIES OF CARBON NANOTUBES: ELECTRONIC, PHONONIC AND OPTICAL FEATURES

neighbor sum

$$f_{\mathbf{k}} := \sum_{j=1}^3 e^{i\mathbf{k} \cdot \mathbf{b}_j}, \quad (3.30)$$

which sums up the scalar products between the connecting vectors of the first 3 nearest-neighbor atoms and the reciprocal wave vector \mathbf{k} . This leads us to the energy dispersion relation of graphene

$$\epsilon_{\mathbf{k}}^l = \frac{\epsilon_0 \pm \gamma_0 |f_{\mathbf{k}}|}{1 \pm s_0 |f_{\mathbf{k}}|}, \quad (3.31)$$

with $l = V, C$ denoting the valence and conduction bands, respectively. The values of the tight-binding parameters can be obtained from experimental data [7]. The overlap parameter is accordingly $s_0 = 0.07$ and the interaction energy $\gamma = -2.7 \text{ eV}$. For the relaxation processes within photoluminescence and pump-probe experiments we rely on the optically important K-point, cp. Fig. 3.6. The valence and conduction bands are assumed to be mirror symmetric with respect to the Fermi energy E_F , i.e. $E^V = -E^C$. This implies that we may neglect the self interaction, i.e. we set $\epsilon_0 = 0 \text{ eV}$ and the overlapping is $s_0 \approx 0$. Therefore, we can write the band structure of graphene as

$$\epsilon_{\mathbf{k}}^l = \pm \gamma_0 |f_{\mathbf{k}}|. \quad (3.32)$$

With the previous made assumptions we yield a symmetric valence- and conduction band characteristic that crosses at the K-point and delivers a twofold bigger gap at the Γ -point than at the M-point. This is the reason why graphene is called a semi-metal which will play an important role for its band structure and thus the electronic properties of carbon nanotubes.

Zone Folding - Cutting Lines in Graphene

The process of rolling up the graphene sheet to form the CNT boundary conditions onto the electronic band structure of graphene arise. While the wave vector along the axis of the tube \mathbf{k}_z is quasi-continuous, the wave vector \mathbf{k}_\perp perpendicular to it has to be quantized. The electronic wave functions $\psi_{\mathbf{k}}$, which are the eigenfunctions of the stationary Schrödinger equation (3.15) can be written for an electron in a crystal as a Bloch wave function via the Bloch Theorem

$$\psi_{\mathbf{k}}(\mathbf{r}) = \psi_{\mathbf{k}}(\mathbf{r})e^{i\mathbf{k} \cdot \mathbf{c}} = \psi_{\mathbf{k}}(\mathbf{r} + \mathbf{c}), \quad (3.33)$$

with the condition, that after a complete translation the wave functions have to match, i.e. according to the unrolled graphene they have to be equal at the edges of the sheet. This leads to the condition that the scalar product between the electronic wave and chiral vector has to be periodic within the multiple of 2π . Since \mathbf{k}_\perp and \mathbf{c} are parallel we have the relation

$$\mathbf{k} \cdot \mathbf{c} = m \cdot 2\pi = |\mathbf{k}_\perp| |\mathbf{c}| \cos \angle(k_\perp, c). \quad (3.34)$$

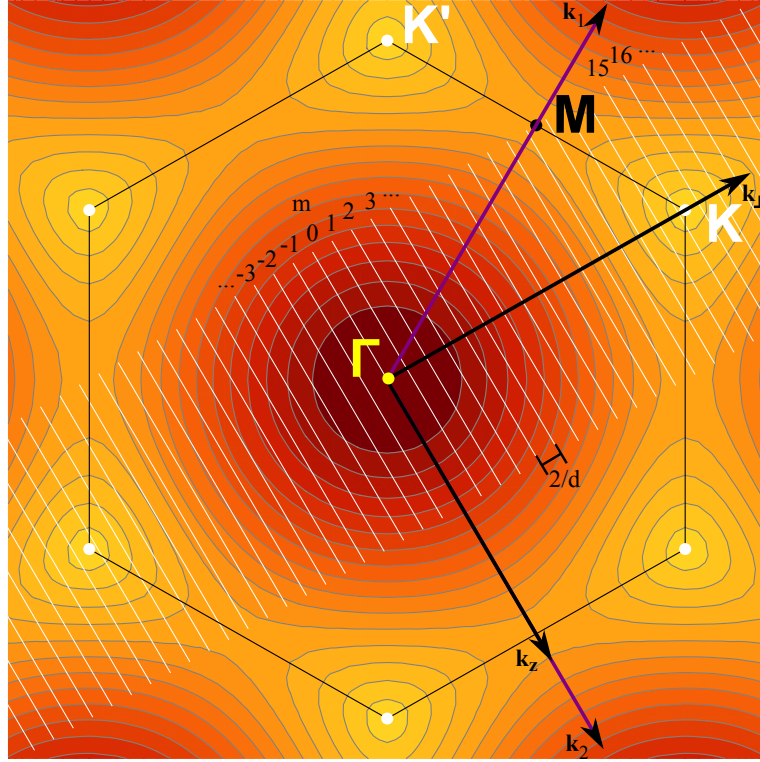


Figure 3.5: Cutting lines plotted onto the electronic band structure of the graphene Brillouin Zone constituting the semiconducting (2,3) zig-zag tube. The subbands introduced by zone folding are labeled with m and reach from $(-\frac{N_{hexa}}{2}, +\frac{N_{hexa}}{2}]$.

Resolving this equation yields the absolute value of the quantized perpendicular wave vector

$$k_{\perp} = m \frac{2}{d}, \quad (3.35)$$

which scales inverse with the diameter of the tube. By this, the Brillouin-zone of graphene is divided into m equally separated allowed lines corresponding to the subbands of the CNT. The integer m represents a new quantum number describing the angular momentum of the electron. Its conservation will be the basis of the selection rules for optical transitions in CNTs. The cutting lines run from $(-\frac{N_{hexa}}{2}, +\frac{N_{hexa}}{2}]$ with an interval of $2/d$ being parallel to the tube axis. Nevertheless, the zone folding method is an approach which neglects existing curvature effects of the cylindrical tube. For tubes with diameters larger than 0.8 nm it has been shown to be a suitable approximation [43, 44]. From Eq. (3.35) it is clear, that by raising the diameter, the distance between these lines vanish and the band structure of graphene is again achieved.

Electronic Band Structure of Carbon Nanotubes

The wave vector of graphene \mathbf{k} is divided in the continuous k_z component along the axis of the tube and \mathbf{k}_\perp perpendicular to it which is quantized according to the zone folding approach introduced above

$$\mathbf{k} = \frac{m}{2N_{12}} \left([2n_1 + n_2]\mathbf{k}_1 + [n_1 + 2n_2]\mathbf{k}_2 \right) - \frac{1}{N_{hexa}} \left([n_2]\mathbf{k}_1 - [n_1]\mathbf{k}_2 \right). \quad (3.36)$$

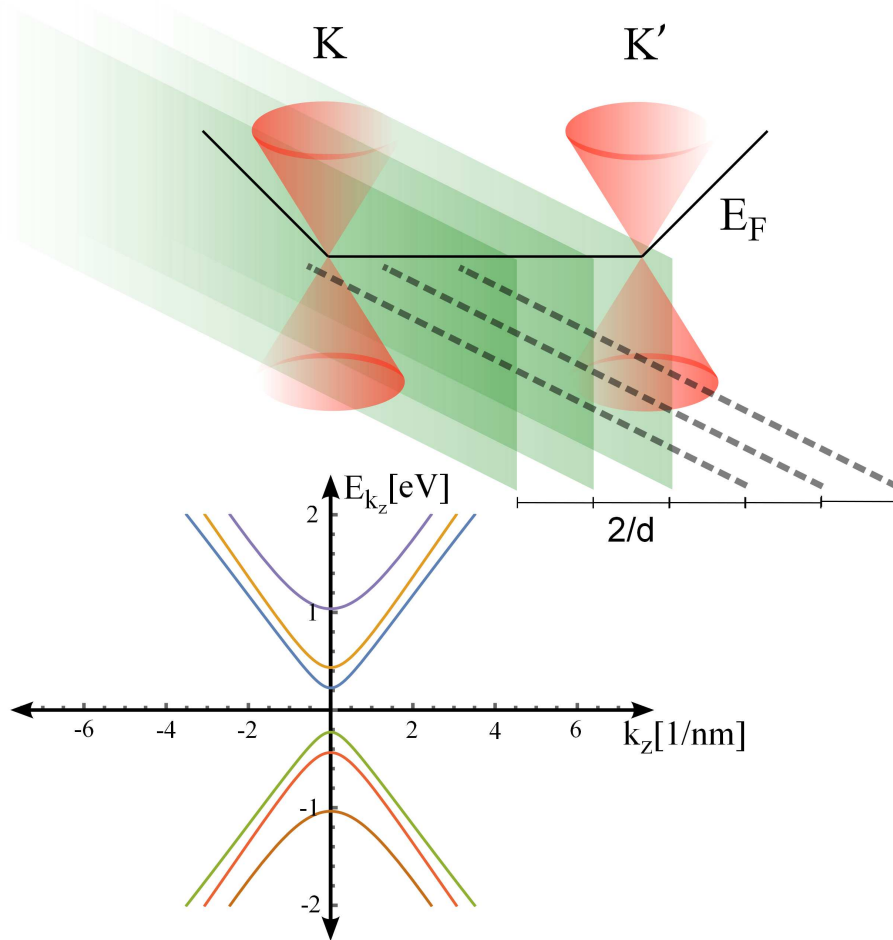


Figure 3.6: Sketch of the concept of cutting lines for a semiconducting carbon nanotube. The cutting lines create conic sections of the Dirac cones at the K-points within the graphene Brillouin-Zone leading to the one-dimensional band structure of CNTs.

Inserting this quantized wave vector into the equation for the band structure of graphene, cp. Eq. (3.32) with

$$\begin{aligned} |f(k)| &= \sqrt{3 + 2\cos(\mathbf{k}(\mathbf{a}_1 - \mathbf{a}_2)) + 2\cos(\mathbf{k}\mathbf{a}_2) + 2\cos(\mathbf{k}\mathbf{a}_1)} \\ &= \sqrt{3 + 2\cos(2\pi(k_1 - k_2)) + 2\cos(2\pi k_2) + 2\cos(2\pi k_1)} \end{aligned} \quad (3.37)$$

leads to the band structure of carbon nanotubes [45]:

$$E_{k_z}^{V_s, C_s}(m) = \pm \gamma_0 \sqrt{3 + 2\cos[A] + 2\cos[B] + 2\cos[C]} \quad (3.38)$$

where we used the abbreviations:

$$A = \pi m \left[\frac{2n_1 + n_2}{N_{12}} \right] - 2\pi \left[\frac{n_2}{N_{hexa}} \right] k_z, \quad (3.39)$$

$$B = \pi m \left[\frac{n_1 + 2n_2}{N_{12}} \right] + 2\pi \left[\frac{n_1}{N_{hexa}} \right] k_z, \quad (3.40)$$

$$C = A - B. \quad (3.41)$$

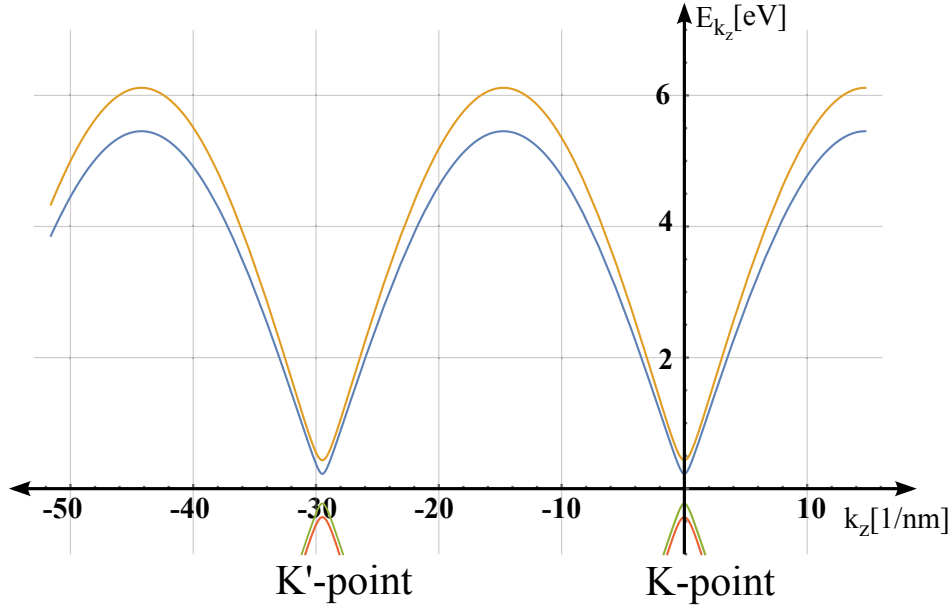


Figure 3.7: Calculated band structure for the semiconducting (23,0) tube. Around the optically relevant K-point the lowest lying subbands are plotted.

3.1.4 Density of states (DOS) in One Dimension

The density of states in a certain energy interval describes the number of states of levels which are available for being occupied. In momentum space the DOS depends on the dimensionality of the system:

$$D(\varepsilon) = \frac{1}{L^d} \sum_{k,l,s} \delta(\varepsilon - \varepsilon_k^l), \quad (3.42)$$

with d denoting the dimensions of the considered system, $l = V, C$ the energy band and s the spin quantum number[2]. In the case of one-dimensional structures like CNTs (wires) the confinement leads to a divergence at the band edges of the subbands of the electronic band structure. Those singular points are known as van Hove singularities. In their surrounding, the DOS scales as $\varepsilon^{-\frac{1}{2}}$. Through the approximation of the electronic band structure around the K-point with parabolas $\varepsilon_k^l = \alpha_l k^2 + \varepsilon_0^l$ the DOS can be written as [2]:

$$D(\varepsilon) = \frac{8}{2\pi} \sum_l \int dk' \frac{1}{|2\alpha_l(k' - k_0^l)|} \delta(k' - k') = \sum_l \frac{2}{\pi\sqrt{\alpha_l}} \frac{1}{\sqrt{\varepsilon^l - \varepsilon_0^l}}. \quad (3.43)$$

Only for values larger than the band edge energy $\varepsilon^l > \varepsilon_0^l$ the DOS has a positive value, while towards the band edge the above mentioned divergences occur, *i.e.* the van Hove singularities. In Fig. The transitions labeled as E_{22} and E_{11} in Fig. 6.5 will be in the focus for our relaxation dynamic studies, as they rule the optical emission process we will consider in this thesis.

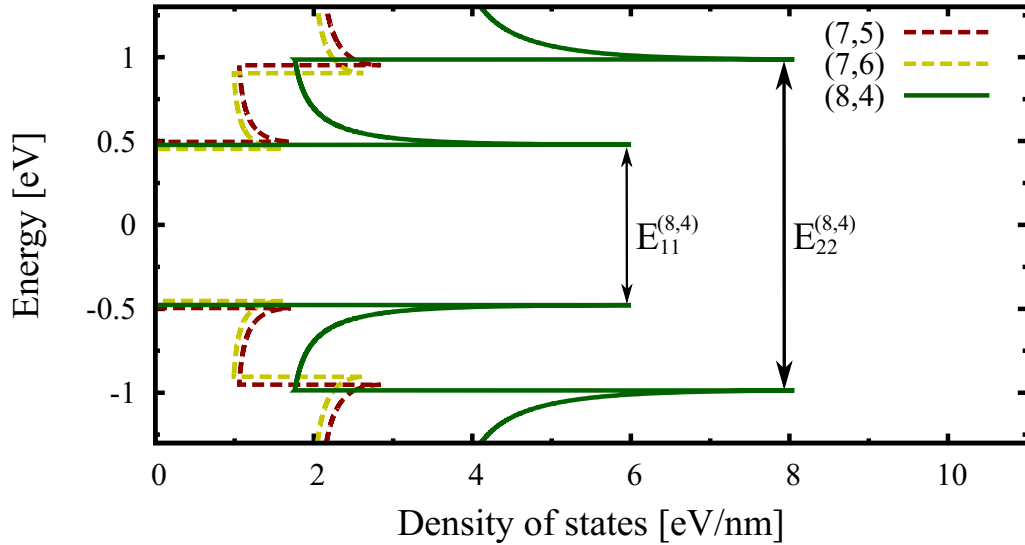


Figure 3.8: Density of States for the (7,5), (7,6) and (8,4) tube showing the characteristic one-dimensional divergence behavior towards the band edge scaling with $\varepsilon^{-\frac{1}{2}}$. The DOS is plotted for the in PLE and pump-probe experiments relevant first and second optical transitions E_{11} and E_{22} , [46].

3.1.5 Family Patterns: Metallic versus Semiconducting CNTs

Depending on their structure we showed how nanotubes can be divided according to their chiral indices into armchair, zig-zag and chiral tubes. As a consequence of folding the graphene sheet into nanotubes, only some of the in graphene available states will be allowed for the resulting tubes. If the allowed states will pass through the K -point, the resulting tube will be metallic, otherwise it will be semiconducting. Exploiting the results of the zone-folding scheme and applying the boundary conditions at the K -point, we get the condition whether a tube is semiconducting or metallic:

$$\mathbf{K} \cdot \mathbf{c} = \frac{1}{3}(\mathbf{k}_1 - \mathbf{k}_2) \cdot (n_1 \mathbf{a}_1 - n_2 \mathbf{a}_2) = m \cdot 2\pi, \quad (3.44)$$

with

$$m = \frac{n_1 - n_2}{3}, \quad (3.45)$$

depending on if the difference between the chiral indices can be divided by three without remainder. The semiconducting tube families split of into two subfamilies the $+1$ and -1 , whether the allowed line next to the K point is located on the KM or on the KT side.

Altogether we can embrace 3 families:

$$\left\{ \begin{array}{ll} \text{metallic} & \Leftrightarrow \quad \text{mod}_3(n_1 - n_2) = 0 \\ +1 \text{ semiconducting} & \Leftrightarrow \quad \text{mod}_3(n_1 - n_2) = +1 \\ -1 \text{ semiconducting} & \Leftrightarrow \quad \text{mod}_3(n_1 - n_2) = -1 \end{array} \right. \quad (3.46)$$

For our investigations of the photoluminescence process only semiconducting tubes are of interest, as they allow band-gap radiative recombination.

3.2 Phonon Modes - Optical and Acoustic Dispersions

Figure 3.9 displays the phonon dispersion of graphite. Filled dots are experimental values and open dots represent ab initio calculations of graphene. It can be seen that for optical phonons at the Γ and K point two sharp kinks occur which are called Kohn anomalies[48]. The phonon modes in the vicinity of these two points denoted with $\Gamma - E_{2g}$ and $K - A_1'$ exhibit a strong electron-phonon coupling [2]. At the Γ point the doubly degenerated E_{2g} mode splits up into a TO and LO mode. Since we constrain with our calculations on intravalley scattering processes, i.e. Γ -phonons the transferred phononic momentum is very small $q \approx 0$. We can validly approximate the dispersion of the optical phonons involved in our processes as constant with a value of $\hbar\omega_q^{\Gamma TO} \approx \epsilon_0^{\Gamma TO} = 192$ meV [47] for the TO mode. For acoustic phonons we assume a linear phonon dispersion around the Γ point [38], cp. Fig. 4.10: $\hbar\omega_q^{\Gamma LA} = \hbar c_s |q| \approx \beta^{\Gamma LA} |q|$, with the velocity of acoustic phonons being $c_s = 2 \times 10^4 \frac{m}{s}$ and the reduced Planck constant $\hbar = 0.658 \text{ eV fs}$ the slope of the approximated acoustic dispersion follows $\beta^{\Gamma LA} = 0.013 \text{ eVnm}$. Furthermore, we note that beside the optical and acoustic other important phonon modes in carbon nanotubes exist. A special unique in CNTs existing phonon mode is the radial breathing mode [49]. Within our investigations we revealed that the coupling strength is found to be to small and therefore it was concluded that this mode has not a decisive influence onto the ultrafast non-radiative relaxation processes within the considered conduction subbands.

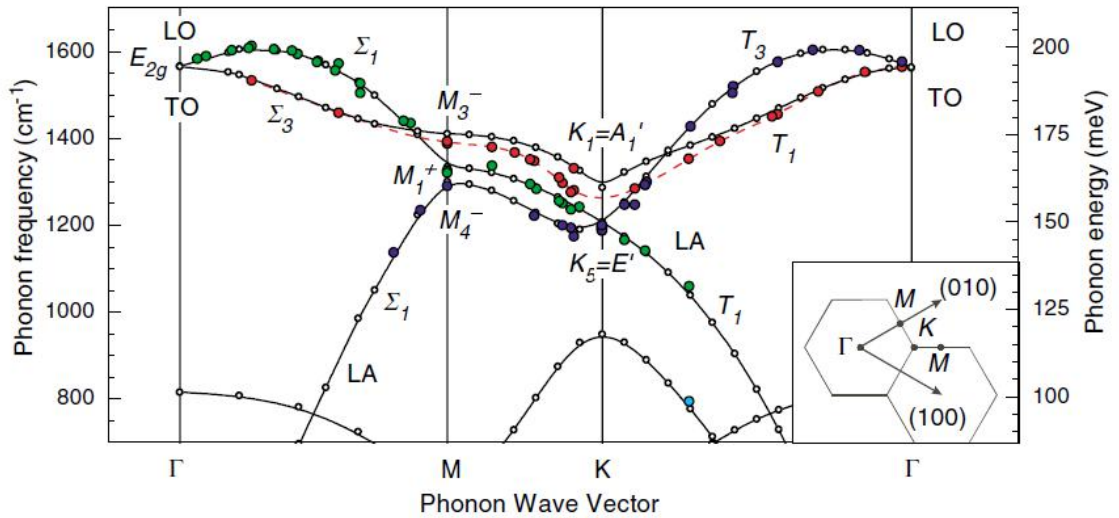


Figure 3.9: Phonon dispersion of graphite obtained from inelastic x-ray scattering (filled dots) and ab initio calculations (open dots). The longitudinal (LO) and transverse (TO) optical phonon branches are displayed exhibiting special kinks around the Γ and K point. Since the optical phonons can be assumed to be constant in vicinity of the Γ -point the acoustic branch exhibit an approximately linear dispersion. Picture taken from [47].

3.3 Matrix Elements Describing the Coupling

3.3.1 Between External Fields and the Nanotube: Optical Matrix Element (OME)

Through the external excitation of a solid with laser light in a pump-probe experiment or from a HgXe lamp of a photo-luminescence spectrometer electrons are excited from the valence to the conduction band. In theory this is viewed as an absorption process of a photon providing the energy for the electron transfer, mostly neglecting the very small but not vanishing photon momentum resulting in a vertical transition. The Hamiltonian that describes this coupling between the external field in the semi-classical treatment contains the scalar product of the vector potential $\mathbf{A}(t)$ with the optical matrix element $\mathbf{M}_{\mathbf{k}\mathbf{k}'}^{\lambda\lambda'}$. In second quantization the optical matrix element (OME) is given via the transition probability between two different quantum mechanical states represented by the graphene Bloch functions in tight-binding expressed by the linear combination of the atomic $2p_z$ orbitals. In the derivation of the $\mathbf{p} \cdot \mathbf{A}$ Hamiltonian the optical matrix element was introduced

$$\mathbf{M}_{\mathbf{k}\mathbf{k}'}^{\lambda\lambda'} = \int_{-\infty}^{+\infty} d^3\mathbf{r} \psi_{\mathbf{k}}^{\lambda*}(\mathbf{r}) \nabla_{\mathbf{r}} \psi_{\mathbf{k}'}^{\lambda'}(\mathbf{r}), \quad (3.47)$$

with the wave functions of the energy bands, which can be viewed as the summation of the Bloch functions of the carbon atoms A and B in the graphene unit cell. Within the nearest neighbor approximation for interband processes between valence and conduction bands the OME for graphene states:

$$\mathbf{M}_{\mathbf{k}\mathbf{k}'}^{V_s C_s} = \frac{M_c}{\sqrt{|\mathbf{f}_{\mathbf{k}}| - s_0^2 |\mathbf{f}_{\mathbf{k}}|^4}} \Re \left[\sum_{i=1}^3 e^{i\mathbf{k}\mathbf{b}_i} \frac{\mathbf{b}_i}{b_i} \mathbf{f}_{\mathbf{k}}^* \right] \quad (3.48)$$

with the constant optical matrix element for the two nearest neighbor atoms [50, 51]

$$M_c = \langle \phi(\mathbf{r} + \mathbf{R}_i) | \partial_z | \phi(\mathbf{r}) \rangle \quad (3.49)$$

which is 3.00145 nm^{-1} , calculated from the effective nucleus charge number $Z = 4.01286$ obtained from the variation of the hydrogen wave function for an overlap value of $s_0 = 0.13$ [52].

Without overlapping, i.e. $s_0 = 0$, the coefficients for the valence and conduction band state

$$C_A^{V_s, C_s}(\mathbf{k}) = \pm C_B^{V_s, C_s}(\mathbf{k}) \frac{\mathbf{f}_{\mathbf{k}}}{|\mathbf{f}_{\mathbf{k}}|} \quad (3.50)$$

where $\pm C_B^{V_s, C_s}(\mathbf{k}) = \pm \frac{1}{\sqrt{2}}$ with the minus denoting the conduction and the plus sign valence band. Inserting the quantized wave vector of graphene, cp. Eq. (3.36), i.e. applying zone folding, we can finally express the optical matrix element as a function of the chiral indices (n_1, n_2) , the subband index m and the continuous wave vector along the tube axis \mathbf{k}_z [53]

$$M_{k_z} = \frac{M_c}{2\sqrt{N_{12} \cdot |\mathbf{f}_{\mathbf{k}}|}} \left[(n_1 - n_2) \cos[C] - (2n_1 + n_2) \cos[A] + (n_1 + 2n_2) \cos[B] \right], \quad (3.51)$$

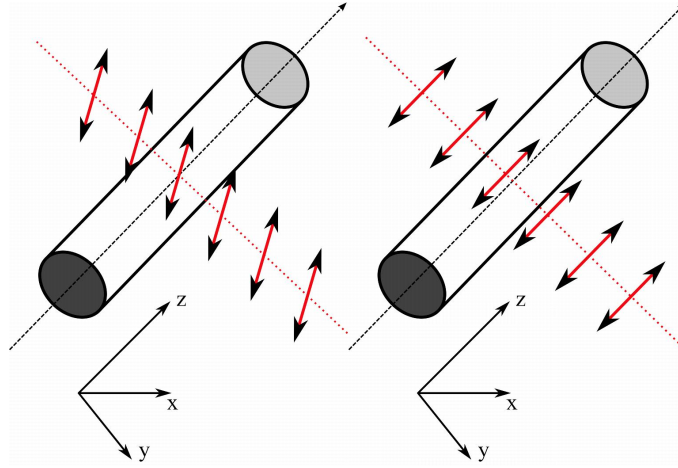


Figure 3.10: Light polarized perpendicular (left side) and parallel (right side) to the tube axis along the z-direction while the propagation is perpendicular to this axis

with

$$|f_k| = \sqrt{3 + 2 \cos[A] + 2 \cos[B] + 2 \cos[C]}. \quad (3.52)$$

According to different authors [54, 55] light which is polarized perpendicular (cp. Fig. 3.10) to the tube axis has no impact, originating in the optical selection rules from the quantum mechanical and depolarization ('Antenna') effects from classical electromagnetic theory. Thus taking only light parallel polarized to the nanotube axis into account allows to focus the optical matrix element to its z-component cp. Eq. (3.51).

3.3.2 Within the Nanotube: Electron-Phonon Coupling (EPC)

We repeat the electron-phonon interaction the Hamiltonian from chapter 2:

$$H_{car-phon} = \sum_{\lambda\lambda'\mathbf{k}\gamma\mathbf{q}} \left(g_{\mathbf{k}\mathbf{q}}^{\lambda\lambda'\gamma} a_{\lambda\mathbf{k}+\mathbf{q}}^\dagger a_{\lambda'\mathbf{k}} b_{\gamma\mathbf{q}} + h.c. \right) \quad (3.53)$$

with the electron-phonon matrix element $g_{\mathbf{k}\mathbf{q}}^{\lambda\lambda'\gamma}$. For the case of CNTs we can rely on the matrix element of graphene and derive that for CNTs. Under the premiss that curvature effects do not have a remarkably impact on the electron-phonon coupling in tubes, the following equalization can be done [56]:

$$|g_{tu}|^2 A_{tu} = |g_{gr}|^2 A_{gr}, \quad (3.54)$$

with $A_{gr} = \frac{\sqrt{3}}{2}a_0^2$ and $A_{tu} = |\mathbf{c} \times \mathbf{a}| = \pi da$ being the unit cell area of graphene and the carbon nanotube, respectively. Since \mathbf{a} and \mathbf{c} are perpendicular, having $|\mathbf{c}| = \pi d$ we yield:

$$|g_{tu}|^2 = |g_{gr}|^2 \frac{\sqrt{3}a_0^2}{2\pi L} \frac{1}{d}, \quad (3.55)$$

whereby the length of the tube L enters through a normalization factor $\frac{1}{N}$ from the EPC element as shown in [56] multiplied with the length of the unit cell a ($a = \frac{L}{N}$).

Intra- and Intersubband Coupling with Transverse Optical Phonons

Modeling the electronic dynamics in the two lowest lying subbands we have to consider intraband coupling elements which we also assume for interband scattering between the conduction subbands.

$$|g_{gr}^{\lambda\lambda\gamma}|^2 = \langle g_{\Gamma,gr}^2 \rangle_F [1 \mp \cos(\Theta + \Theta')]. \quad (3.56)$$

The \mp refers to the phonon modes $\gamma = \text{LO/TO}$ with Θ being the angle between the electronic \mathbf{k} and the phononic \mathbf{q} vector and Θ' between $\mathbf{k} + \mathbf{q}$. With the equalization Eq. (3.54) we obtain for nanotubes:

$$|g_{tu}^{\lambda\lambda\gamma}|^2 = \langle g_{\Gamma,gr}^2 \rangle_F \frac{\sqrt{3}a_0^2}{2\pi dL} [1 \mp \cos(\Theta + \Theta')]. \quad (3.57)$$

Since in metallic nanotubes \mathbf{k} and \mathbf{q} are parallel to the tube axis, Θ' and Θ can only take the value 0 or π . Therefore, intraband coupling with LO phonons vanishes and leads to a factor of 2 for the coupling strength with the Γ TO phonon mode. This implies that inter- and intrasubband relaxation is driven by Γ TO phonons and we finally have:

$$|g_{tu}^{\Gamma\text{TO}}|^2 = \langle g_{\Gamma,gr}^2 \rangle_F \frac{\sqrt{3}a_0^2}{\pi dL}. \quad (3.58)$$

In semiconducting nanotubes the band structure is parabolic and exhibit a band gap in the few hundred meV range. To extrapolate the formulas, which are derived for metallic nanotubes one would have to take an extra angle dependence into account [48].

Intrasubband Coupling with Longitudinal Acoustic Phonons

To obtain the carrier-phonon coupling elements, we follow the derivation for graphene from Ref. [38]:

$$|g_{gr}|^2 = \frac{D^2 \hbar}{2m\omega_q A_{gr}} |q|^2 [1 + \mu\lambda \cos(\phi_{k-q} - \phi_k)], \quad (3.59)$$

$\mu, \lambda = \pm 1$ is the chirality index with $\mu, \lambda = 1$ for the conduction band. In the case of intraband coupling $\phi_{k-q} = \phi_k$ as also $\lambda = \mu$ yielding

$$|g_{tu}^{\Gamma\text{LA}}(q)|^2 = \frac{\hbar^2}{L} \frac{D^2}{\pi m \beta_{\Gamma\text{LA}}} \frac{1}{d} |q|, \quad (3.60)$$

with the deformation potential $D = 16\text{ eV}$ and the mass density of graphene $m = 7,6 \cdot 10^{-8} \frac{\text{g}}{\text{cm}^2}$. We point out the explicit dependence on the modulus of the phonon momentum $|q|$, which is in contrast to the corresponding coupling element for optical phonons.

3.4 At a Glance

In this chapter we introduced the special properties of carbon nanotubes onto their one-dimensional confinement of the acting quasiparticles. We derived the band structure stemming from graphene, the optical matrix element including the allowed optical transitions and the electron-phonon coupling for acoustic and optical phonons in CNTs. Beside this, the different possibilities of rolling up the graphene sheet produce a huge variety of tubes which have different basic features, e.g. exhibiting a band gap or not, i.e. being semiconducting or metallic in contrast to its mother material being only the latter one.

4

Relaxation Dynamics in Semiconducting Nanotubes

The physical process of photoluminescence excitation (PLE) is in the case of CNTs the primary process for assigning the tube chirality by their optical transition energies E_{11} and E_{22} . The main aim of this chapter is to understand the non-radiative relaxation process of optically excited non-equilibrium carriers through scattering with optical and acoustic phonons. The calculations are based on the density matrix theory giving microscopic access to in time and momentum resolved carrier dynamics. It is major challenge to distinguish the different contributions of the experimentally observed differential transmission spectra and their resulting relaxation times. Comparing the experimental spectra to theoretical calculations the observed relaxation times can be addressed to inter- and intrasubband carrier scattering with optical and acoustic phonons. The relaxation times extracted from the obtained dynamics are offering a direct comparison to recent two-color pump-probe experiments done by O. Dyatlova in the group of Prof. U. Woggon [16, 17]. Due to the flexible control of the input parameters like the duration and frequency of the exciting pulse it is possible to adapt the variation of the pump and probe energy to the experimental investigations. The developed theory allows moreover the simulation for a wide range of tubes opening the analysis on global behaviors like diameter and chirality dependence for semiconducting carbon nanotubes.

4.1 Experimental Techniques on Nanotubes

The experimental techniques on carbon nanotubes lead to specific insights of their optical and electronic and phononic properties. Raman spectroscopy enables the characterization of different phonon modes occurring in a tube and also their coupling strength with electrons [57, 49]. Photoluminescence excitation (PLE) spectroscopy allows the specific identification of a CNT by its unique optical transition energies. This works only for semiconducting tubes since a band gap is a prerequisite. The intensities emitted by the tubes contained in the sample are measured (there are always more than one tube in a sample) by driving a range of excitation wavelengths through. Pump-probe spectroscopy can determine relaxation times within the process of PLE resolving timescales down to femtoseconds [58].

4.1.1 Photoluminescence Excitation (PLE)

The PLE technique is performed by analyzing the emission spectra of a material while tuning the energy of the excitation photons. No emission means that the excitation energy is below the band gap. PLE is the process of emission of light (photons) from a solid that is in the state of lower energy and after absorption of light at high frequency gets into an excited state of non-equilibrium. The carrier relaxation towards an equilibrium ground state causes the emission of a photon whose energy is related to the band gap value of the material [6]. For CNTs this process is assigned to the well defined optical transition energies E_{ii} with $i = 1, 2$ exhibiting divergences in the density of states, the Van Hove Singularities that dominate the process of light absorption and emission, cp.

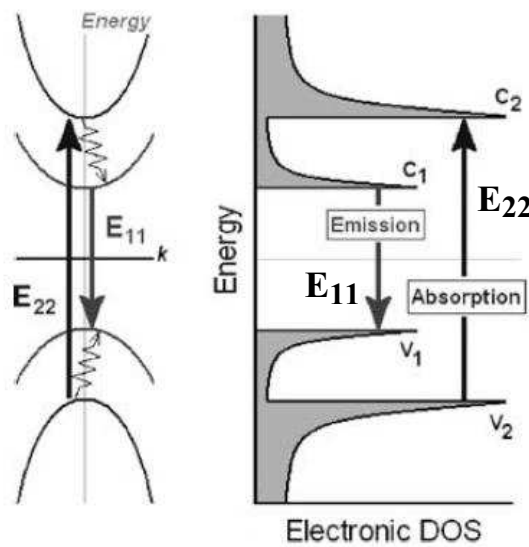


Figure 4.1: The process of optical absorption and emission within the single particle picture for photoluminescence excitation (PLE), reflecting the scientific knowledge in 2007, adapted from [6].

Process	Scattering partners	Energy region	Timescale
Absorption	electron-photon	E_{22}	t_{pulse} dependent
Relaxation	electron-phonon	E_{22} to E_{11}	hundred of fs up to ps
Emission	electron-photon	E_{11}	ns

Table 4.1: Identifying the subprocesses of photoluminescence excitation (PLE) assigning within which energy region which scattering partners are leading to different relaxation timescales. We note that the PLE process covers a range of 10^{-6} in time.

the right side of Fig. 4.1.

Bachilo et al. published spectrofluorimetric measurements on isolated single walled carbon nanotubes in aqueous surfactant suspensions [14]. The authors obtained distinct electronic absorption

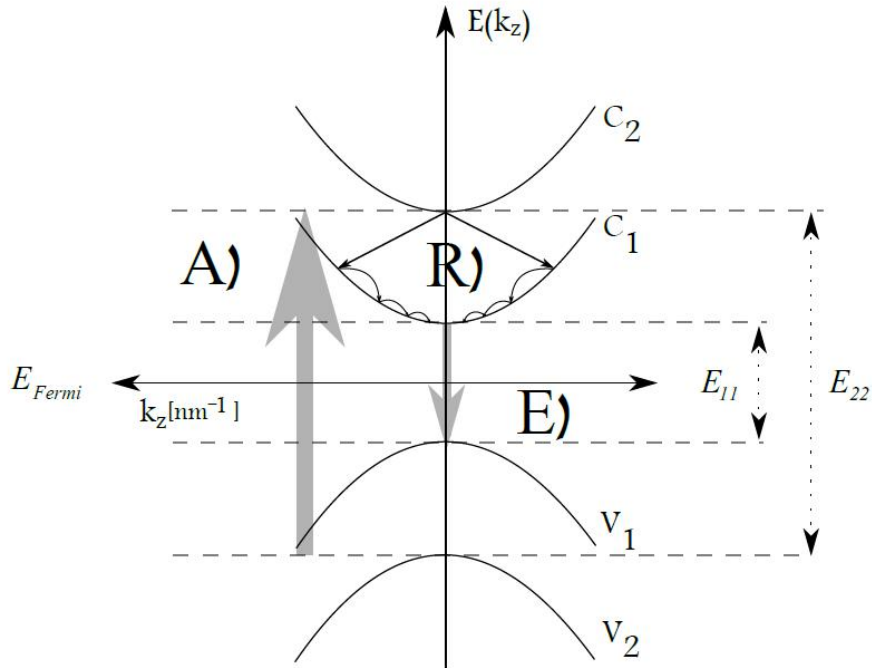


Figure 4.2: PLE in greater detail: A) generating non-equilibrium carriers via photon absorption with the following redistribution R) through scattering with optical and acoustic phonons and final radiative recombination under photon emission E) for a semiconducting nanotube. For the relaxation of the holes we assume at this stage a symmetric behavior of the scattering dynamics with the same phonon modes as for the electrons.

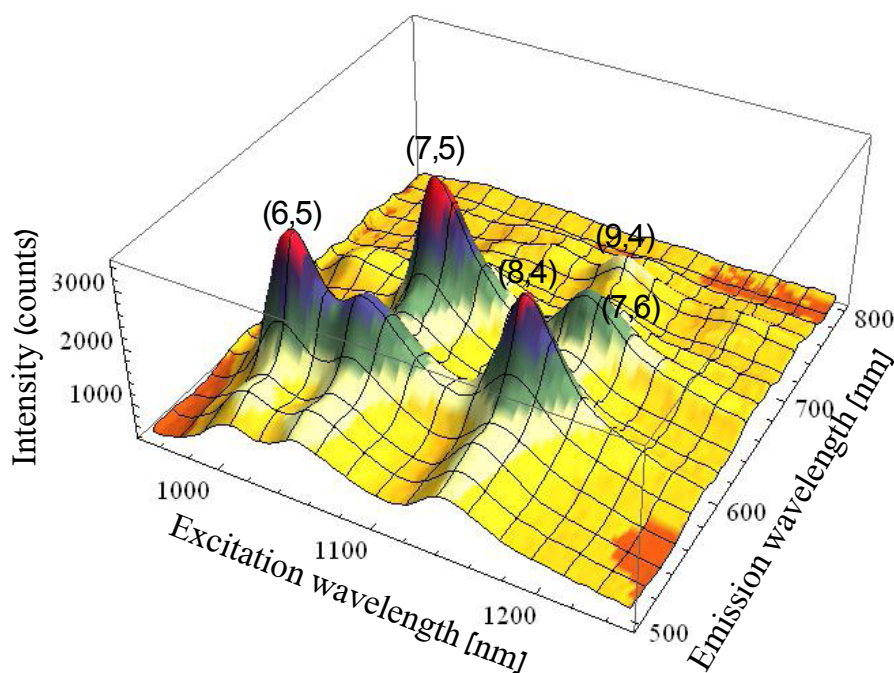


Figure 4.3: My own PLE map recorded with the friendly permission and help from Dr. A. Setaro in the group of Prof. S. Reich. The measured intensity of the emission is plotted over the excitation and emission wavelength. The sample contained (7,5), (7,6), (6,5), (9,4) and (8,4) tubes identified through their unique transition energies E_{22} for absorption and E_{11} for emission.

and emission transitions for more than 30 different tube species. Combining the measured results with resonant Raman data, enabled them to associate each optical transition to a certain nanotube identified by their chiral indices (n_1, n_2) . By mapping the luminescence spectra as a function of the excitation energy they created a two dimensional plot.

The largest intensities of the joint density of states (JDOS) in correspondence of the van-Hove singularities make the PLE process essentially given by the photo absorption at the E_{22} and the photo emission at the E_{11} transition. As these transitions are unique for a certain (n_1, n_2) species, their determination allows the clear identification of different CNTs. Through the confinement in one dimension the PLE charts show sharp peaks for the different chiralities. The general description of the PLE process in CNTs can be found e.g. in [6, 59]. Figure 4.1 displays a sketch of photoluminescence excitation with the state of knowledge in the year 2007 including the radiative and non-radiative subprocesses. In table 4.1 the timescales on which the respective processes take place are summarized. By our investigations we gained a detailed insight in the process of non-radiative carrier relaxation between absorption and emission. The absorption, emission and relaxation processes for resonant excitation are shown in greater detail in Fig. 4.2. We extracted how carriers relax from the excited non-equilibrium state into the thermalized equilibrium one

under the emission of transverse optical (TO) and longitudinal acoustic (LA) phonons between the lowest conduction subbands C_2 and C_1 before radiative recombination takes place. For the relaxation dynamics between the absorption at E_{22} and the recombination at E_{11} , we are able to address the corresponding phonon modes and how they can be assigned via the obtained relaxation times in the differential decay spectra of corresponding experiments [16, 17]. To understand how to measure and obtain such a spectrum I did my own PLE chart in the group of Prof. S. Reich, cp. Fig. 4.3. The plot shows the observed emission intensity over the excitation and emission wavelength. Cutting along these axes yields the emission and absorption at fixed energy points. The transition energies of absorption E_{22} and emission E_{11} can be used to identify the tubes present in the sample. As the excitation source a HgXe lamp has been used and the desired wavelength was selected through a grating. The emission spectrum got recorded with an InGaAs detector. Repeating this process under different excitation wavelengths we obtained the PLE chart.

4.1.2 Ultrafast Pump-Probe Experiments

While continuous wave photoemission spectroscopy provides insight into the structure of the electronic density of states of the material by providing the position of the Van Hove singularities, the relaxation dynamics in a solid state can be studied through time resolved spectroscopic techniques. Among them, pump-probe spectroscopy can investigate the ultrafast processes which occur between different energy levels like the subbands in carbon nanotubes. The structure is excited with a strong pump laser pulse, i.e. with a high intensity, creating a non-equilibrium carrier density at a certain energy point through a defined wavelength of the pump laser. In the band to band transition picture this is viewed as the pumping of electrons from the valence into the empty conduction

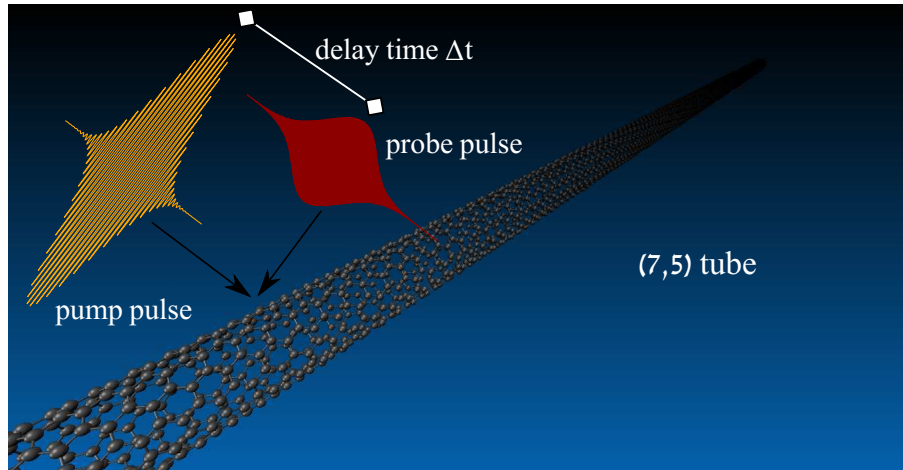


Figure 4.4: Sketch of pump-probe spectroscopy for the (7,5) carbon nanotube related to the upcoming experiments [17]. The tube is excited via a strong pump pulse with a width of $t^{pump} \approx 190$ fs followed by weaker probe pulse with $t^{probe} \approx 300$ fs within a delay time Δt .

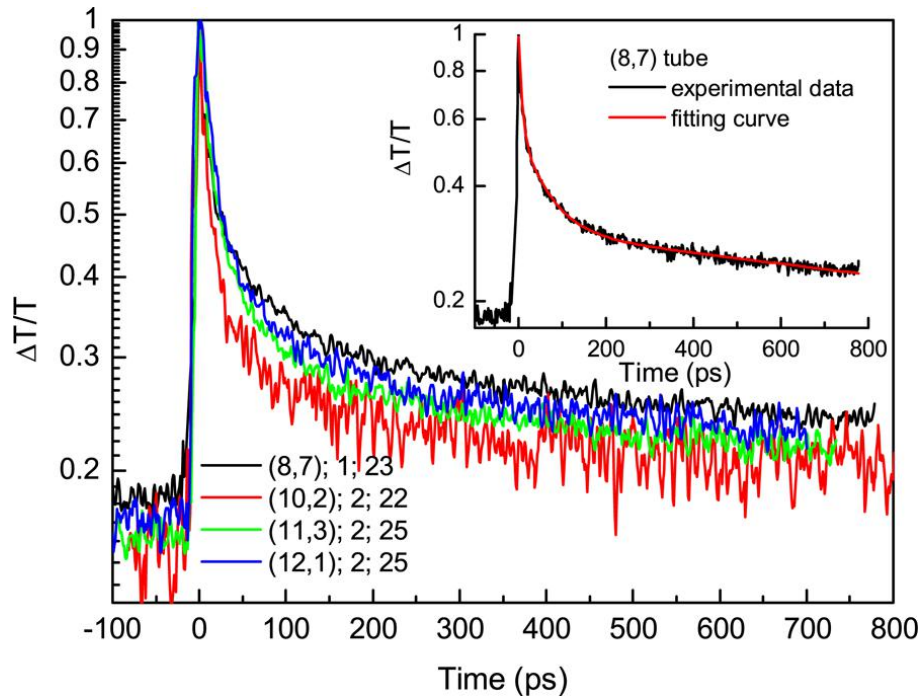


Figure 4.5: Differential transmission curves recorded from two-color pump-probe measurements. The measured transmission signal resulting from both pulses $\Delta T = \Delta T(\Delta t)$ related to the signal T without the pump pulse yields the differential transmission spectrum (DTS) $\frac{\Delta T}{T}$ with respect to the delay time Δt between the pump and probe pulse. Pump and probe energies are chosen resonant to the transition energies E_{22} and E_{11} . The inset displays the fitting with a bi-exponential decay function, taken from [16].

subband. A second weaker laser beam, called probe, is used to monitor the change in the induced carrier density at defined energies. When the probe energy equals the pump energy one would speak of a one-color pump-probe experiment. For the multi-subband structure of single-walled carbon nanotubes, at this constant energy levels both of the lowest lying subbands can be involved. In contrast, in a two-color pump-probe experiment the wavelengths of the two lasers are different, which will be in the focus of the experiments described by our calculations in section 4.4.

Differential Transmission Curves-Assigning of Relaxation Processes

A number of one- and two-color pump-probe experiments measuring the relaxation dynamics of non-equilibrium carriers have been performed, revealing different relaxation times and offering a variety of possible explanations. Here we give a short overview of these experimental results within the last years in the field of carrier relaxation dynamics in carbon nanotubes [60, 61, 58, 62, 63, 64, 65] which is adapted from our previous publication [16]. Ostojic et al. observed decay times within two different timescales. One in the range between 5 to 20 ps and a faster component

between 0.3 to 1.2 ps. The slower times are viewed as the lower boundary of radiative lifetimes resulting from interband carrier recombination, while the faster times have been identified with the non-radiative intraband relaxation of carriers in tubes that have been excited non-resonantly [60]. With ultrashort sub 10 fs pump pulses Manzoni *et al.* resolved intersubband exciton relaxation and obtained a decay time constant of 40 fs [58]. Within a two-dimensional nonlinear optical experiment on nanotubes Graham *et al.* observed also a bi-exponential decay with a fast time component of 0.12 fs and a slower one of 1.25 ps [65]. In experiment the transmission signal over the delay time between the pump and probe pulses are measured, cp. Fig. 4.5. On a first view such curves, being plotted in half logarithmic scale and normalized to one, can be divided into different stages. First, the transmission signal raises within a few hundred femtoseconds to its maximum, followed by a multi-exponential decay of the signal. In all experiments of Dyatlova *et al.* a three-exponential decay of the differential transmission signal is observed, whereby the samples differ in their composition. In Ref. [16] the sample contained up to 17 different tube species and while in Ref. [17] the samples have been chirality enriched with a dominating tube specie. In both cases the fastest relaxation time τ_1 of the signal decay within the first few picoseconds is followed by a second time τ_2 ranging from approximately 7 up to 50 ps. Finally a third component τ_3 on a timescale of hundreds of picoseconds up to nanoseconds has been measured. With our calculations we reveal relaxation times from intra- and intersubband carrier dynamics via electron-phonon scattering from hundreds of femtoseconds up to the first picoseconds. These times we compared to the experimentally obtained fastest relaxation time τ_1 . The other two timescales are beyond the current state of our simulation, which could be embedded by extending the model to the process of radiative recombination of the relaxed carriers at E_{11} . The task is now to interpret the observed decay times with our theoretical microscopic model and to assign which electron-phonon scattering processes leading to them. From our calculations, cp. Eq. (2.17) and (2.18) we plot the temporal evolution of the electronic population $\rho_\epsilon^l(t)$ within the subbands $l = C_2, C_1$ at certain points in energy. The occupation probabilities of the exemplary semiconducting (23, 0) zig-zag tube for the

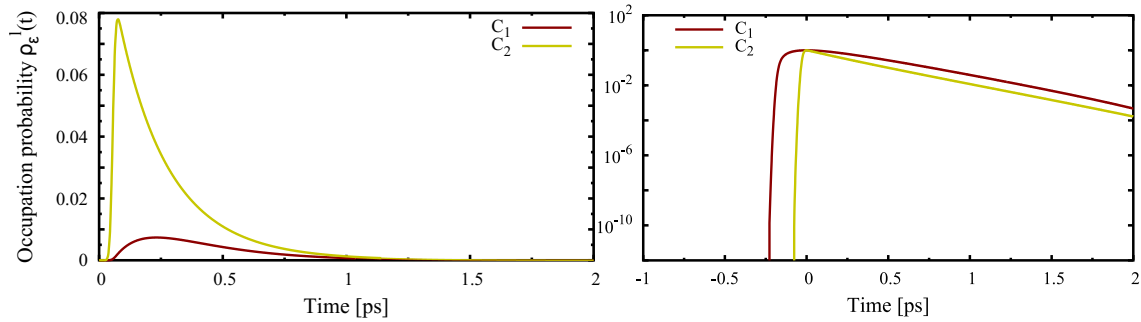


Figure 4.6: Occupation probabilities ρ_ϵ^l fitted at E_{exc} within C_2 and lowered via optical phonon scattering within C_1 at $E_{exc} - \epsilon_{q_0}^{\Gamma\text{TO}}$. On the left side the occupations are plotted linear over time, exhibiting a much smaller but broadened distribution (red line) arising after intersubband scattering with optical phonons. The right side displays the logarithmic version with both curves shifted to zero and normalized to 1.

4.1. EXPERIMENTAL TECHNIQUES ON NANOTUBES

upper subband C_2 at the excitation energy E_{exc} and lower C_1 at $E_{exc} - \epsilon_{q_0}^{\Gamma_{TO}}$ are displayed in Fig. 4.6. On the left side the linear over time and on the right side the half-logarithmic representation with their maxima normalized to 1 and shifted to zero are shown. The raise of the occupation in the upper subband reflects the excitation via the external pulse by building up the electronic occupation probability to its maximum. For the lower subband the scattered electronic distribution is broadened and lowered. In the half-logarithmic representation the subsequent decay of the occupation probability shows a linear dependence within the first 2 picoseconds. Comparing the curves for both subbands in the half-logarithmic representation the raise of the occupation of the lower is slower than for the upper subband. This broadened slower rise of the electronic distribution reflects the process of intersubband scattering with optical phonons and can be identified with the observed raise of the experimental differential transmission signal. The rising times for the latter one can be estimated to a few hundred femtoseconds [66] which is in good agreement with the theoretical simulated relaxation times we will extract in the next sections.

4.1.3 Dielectric Screening in Single Walled Carbon Nanotubes

The surrounding medium of a nanosystem can weaken the Coulomb interactions and therefore reduce the excitonic binding energies. This has been theoretically and experimentally demonstrated for single walled carbon nanotubes [67, 68]. In a medium with a relative dielectric constant $\epsilon_r = 1$, the electron-electron as also the electron-hole interaction is interfered via the Coulomb interaction. The first leads to a repulsive renormalization of the band gap while the attractive coupling of the latter forms a bound state, i.e. excitons which is an important effect in carbon nanotubes [69, 70, 71, 72, 73, 74]. The solution samples mainly containing (7, 5), (7, 6) and (8, 7) tubes investigated by Dyatlova et al. which we compare with our theoretical studies on relaxation dynamics exhibit an averaged dielectric background constant $\epsilon_{bg} = 1.8 \pm 0.1$. The excitonic binding energies E_{ii}^b for the first three transitions of the semiconducting (10, 0) zig-zag tube are plotted as a function of the dielectric background constants ϵ_{bg} , cp. Fig. 4.7 (a). Apparently for ϵ_{bg} in the range between 1 and 2 the excitonic binding energies E_{22}^b and E_{11}^b for transitions being important in our simulation are reduced approximately by 55%. With an increasing ϵ_{bg} the absorption spectrum of the lowest excitonic transition E_{11} of the (7, 5) tube shifts towards the free-particle Van Hove singularity, cp. Fig. 4.7 (b). These results indicate that the electron-hole interaction is strongly weakened via an increasing external screening and therefore the formation of excitons is suppressed. From this, we can state that for tubes in samples with high dielectric screening and therefore weak Coulomb interaction it is justified to focus on electron-phonon interaction since this mechanism is dominating the carrier relaxation.

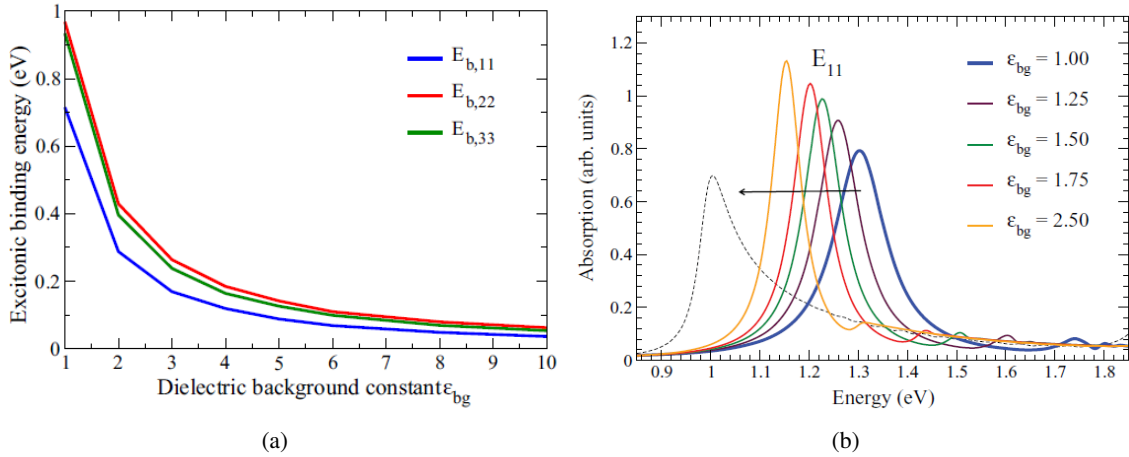


Figure 4.7: (a) The influence of the dielectric background constant ϵ_{bg} on the excitonic binding energy E_{ii}^b for the first three transitions of the semiconducting (10, 0) zig-zag tube. (b) Absorption spectra for the (7, 5) tube for different ϵ_{bg} . With increasing values it exhibits a red shift to lower energies towards the free-particle Van Hove singularities, taken from [67, 68].

4.2 Carrier Relaxation Dynamics via Electron-Phonon Scattering

4.2.1 Simulation of the Excitation

The excitation of the tube with light is achieved within a semi-classical treatment expressed via the light matter Hamiltonian, cp. section 2.1:

$$H_{car-lf} = i\hbar \frac{e_0}{m_0} \sum_{\lambda \lambda'} \sum_{\mathbf{k} \mathbf{k}'} \mathbf{M}_{\mathbf{k} \mathbf{k}'}^{\lambda \lambda'} \cdot \mathbf{A}(t) a_{\lambda \mathbf{k}}^\dagger a_{\lambda' \mathbf{k}'}. \quad (4.1)$$

The vector potential $\mathbf{A}(t)$ (within dipole approximation) builds up a polarization between the second lowest valence and conduction bands V_2 and C_2 . It contains a slow varying Gaussian shaped envelope with an amplitude A_0 and an exponential part with a temporal pulse width σ_t and a cosine part modeling the fast oscillations driven by the external excitation frequency ω_{exc} :

$$A(t) = A_0 \exp\left[\frac{-t^2}{2\sigma_t^2}\right] \cos\left(\frac{E_{exc}}{\hbar} t\right), \quad (4.2)$$

with the excitation frequency corresponding to the excitation energy $\hbar\omega_{exc} = E_{exc}$.

The width of the pulse duration t_{pulse} is given in Full Width Half Maximum (FWHM) which is related to σ_t via $t_{pulse} = 2\sqrt{2\ln 2} \sigma_t$. We compare pulses with different durations in Fig. 4.8. An ultra short pulse (yellow) with a width of $t_{pulse} = 28$ fs in FWHM and an amplitude of $A_0 = 0.13 \left[\frac{\text{eV fs}}{\text{e}_0 \text{ nm}}\right]$, which we used in the most of our theoretical investigations in comparison to a five times wider

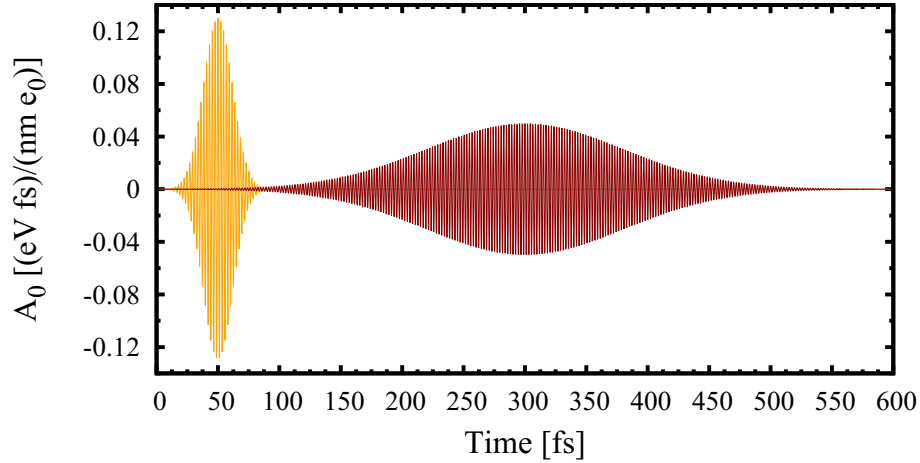


Figure 4.8: Gaussian shaped excitation pulses $A(t)$ over time: a) short pulse width of $t_{pulse} = 28$ fs (FWHM) and an amplitude of $A_0 = 0.13 \left[\frac{\text{eV fs}}{\text{e}_0 \text{ nm}}\right]$. b) five times larger pulse width of $t_{pulse} = 190$ fs and $A_0 = 0.05 \left[\frac{\text{eV fs}}{\text{e}_0 \text{ nm}}\right]$ as used in the simulation for experiment [17]. The pulses are shifted to the maximum of their amplitude to avoid losses within the numerical simulation.

pulse (red) with $t_{pulse} = 190$ fs and $A_0 = 0.05 \left[\frac{\text{eVfs}}{\text{e}_0 \text{ nm}} \right]$ according to the setup used in the experiment of Dyatlova et al. [17] are plotted. The amplitude is chosen appropriate to keep the area under the envelope, i.e. the energy of the pulse constantly small to prevent high electronic occupation probabilities. Otherwise, since we are dealing with the Boltzmann-Equation, cp. Eq. (2.35) strong Pauli-Blocking would show up.

4.2.2 Relaxation Channels in Semiconducting Carbon Nanotubes

The one-dimensional band structure of single-walled carbon nanotubes around the K-points can be viewed within the zone folding approximation as conic sections of the Dirac cone in graphene, cp. section 3.1.3. Depending whether the cutting lines hit the K-point or not a linear (without band gap) or a parabolic band structure exhibiting a band gap in the eV range is obtained dividing the tubes in metallic and semiconducting, respectively [2]. For our investigations of the photoluminescence excitation only semiconducting nanotubes are of interest, since a band gap for radiative recombination is necessary. The channels for the electronic relaxation processes via scattering with optical phonons are sketched in Fig. 4.9. We assume in the vicinity of the K-point mirror symmetry of the valence and conduction subbands with respect to the Fermi energy E_F , cp. section 3.1.1. Furthermore, in the case of zig-zag tubes the parabolic band structure is also mirror symmetric respectively to the energy axis (y-axis). Optical excitation of a tube around the K-point at a certain energy implies the excitation of two points in energy cutting the parabola. Therefore, a relaxation

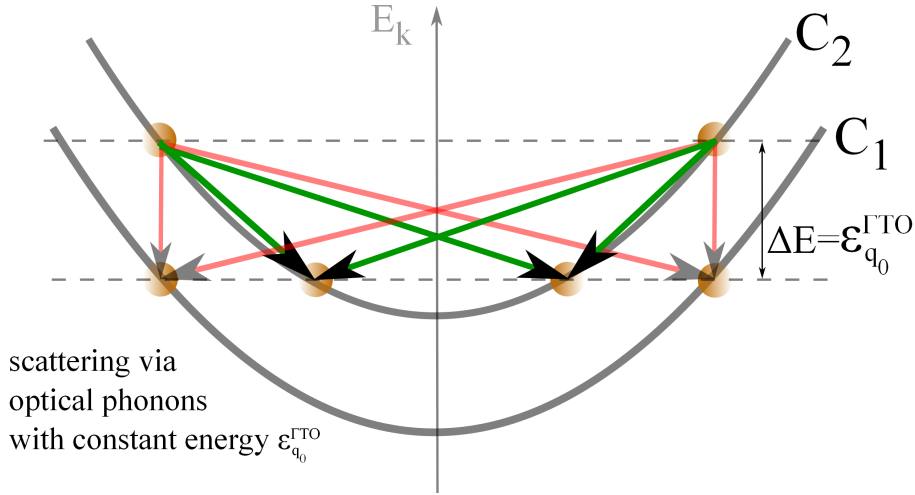


Figure 4.9: Sketch of the intra- and intersubband relaxation channels of a semiconducting zig-zag tube. Green arrows depict intra- and red intersubband scattering via optical phonons. The optical excitation takes place at a constant energy and hence at the two cutting points with the C_2 parabola. Due to mirror symmetry we can simulate the relaxation on one side of the parabola taking both relaxation channels into account by doubling the electron-phonon coupling.

4.2. CARRIER RELAXATION DYNAMICS VIA ELECTRON-PHONON SCATTERING

process with a constant optical phonon energy includes two relaxation channels as depicted for the case of intra- and intersubband scattering with green and red arrows, respectively. Because of the latter described mirror symmetry, we can simulate the relaxation dynamics at one side of the parabola and take the second scattering channel into account by a 2 times stronger electron-phonon coupling element. For acoustic phonons the phonon energy is not a constant value. The phonon dispersion is approximated as a linear function around the Γ -point of graphene and further adapted to carbon nanotubes. In Fig. 4.10 the scattering mechanism with acoustic phonons in nanotubes is sketched. A scattering event between a carrier and an acoustic phonon is only possible, when the electronic scattering process in momentum and energy matches the linear approximated phononic dispersion. From Eq. (2.47) we can estimate, that within the relevant region of the relaxation dynamics the acoustic phonons can reach a maximum energy of about 40 meV. Because the energy of an acoustic phonon failed to be large enough to overcome the energetic distance between the concerned subbands an intersubband-scattering is unlikely and therefore not investigated.

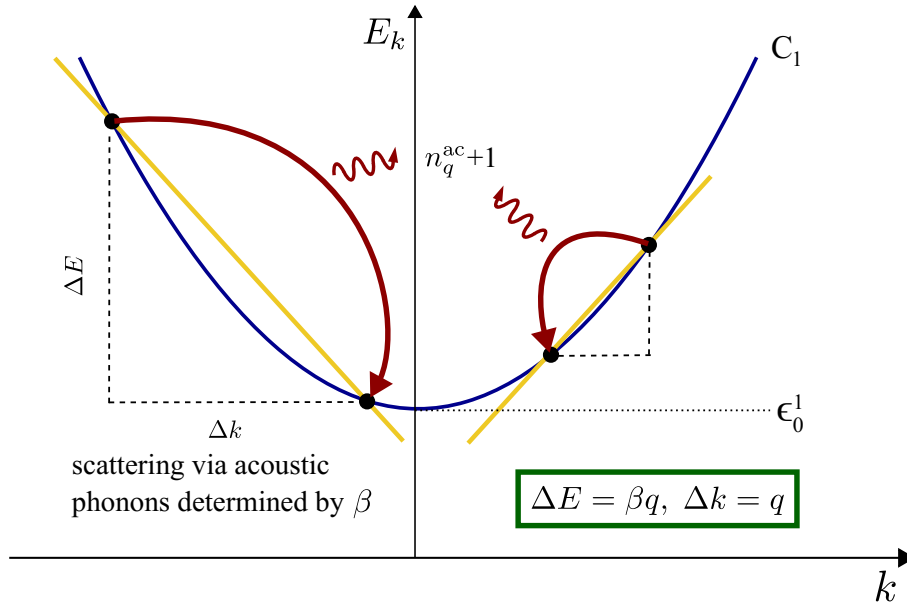


Figure 4.10: Sketch of exemplary intraband scattering processes via acoustic phonons with a linear phonon dispersion (orange lines) along the parabolic approximated electronic band structure of a random semiconducting carbon nanotube. For scattering towards the band edge the necessary phonon momentum is smaller than for scattering events starting further away at higher energies. We note that the slope of the acoustic phonon dispersion is much lower than displayed in the sketch. Picture taken from [75].

4.2.3 Intrasubband Scattering: One-Color Pump-Probe

We start with the case of intrasubband relaxation dynamics considering optical and acoustic phonon modes first separately and finally together. From this we compare the influence of the electronic relaxation behavior and emphasize the competition of the phonon mode dependent

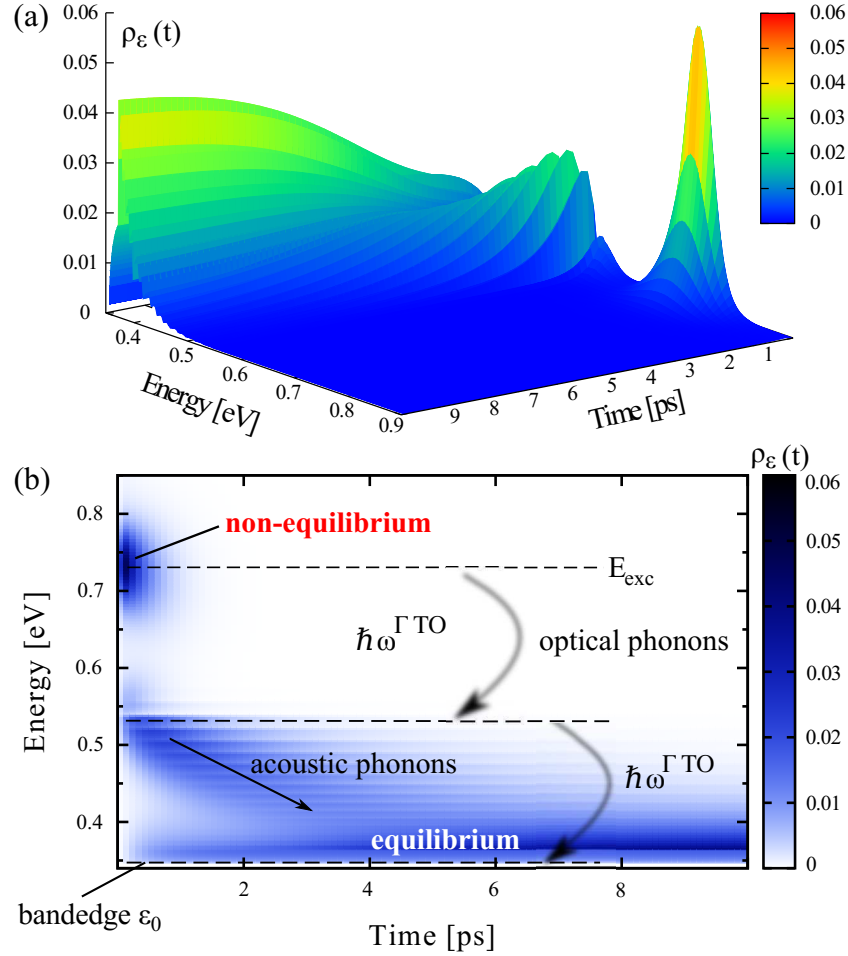


Figure 4.11: Relaxation dynamics of optically excited electrons for the (14,1) tube. Panel (a) displays the electronic occupation probability $\rho_\epsilon^{C_1}(t)$ in the lowest subband C_1 resolved in energy and time. A Gaussian-like non-equilibrium carrier distribution at 0.74 eV is generated via optical pumping of carriers at $E_{exc} = 1.47$ eV. Within a few picoseconds the carriers relaxed by scattering with optical and acoustic phonons towards the band edge into equilibrium, cp. the Fermi-like distribution. In panel (b) the discrete and continuous acting of the optical and acoustic relaxation behavior with a contour plot is displayed, taken from [76].

induced relaxation channels. Our here presented investigations and results are published in [76]. Through the evaluation of the coupled dynamical equations of the microscopic polarization p_k and electronic occupations $\rho_k^{C_1}$ we are able to simulate the relaxation dynamics with optical (Γ_{TO}) and acoustic (Γ_{LA}) phonon modes for the exemplary (14, 1) semiconducting nanotube, cp. Fig. 4.11. Within the optical excitation via a Gaussian pulse with $t_{pulse} = 28$ fs (in FWHM), an amplitude of $A_0 = 0.13 \left[\frac{eVfs}{e_0nm} \right]$ and an excitation energy of $E_{exc} = 1.47$ eV corresponding to the E_{22} transition, a non-equilibrium distribution is generated around 0.74 eV, i.e. $E_{22}/2$ by lifting electrons from the valence to the conduction subband. We focus on the electronic dynamics, since the hole dynamics has no influence on the further electron relaxation. Therefore, we constrain to the conduction subbands within the band to band transition picture. The electrons are redistributed to energetically lower states by emission of optical phonons with a constant energy of $\varepsilon_{q_0}^{\Gamma_{TO}} = 0.192$ eV. From the energy region below 0.54 eV the carriers relax towards the band edge $\varepsilon_0^{C_1}$ in smaller getting energy steps via scattering with acoustic phonons. Finally the carrier distribution is going into equilibrium by building up a Fermi-like distribution around 0.35 eV $\approx \varepsilon_0^{C_1}$, cp. Fig. 4.11 (b). The entire process is subjected to the conservation of energy and momentum stemming from the Boltzmann equation (2.35) within the Markov approximation. For a detailed comparison we plotted the electronic occupation probability over energy at different times for the cases of intrasubband relaxation driven with (a) optical, (b) acoustic and (c) optical with acoustic phonons together, cp. Fig. 4.12.

(a) *Optical phonons:*

The relaxation process starts with a non-equilibrium electronic distribution at 0.74 eV and goes into the equilibrium state around 0.35 eV $\approx \varepsilon_0^{C_1}$. For the case of optical phonon scattering this takes up to 2 ps cp. Fig. 4.12 (a). We see a redistribution in discrete steps of the phonon energy $\varepsilon_{q_0}^{\Gamma_{TO}} = 0.192$ eV due to the energy conservation inherent Markovian dynamics. Therefore, within the available energy region of 0.39 eV two scattering processes are possible leading to pronounced carrier occupations at approximately 0.55 and 0.36 eV during the first hundreds of femtoseconds after the optical excitation. The pronounced Markovian kink raising at 0.54 eV reflects the singularity resulting from the analytical scattering prefactor $\mathfrak{X}_{k\mp}^{l\Gamma_{TO}} = 2\alpha_l \sqrt{k^2 \mp \frac{\varepsilon_{q_0}^{\Gamma_{TO}}}{\alpha_l}}$ in Eq. (2.35). The observed kink in the carrier occupation is an artifact of the Markov approximation [77]. A smooth Fermi function cannot be reached within the Markov approximation and without considering the Coulomb-induced carrier-carrier interaction. An exponential fit of the time-resolved occupation probability at the excitation energy yields an optical phonon-induced relaxation time of $\tau_{C_1}^{IA} = 360$ fs.

(b) *Acoustic phonons:*

The relaxation dynamics from the interaction with acoustic phonons is significant slower compared to optical phonons exceeding to a timescale of approximately 30 ps being fifteen times larger than with optical phonons. We also obtain an nearly six times larger relaxation time of $\tau_{C_1}^{IA} = 2.1$ ps. This can be ascribed to the almost flat acoustic phonon dispersion relation allowing scattering processes with small momentum transfer q , which conserve energy and momentum at the same time. Since the carrier-phonon coupling element scales with $|q|$, the relaxation dynamics governed by acoustic phonons is slowed down. Compared to the case of optical phonons, the relaxation is

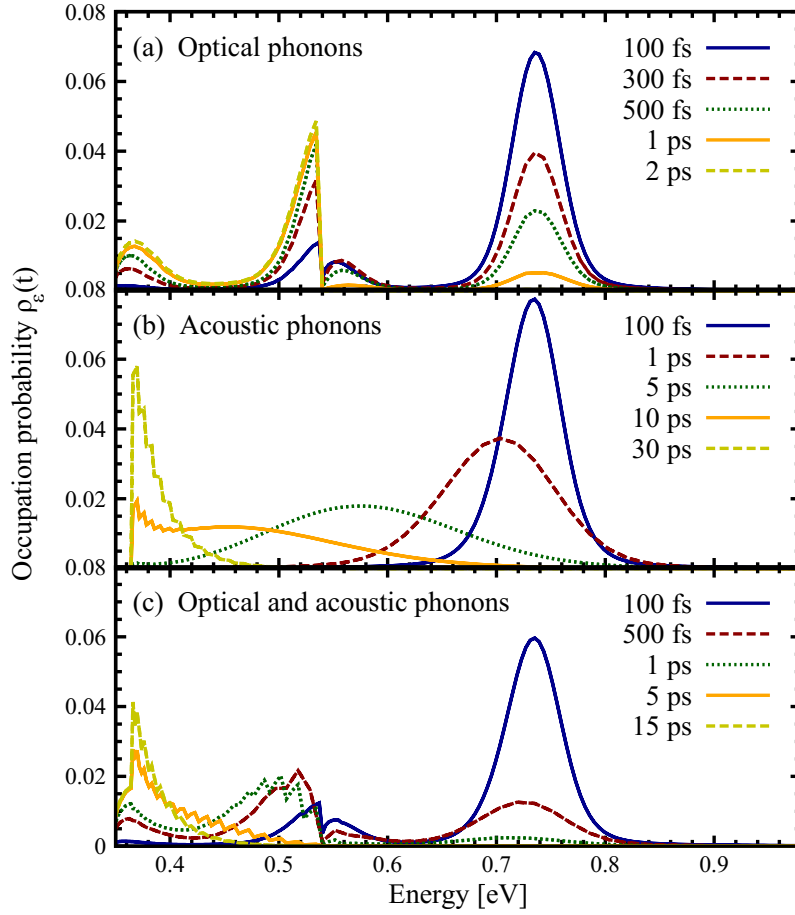


Figure 4.12: Snap shots of the electronic occupation probabilities $\rho_{\varepsilon}^{C_1}(t)$ over energy from Fig. 4.11 (a) at relevant times. The generated non-equilibrium electrons around 0.74eV are redistributed via electron-phonon interaction into equilibrium in the vicinity of the band edge of C_1 . In Comparison: electron dynamics through scattering with optical (a), acoustic (b), and (c) optical and acoustic phonons together. Figure taken from [76].

not characterized by discrete scattering steps, since the dispersion relation of the considered FLA phonons is linear. As a result, the excited carriers scatter in smaller getting steps to energetically lower states and can reach spectral regions in the vicinity of the band edge.

(c) *Optical and acoustic phonons:*

Allowing both phonon modes, optical and acoustic together we arrive at a relaxation dynamics passing on up to 15ps, cp. Fig. 4.12(c). Within the initial 500fs optical phonons dominate the carrier relaxation. Beyond, on a picoseconds time scale, acoustic phonons start to be important giving rise to a Fermi-like distribution. The Markov feature vanishes due to the additional relaxation channel via emission of acoustic phonons. The exponential fit reveals a decreased relaxation time of

$\tau_{C_1}^{\text{IA}} = 280$ fs reflecting the higher scattering efficiency via the doubled number of relaxation channels compared to the relaxation dynamics including only optical or acoustic phonons, respectively.

4.2.4 Excitation Energy

Referring to the equations of motion (2.17) and (2.18) the variation of the pump energy, i.e. E_{exc} under accordingly probing at the same energy will have an influence on the relaxation times depending on the respective dominating phonon modes. The exponential fit yielding the relaxation time is performed at the excitation energy, i.e. $E_{exc} = E_{pump} = E_{probe}$ modeling one-color pump-probe experiments. We vary E_{exc} from the former fixed value of 1.47 eV towards the band edge of the energetically lowest subband C_1 . When scattering with optical phonons the carrier dynamics becomes accelerated for reducing the energy from 1.47 to 1.18 eV resulting in a decrease of the relaxation time by approximately 44%, cp. the red solid line in Fig. 4.13 (b). The reason for this behavior originates in the previous focused scattering prefactor $\mathcal{X}_{k\mp}^{l\Gamma\text{TO}} = 2\alpha_l \sqrt{k^2 \mp \frac{\epsilon_{90}^{\Gamma\text{TO}}}{\alpha_l}}$. For lower excitation energies, the electronic momenta k involved in scattering processes become smaller leading to larger scattering rates, which scales with $1/\mathcal{X}_{k\mp}^{l\Gamma\text{TO}}$, cp. Eq. (2.42). In contrast, for acoustic phonons, the relaxation time increases by approximately 23%, cp. Fig. 4.13 (a). This can be understood through the dependence of the carrier-phonon coupling element on the phonon

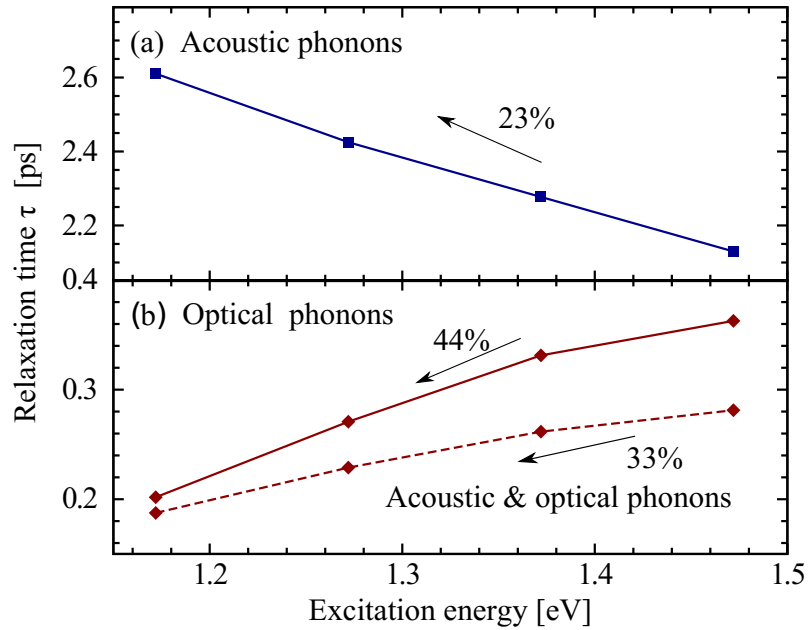


Figure 4.13: Influence of the excitation energy on the relaxation times for the (14,1) tube. We contrast the electronic relaxation time trend of the interaction with (a) acoustic, (b) only optical and optical and acoustic (dashed line) phonons, taken from [76].

momentum $|q|$. Reducing the excitation energy also limits the momentum $|q|$ to smaller values resulting in a slowed-down relaxation dynamics, i. e. the relaxation time increases for smaller excitation energies. This effect prevails even through the density of states increases toward the band minimum resulting in a larger number of available scattering partners. Considering acoustic and optical phonons yields the fastest relaxation times since every phonon mode creates an effective relaxation channel. Like with only optical phonons we see a similar acceleration behavior towards the band edge which is slightly weaker than for optical phonons alone, cp. 44% versus 33%. Now the interplay of both phonon modes contribute: on one hand side we have smaller phonon momenta q towards the band edge, i.e. for lowering the excitation energy and on the other side the smaller getting electronic momenta k in the prefactors lead to shorter relaxation times.

4.2.5 Dependence on Diameter and Chirality

We extend at this stage our relaxation dynamic studies to variety of tubes considering:

- tubes with different diameters obeying nearly the same chiral angle ϑ
- scanning the range of chiral angles between $0^\circ < \vartheta < 30^\circ$ with nearly constant diameter d

The excitation energy E_{exc} is fixed to the second optical transition E_{22} where the fitting of the electronic occupation decay will be performed.

Diameter:

We chose tubes $(n_1, 1)$ with nearly constant chiral angle $\vartheta \approx 4.3^\circ - 2.1^\circ$ covering diameters from 0.9 to 1.8 nm. We simulate consistently the scattering with acoustic, optical, and both phonon modes together. In all three cases we see a slow-down trend in the relaxation times for tubes with larger diameters, which origins in the $\frac{1}{d}$ dependence of both electron-phonon couplings, cp. Eq. (3.58,3.60). For acoustic phonons the relaxation time increases from 1.2 to 7 ps by a factor of approximately six, cp. Fig. 4.14 (a). This results from the explicit dependence of the electron-phonon coupling element for the LA mode on the absolute value of the transferred phonon momentum. For larger tube diameters the subband curvature α_l increases. Since we pump and probe at the E_{22} transition we reach with increasing tube diameters further to the band edge of the lower subband ϵ_0^{C1} of the respective tube. The excitation closer to the band edge leads to smaller phononic momentum transfer and therefore the coupling is weaker, cp. Fig. 4.13. This yields directly to a slow down of the relaxation dynamics and finally larger relaxation times. In contrast, the relaxation times for scattering with optical phonons decrease for diameters larger than 1.5 nm in spite of the $1/d$ -dependence of its electron-phonon coupling element, cp. Eq. (3.58). This can be traced back to the variation of the excitation energy with the diameter. One has to keep in mind that we fixed the excitation E_{exc} to the transition energy E_{22} . Because for CNTs with large diameters E_{22} decreases. This results in faster relaxation times, cp. Fig. 4.13 (b). Thus, scattering becomes more efficient at lower excitation energies.

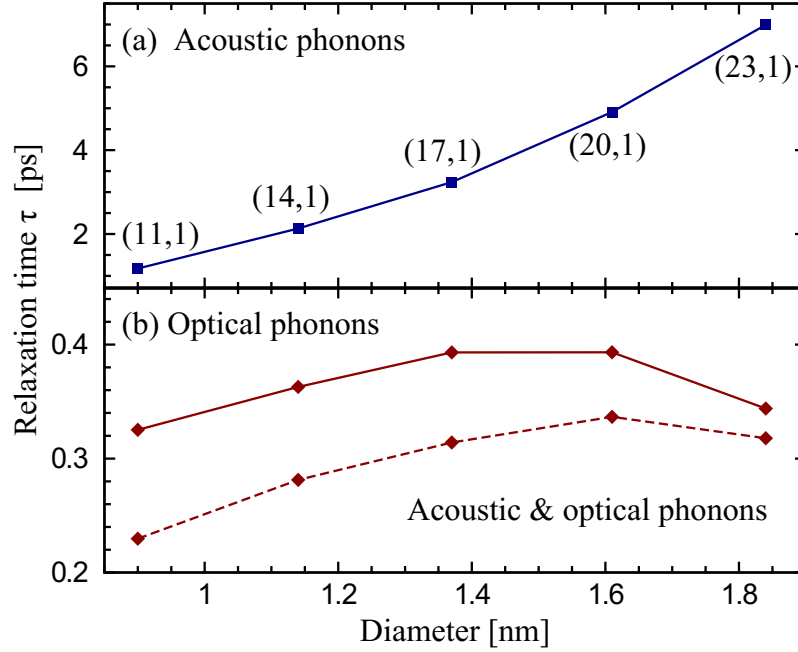


Figure 4.14: Relaxation time performance with respect to the diameter for constant excitation energy $E_{exc} = E_{22}$ of each single tube. The investigated tubes with $(n_1, 1)$ exhibit a slight change of the chiral angle $\vartheta \approx 4.3^\circ - 2.1^\circ$. Same phonon mode selection for (a) and (b) as used before, cp. Fig. 4.13, taken from [76].

Chirality:

Now we vary the chiral angle from zig-zag to armchair tubes by increasing the angle from $\vartheta = 0^\circ$ to $\vartheta = 30^\circ$ with a minor change in diameter. We chose CNTs along the exemplary Kataura branch $2n_1 + n_2 = 29$ including the so far discussed $(14, 1)$ tube, cp. Fig. 4.15. The relaxation times in dependence of the chiral angle do not show such a strong change, in particular because the subband curvature almost does not alter. The relaxation time $\tau_{C_1}^{IA}$ is nearly independent of the chiral angle for optical phonons, cp. Fig. 4.15 (b). This results from two counteracting mechanisms: The $1/d$ dependence of the optical coupling element slows down the relaxation time, whereas the reduced excitation energy for CNTs with increasing chiral angle gives rise to an acceleration of the dynamics. An increase by approximately 30% in the relaxation times can be seen for interaction with acoustic phonons, cp. Fig. 4.15 (a). This originates to some extent from the slight diameter change along the investigated Kataura branch and the high sensitivity of the electron-phonon coupling for acoustic phonons.

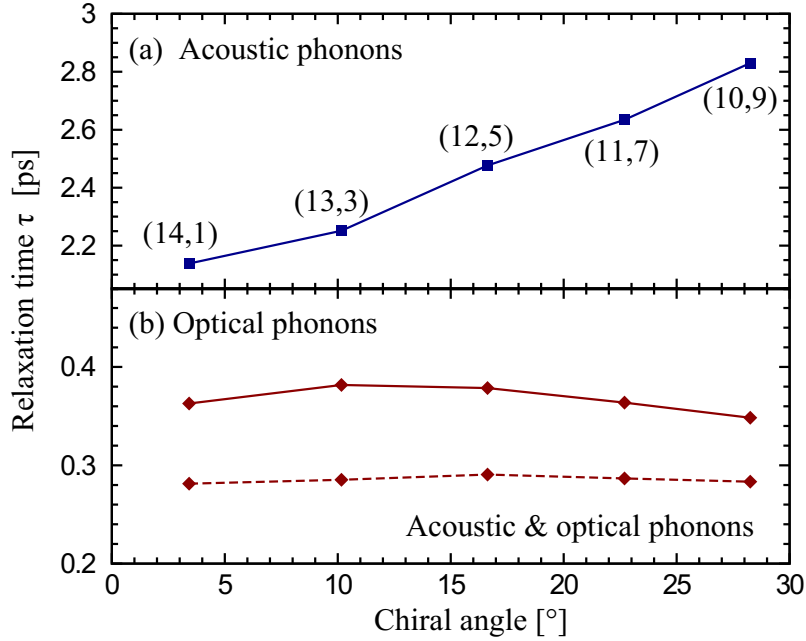


Figure 4.15: Relaxation time dependence under the variation of the chiral angle from $\vartheta = 0^\circ$ to $\vartheta = 30^\circ$ for tubes along the Kataura branch $2n_1 + n_2 = 29$. We mention, that a slight change in diameter from 1.14 to 1.29 nm exists, taken from [76].

4.3 Intra- and Intersubband Dynamics-Two Color Pump-Probe Studies

We now extend the model by taking the second higher lying conduction subband C_2 into account. This allows us to study new features like intersubband relaxation driven by electron-phonon scattering and its impact on the intraband dynamics of each subband. Further the influence of the intrasubband relaxation channels on the intersubband times will be investigated. A result of these studies will be, that intersubband scattering is only possible via optical phonons, since the energy of acoustic phonons is too small to overcome the energetic distance between the conduction subbands in semiconducting nanotubes. Also it will show up, that the subsequently C_1 intrasubband relaxation has no impact on the intersubband relaxation times. The investigations will follow the concept of the last section to show how the extended two-band includes the one-band model and which findings will change.

4.3.1 Relaxation Dynamics of the Semiconducting (23, 0) Zig-Zag Tube

We simulate the relaxation dynamics by exciting, i.e. pumping the exemplary (23, 0) zig-zag tube at $E_{exc} = E_{pump} = 1.8 \text{ eV}$ which is approximately 0.464 eV above the band edge of C_2 to study the

4.3. INTRA- AND INTERSUBBAND DYNAMICS-TWO COLOR PUMP-PROBE STUDIES

resulting relaxation dynamics through the interplay of the different electron-phonon interaction. We perform the following electron-phonon scattering scenarios:

- (a) optical intra- and intersubband
- (b) acoustic intra- and optical intersubband
- (c) acoustic and optical intra- and optical intersubband

,cp. Fig.4.16. For (a) we see, that the non-equilibrium electronic occupation raising at 0.9eV scatters within 1.2ps along C_2 in equidistant steps of the optical phonon energy $\epsilon_{q_0}^{\Gamma\text{TO}}$ towards the band edge $\epsilon_0^{C_2}$. During the first hundred femtoseconds the distribution raises in the lower subband C_1 , indicating the intersubband scattering with optical phonons. The following intraband relaxation towards $\epsilon_0^{C_1}$ into equilibrium is achieved on a timescale of 2.5 ps. In contrast for intraband scattering with acoustic phonons (b) the electron occupation relaxes energetically downwards continuously in the range from 0.9 – 0.8eV within C_2 while leading to a broadened intersubband scattered distribution around 0.708eV in C_1 . From there the electrons are quasi-continuously scattered reaching further to the band edge since the decreasing phonon momenta allow subsequently smaller

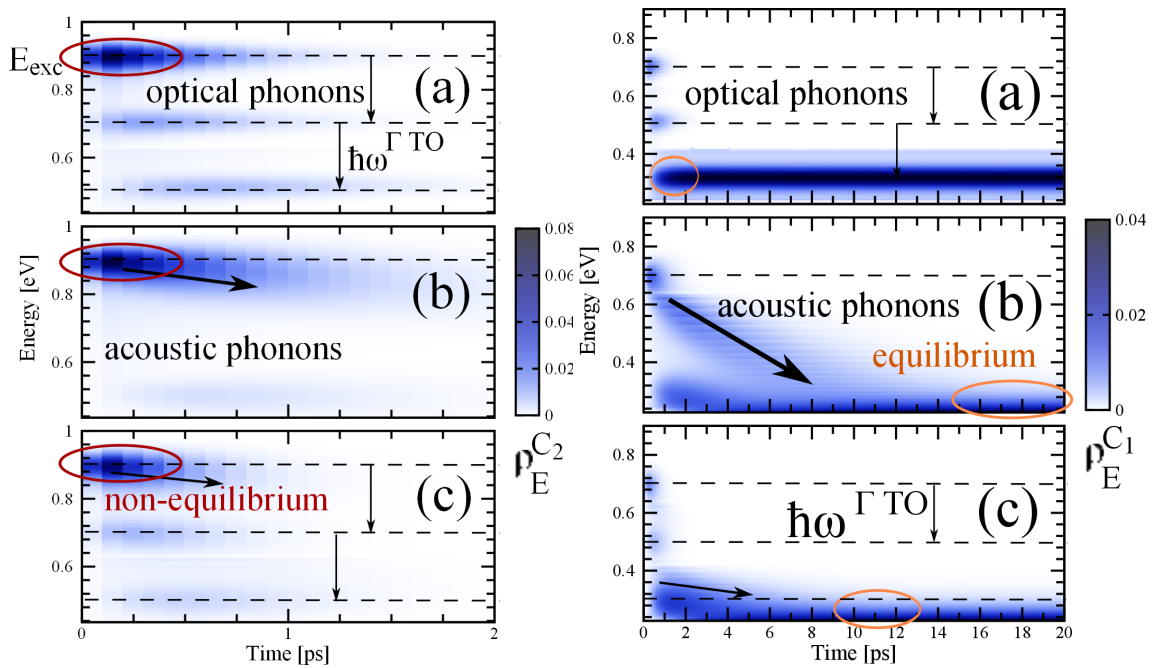


Figure 4.16: Phonon-induced relaxation dynamics of optically excited non-equilibrium carriers within the two lowest lying subbands C_2 (left side) and C_1 (right side). Three cases are considered: Intrasubband relaxation via optical (a), acoustic (b) and (c) optical together with acoustic phonon modes. The respective intersubband scattering for all cases is driven with optical phonons, since the acoustic phonon energy is too small to overcome the energetic separation between the subbands.

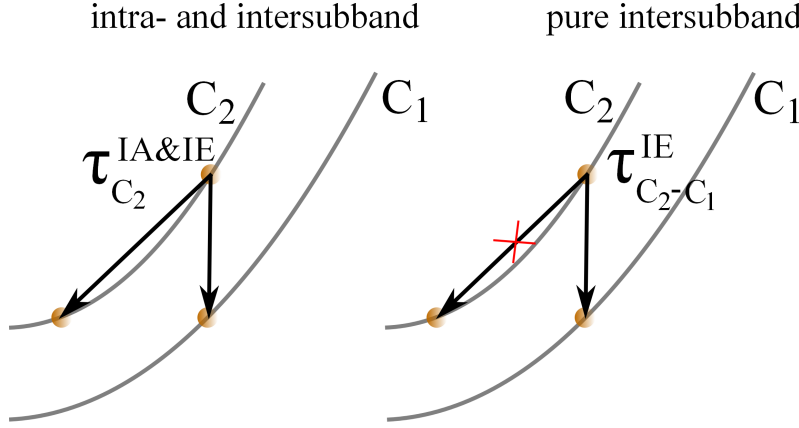


Figure 4.17: Sketch of the different relaxation channels for the simulated cases. The right side displays the pure intersubband relaxation $\tau_{C_2-C_1}^{\text{IE}}$ from the upper C_2 into the lower C_1 subband suppressing the intrasubband relaxation, while on the left the full relaxation containing intra- and intersubband relaxation $\tau_{C_2}^{\text{IA\&IE}}$ is shown.

energy steps in comparison to the large constant optical phonon energy. In combination of both phonon modes (c) we can see that optical phonons dominate intraband relaxation within the first hundred femtoseconds in C_2 and the first picosecond in C_1 . For the relaxation in the upper C_2 subband acoustic phonons do not account much. In contrast within the lower subband they play a major role for the redistribution into the equilibrium state resulting in a larger timescale from 1 ps up to 20 ps of the dynamics. We extract relaxation times via the same fitting routine used for the intraband case for the intra- and intersubband relaxation times. We perform the fit at E_{exc} in the upper and reduced by the optical phonon energy $\epsilon_{q_0}^{\text{ITO}}$ in the lower subband, i.e. the point in energy where the electron distribution raises after intersubband scattering. First we simulate the full relaxation with all intrasubband relaxation channels allowed, cp. the left side of Fig. 4.17 obtaining the relaxation times $\tau_{C_2}^{\text{IA\&IE}}$ and $\tau_{C_1}^{\text{IA}}$. To extract only the intersubband relaxation times $\tau_{C_2-C_1}^{\text{IE}}$ we suppress the intrasubband relaxation within C_2 . Therefore, the non-equilibrium distribution can just relax via intersubband scattering into C_1 , cp. right side Fig. 4.17. We summarize the relaxation times extracted for the different scattering scenarios in table 4.2:

Scattering partner	$\tau_{C_2}^{\text{IA\&IE}}$ [ps]	$\tau_{C_1}^{\text{IA}}$ [ps]	$\tau_{C_2-C_1}^{\text{IE}}$ [ps]
(a) optical	0.317	0.334	0.742
(b) acoustic	0.432	0.492	0.742
(c) acoustic & optical	0.228	0.267	0.741

Table 4.2: Relaxation times extracted for the semiconducting (23,0) zig-zag tube for the three scattering scenarios (a)-(c). The tube is pumped at 1.8 eV with pulse width of $t_{\text{pulse}} = 28$ fs and $A_0 = [0.13 \frac{\text{eV fs}}{\text{e}_0 \text{ nm}}]$. The fitting is performed for the upper C_2 at E_{exc} and for the lower C_1 subband at $E_{\text{exc}} - \epsilon_{q_0}^{\text{ITO}}$.

4.3.2 Excitation Energy

For the exemplary semiconducting (23,0) tube we study the influence of the excitation energy E_{exc} on the relaxation dynamics within the two band model. We vary E_{exc} from 1.4 to 2.1 eV under the consideration of the interplay from the different phonon modes according to our previous investigations. The extracted relaxation times for the upper C_2 and lower C_1 subband include now intra and intersubband relaxation dynamics, cp. Fig. 4.18. Within the upper subband C_2 the relaxation dynamics fastens up for all three cases (a)-(c) by lowering E_{exc} , cp. upper panel in Fig. 4.18. The strongest trend is obtained for scattering with optical phonons (b) by lowering the relaxation times about 51%. With acoustic phonons (a) the relaxation times change only slightly in

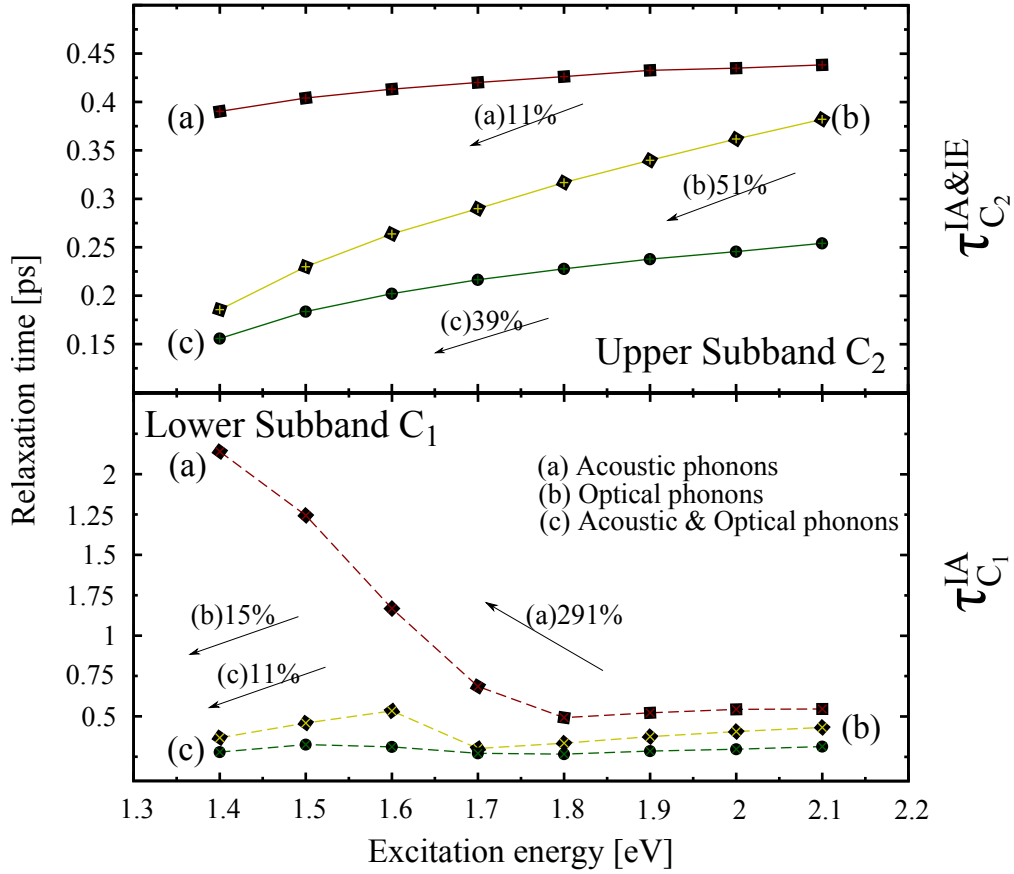


Figure 4.18: Dependence of the phonon-induced relaxation times $\tau_{C_2}^{IA\&IE}$ and $\tau_{C_1}^{IA}$ on the excitation energy for the exemplary (23,0) nanotube in the upper C_2 and the lower subband C_1 , respectively.

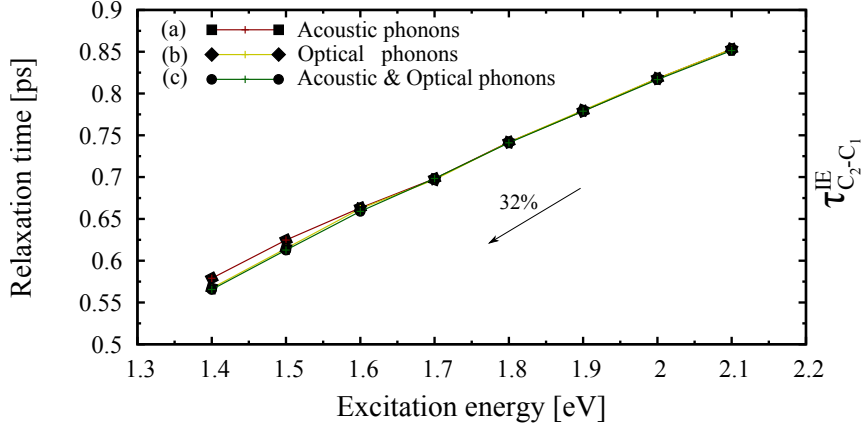


Figure 4.19: Intersubband relaxation times fitted at the excitation energy for scattering with (a) acoustic, (b) optical phonons and (c) both modes together.

the upper subband by 11 % and with both modes combined by 39 %. Interestingly the behavior for the lower subband C_1 shows a significant difference comparing the electronic relaxation dynamics from scattering with acoustic or optical phonons. This originates like in the one-band model in the dependence of the acoustic carrier-phonon element on the phonon momentum $|q|$. For smaller excitation energies the transferred phonon momentum is reduced which results in a slow down of the relaxation dynamics, cp. Fig. channel-sketch-acoustic. We have to note that in this investigation we choose a much more extended range of energy emphasizing a larger trend of the relaxation time behavior. With optical phonons we see a slight decrease of the relaxation times of 15 % when changing to smaller excitation energies. In opposite, for the interaction with acoustic phonons after a similar decrease in the range of 2.1 – 1.8 eV the relaxation times show a large slow down up to approximately 2.13 ps for decreasing the excitation energy to 1.4 eV, cp. (a) in the lower panel of Fig. 4.18. With optical phonons the decrease behavior of the relaxation times are reflected by the prefactors \mathfrak{X} and \mathfrak{Y} for intra- and intersubband scattering, cp. Eq. (2.44) and (2.46). Since both depend on the electronic momentum k and therefore on the energy of the band structure $\varepsilon_k^l = \alpha_l k^2 + \varepsilon_0^l$ it follows that for lower energies within the subband the prefactors are smaller and hence the scattering rates are larger and the relaxation times fasten up. For optical phonon scattering this prevails in both subbands. Below 1.7 eV the relaxation times in the lower subband slow shortly down but the global trend fastens up. This is a remnant of the Markov approximation occurring via fitting the temporal decay of the electronic distribution, which is most prominent for the large energy steps of optical phonons. The minor change of the relaxation times in the lower subband C_1 compared to the large one in the upper subband C_2 stems from the fact that the electrons cannot scatter further due to the energy conservation and constant optical phonon energies. In comparison non-equilibrium electrons generated closer the band edge in the upper subband have an extra intersubband relaxation channel and can scatter further into the lower subband C_1 . To

4.3. INTRA- AND INTERSUBBAND DYNAMICS-TWO COLOR PUMP-PROBE STUDIES

extract relaxation times for the intersubband scattering process with optical phonons we neglected the intrasubband relaxation channels of the upper subband C_2 , cp. Fig. 4.17. We fitted the temporal decay of the non-equilibrium electron distribution at the excitation energy. In the lower subband C_1 we again simulated scattering with acoustic and optical phonon modes solely and together. We obtain a linear slow down for an increasing excitation energy from approx 0.57 to 0.85 ps, cp. Fig. 4.19. A clear distinction between the relaxation scenarios (a)-(c) cannot be made. Therefore, we can conclude that the further relaxation processes in the lower subband have no influence on the intersubband relaxation times. In comparison to the case of intra- and intersubband relaxation, cp. Fig. 4.18 the relaxation times for the different scattering cases are clearly distinguishable within C_2 due to intrasubband relaxation channels. Also the relaxation is faster due to the doubled number of relaxation channels.

4.3.3 Diameter and Chirality Dependence

Diameter

We also extend our studies analog to the single-band model to a variety of tubes considering the two cases: change in diameter with constant chiral angle and tuning the chiral angle ϑ from 0° up to approximately 30° . Within the two band model, the behavior of the relaxation times for the interaction with the acoustic and optical phonon modes is investigated for intra- and intersubband relaxation. For both cases the excitation energy E_{exc} is fixed to 1.8 eV. The fit is performed for the upper subband C_2 at E_{exc} and the lower subband C_1 at the point where the electronic distribution raises after intersubband scattering, i.e. $E_{exc} - \epsilon_{q_0}^{ITO}$. Figure 4.20 displays the relaxation times $\tau_{C_2}^{IA\&IE}$ and $\tau_{C_1}^{IA}$ for varying the diameter from 1.57 to 2.51 nm covering zig-zag tubes with the constant chiral angle $\vartheta = 0^\circ$. With (a), (b) and (c) the intrasubband scattering via acoustic, optical

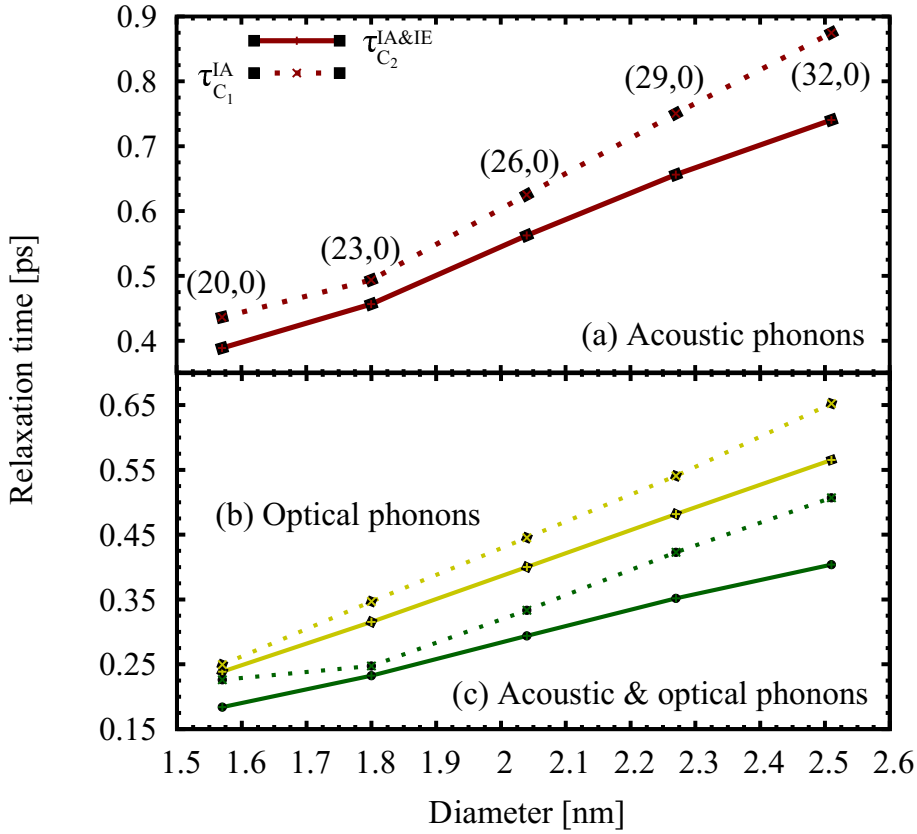


Figure 4.20: The relaxation times for the upper and lower subband $\tau_{C_2}^{IA\&IE}$ and $\tau_{C_1}^{IA}$ as a function of the nanotube diameter d for the cases of electron-phonon interaction (a)-(c). The excitation setup is kept consistent to the previous studies: $E_{exc} = 1.8$ eV, $t_{pulse} = 28$ fs and $A_0 = [0.13 \frac{eVfs}{e_0 nm}]$. Since we chose zig-zag tubes the chiral angle is constant, i.e. $\vartheta = 0^\circ$.

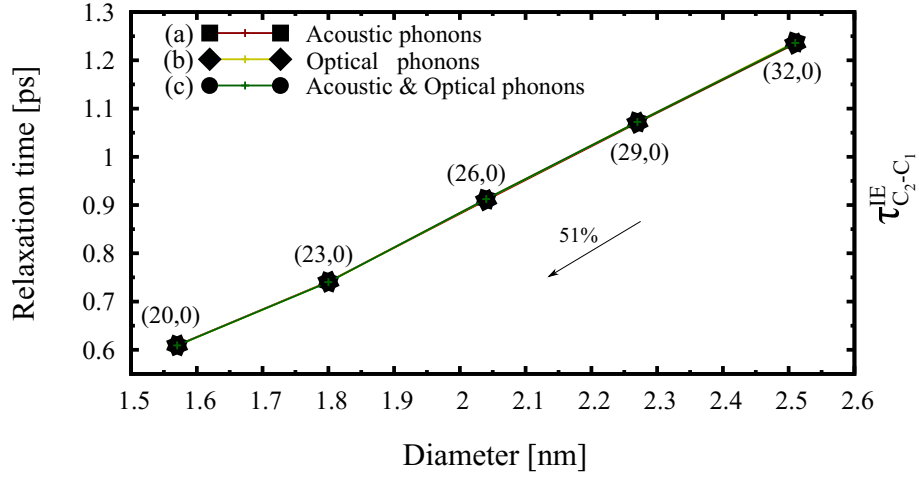


Figure 4.21: Intersubband relaxation times in dependence of the tube diameter fitted at the E_{exc} within C_2 according to Fig. 4.17.

and both phonon modes combined in both subbands is depicted. We plotted both relaxation times for C_2 and C_1 together in the same panel to emphasize their strong sensitivity on the tube diameter. As expected from the previous investigation, we find faster relaxation times in the upper subband C_2 . Reducing the diameter leads to an acceleration of the relaxation dynamics in both subbands for all three cases. The relaxation times decrease approximately 50% for acoustic, 55% for acoustic and optical and 60% for scattering with only optical phonons. These trends can be ascribed to the explicit dependence of the electron-phonon coupling elements $|g_{q_0}^\gamma|$ ($\gamma = \Gamma\text{TO}, \Gamma\text{LA}$) on the diameter. For optical phonons (b) below 1.6 nm, $\tau_{C_2}^{\text{IA}\&\text{IE}}$ and $\tau_{C_1}^{\text{IA}}$ become similar. This originates in the increase of the energetic difference between the two subbands with decreasing diameter mainly the intersubband gap $\Delta\varepsilon$, cp. Fig. 4.22. The energy gap clearly exceeds the optical phonon energy $\varepsilon_{q_0}^{\Gamma\text{TO}} = 192 \text{ meV}$ leading to inefficient intersubband scattering. Therefore, the dynamics in the two subbands is determined only by the intrasubband scattering and no difference between both relaxation times can be made, cp. Fig. 4.20 (b). The slowed-down relaxation dynamics for tubes with large chiral angles can be explained by the slight increase of the diameter, when varying the chiral angle from the zig-zag to the armchair configuration. The influence on the intersubband relaxation is with a fastening of 51% for lowering the tube diameter much stronger in comparison to the variation of the excitation energy of the single tube with constant diameter.

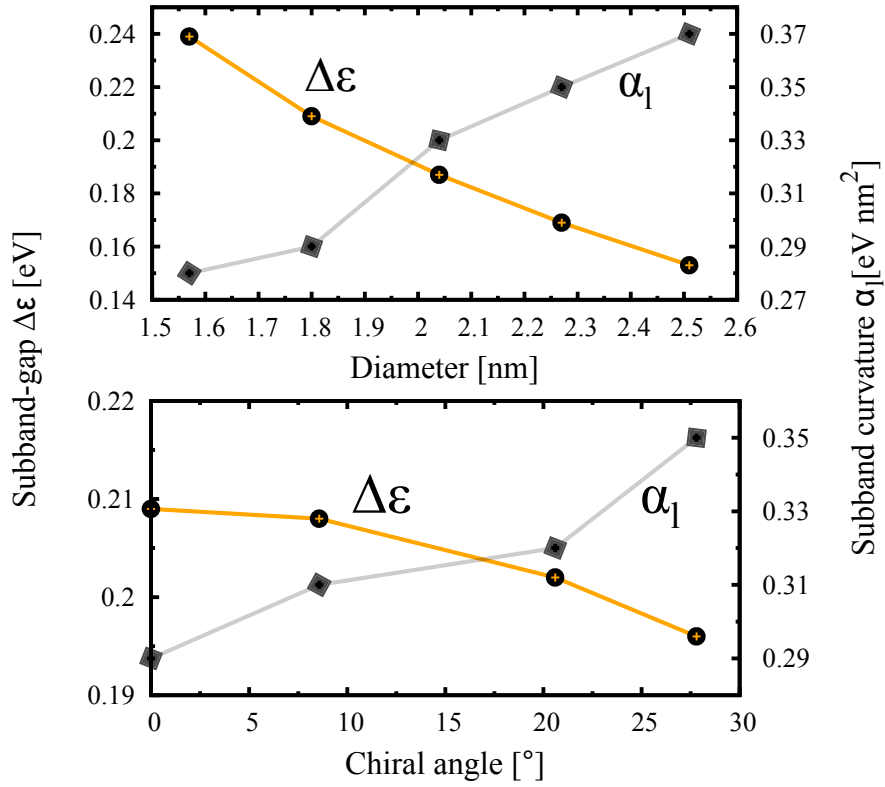


Figure 4.22: Dependence of the intersubband gap $\Delta\varepsilon = \varepsilon_0^{C_2} - \varepsilon_0^{C_1}$ and the subband curvature α_l , $l = C_2, C_1$ for the tubes investigated within the change of diameter and chiral angle ϑ .

Chirality

We complete our investigations of the intra- and intersubband relaxation dynamics on the (23,0) tube with the variation of the chiral angle. We chose tubes exhibiting only a small change in diameter of 0.24 nm to keep the influence of the strong diameter dependence shown in the previous section low. The subband gap $\Delta\epsilon$ between the band edges of C_2 and C_1 decreases therefore also slightly by approximately 13% with increasing chiral angle, cp. Fig. 4.22. The presented tubes cover the whole range of chiral angles from $\vartheta = 0^\circ$ for the (23,0) zig-zag to $\vartheta = 27,8^\circ$ for the armchair like (16,14) tube. The pump energy ($E_{pump} = E_{exc}$) is consistently set to 1.8 eV with a pulse width of $t_{pulse} = 28$ fs and an amplitude of $A_0 = 0.13 \left[\frac{eV \cdot fs}{e_0 nm} \right]$, following the setups of the diameter studies. For both subbands we see that with increasing chiral angle with only acoustic (a) or optical (b) and optical with acoustic modes combined (c) the relaxation times $\tau_{C_2}^{IA\&IE}$ and $\tau_{C_1}^{IA}$ slow slightly down about 19% for C_2 and 23% for C_1 , cp. Fig. 4.23. This results, like in the case

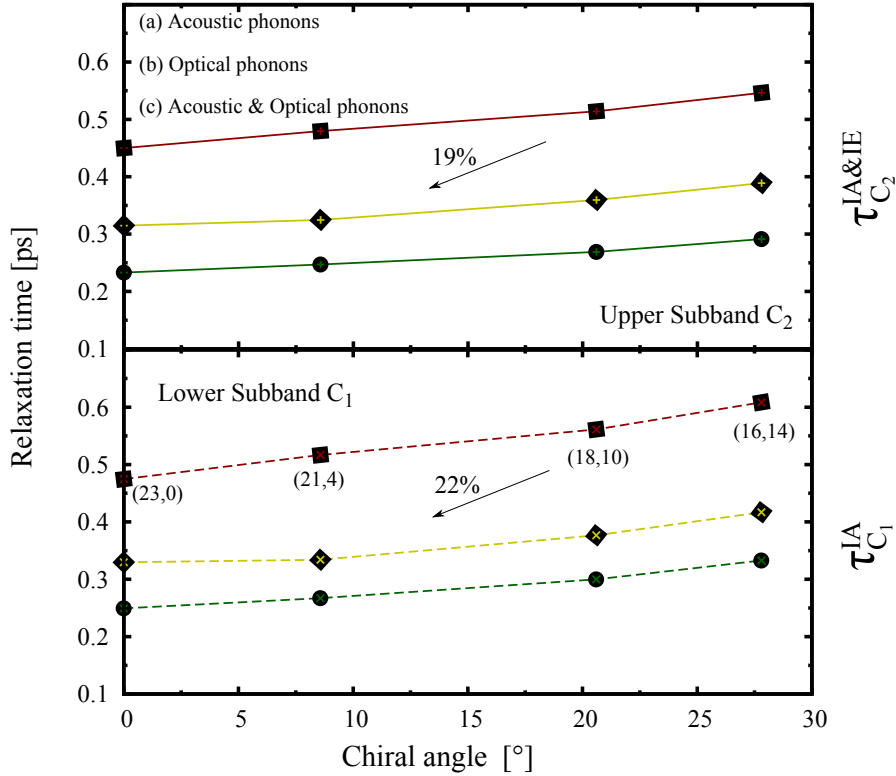


Figure 4.23: Influence of the chiral angle ϑ on the relaxation times in the upper and lower subband $\tau_{C_2}^{IA\&IE}$ and $\tau_{C_1}^{IA}$ comparing the different intraband relaxation channels with optical and acoustic phonons. The variation of ϑ from 0° to $27,8^\circ$ correspond to tubes along the Kataura branch $2n_1 + n_2 = 46$, while the tube diameter show just slight increase from 1.8 to 2 nm.

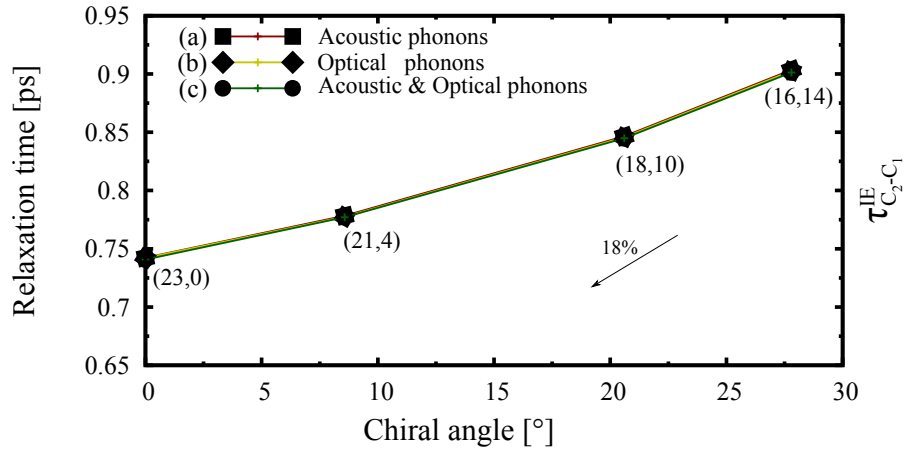


Figure 4.24: The intersubband relaxation time $\tau_{C_2-C_1}^{\text{IE}}$ behavior in dependence of the chiral angle ϑ . Again the subsequent C_1 intraband relaxation has no influence on the intersubband relaxation dynamics.

of only intraband relaxation in the single-band model, cp. section 4.2.5, from the slight change of the diameter from 1.8 to 2 nm. Also for the intersubband relaxation time $\tau_{C_2-C_1}^{\text{IE}}$ this prevails by a slow down from 0.74 to 0.9 ps by varying the chiral angle ϑ from the zig-zag to the armchair-like configuration.

4.4 An Experimental Motivated Two Color Pump-Probe Study

4.4.1 Modeling the Experiment

To test the presented theoretical model of inter- and intrasubband relaxation dynamics we will finally compare it to recent two-color pump-probe spectroscopy experiments done by O.Dyatlova et al. in the group of Prof. U. Woggon. The experiments have been performed with enriched chiralities samples of the semiconducting (7,5) and (7,6) carbon nanotubes which we will label sample (A) and (B), respectively. For the investigations of the relaxation process within a tube it is crucial to have samples with a high purity of a single nanotube chirality. In general a sample contains more than one tube species resulting from the growing mechanisms. This causes, that tubes are not spatially separated and tube-tube interactions leading to energy transfers cannot be excluded. The hereafter presented results of our mutual stimulated experimental and theoretical research can be found in our present paper [17]. As a first step, the experimental characterization of the samples is done within the earlier described photoluminescence excitation spectroscopy. A pulsed titanium sapphire laser was used for exciting the samples to obtain the PLE maps shown in Fig. 4.25. From this 14 different excitation energies between 1.82 – 2.04 eV have been selected and the emission in the range from 1.05 to 1.35 eV have been recorded. The obtained PLE maps for the (A) and (B) samples are displayed as contour plots of the photoluminescence intensity over the excitation and emission energy ranges. Via the intensity peaks sample (A) exhibit clearly (7,5) tubes while for sample (B) beside the desired (7,6), also (7,5) and (8,3) tubes show up. In comparison with reference [14] the transition energies E_{22} and E_{11} have been determined for the (7,5) tubes in sample (A) and the (7,6) tubes in sample (B). These values have been further used as the pump and probe energies in the following studies. To estimate the chiral purity of the (7,5) and (7,6) species in the (A) and (B) samples, respectively absorption measurements have

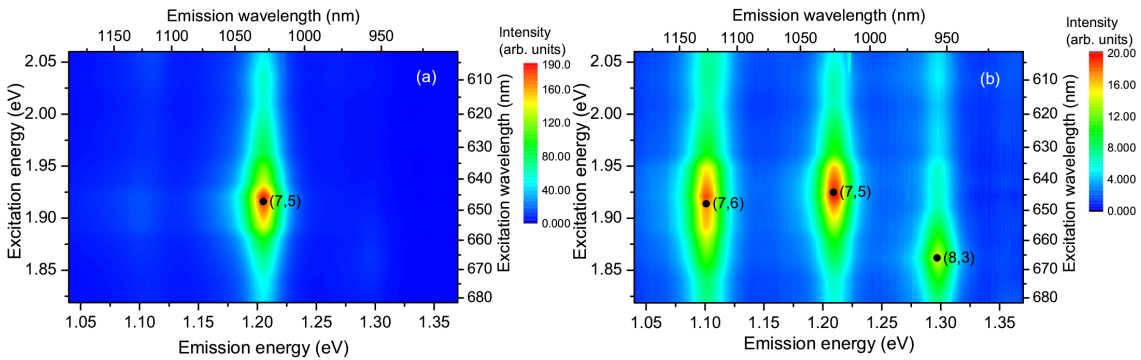


Figure 4.25: The recorded photoluminescence excitation spectra from sample (A) being enriched with (7,5) and sample (B) with (7,6) tubes. The photoluminescence intensity over the emission for the respective excitation energies are displayed, taken from [17].

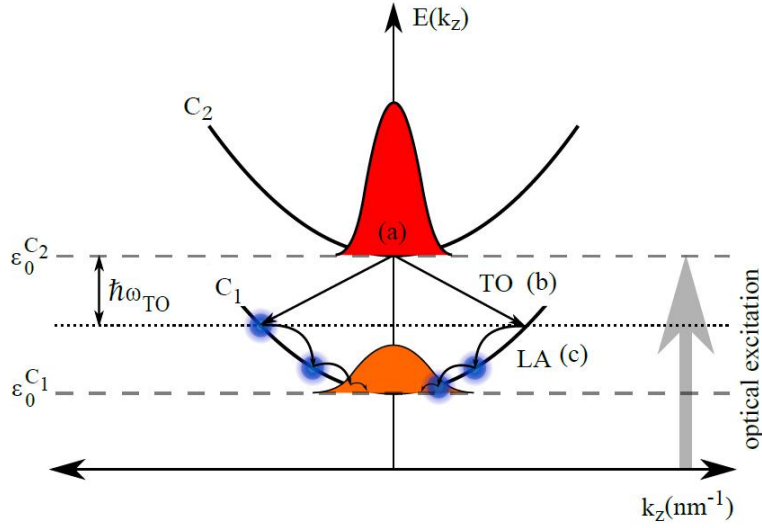


Figure 4.26: Sketch of the possible electron relaxation channels of the (7,5) tube with constant optical phonon and smaller getting acoustic phonon scattering steps. The redistribution process from at $E_{22}/2$ generated non-equilibrium (red Gaussian) into equilibrium displayed by the Fermi-distribution around ϵ_0^{C1} (orange), taken from [17].

been performed. The chiral purity of the (7,5) and (7,6) tubes has been estimated via absorption measurements of the respective (A) and (B) samples. The absorption profiles have been fitted with Lorentzian curves and the resulting enclosed area has been integrated. The chiral purity of the (7,5) and (7,6) species for the (A) and (B) sample have been estimated to be 49% and 24%, respectively. The observation of the relaxation dynamics is performed via energy-selective two-color pump-probe experiments. We described the setup in principal in section 4.1.2 and refer the reader for more details to our paper [17]. With the possibility to tune the wavelengths of the synchronized pump and probe laser systems, the behavior of the relaxation dynamics between the lowest lying C_2 and C_1 subbands have been investigated. For our theoretical simulation we applied the experimental setup considering the special case of resonant pumping at $E_{22}^{(7,5)}$. this leads directly to the relaxation of the non-equilibrium electronic distribution into C_1 via intersubband scattering with optical phonons with subsequent optical and acoustic intraband relaxation. In Fig. 4.26 the relaxation channels and the relaxation behavior constraint to this setup are sketched. First, electrons are pumped by the external laser field through the resonant transition $E_{22}^{(7,5)}$ into the C_2 subband (a) from where they scatter directly into the lower conduction subband C_1 via optical (TO) phonons (b) and finally relax through interaction with acoustic (LA) phonons into an equilibrium towards the band edge ϵ_0^{C1} . We evaluated the equations of motion, cp. Eq. (2.19) numerically for the carrier occupations $\rho_{\epsilon}^{C_2, C_1}(t)$ close to the experimental setup pumping optically resonant to the earlier determined $E_{22}^{(7,5)}$ transition with a pulse width of $t_{pulse} = 190$ fs in FWHM.

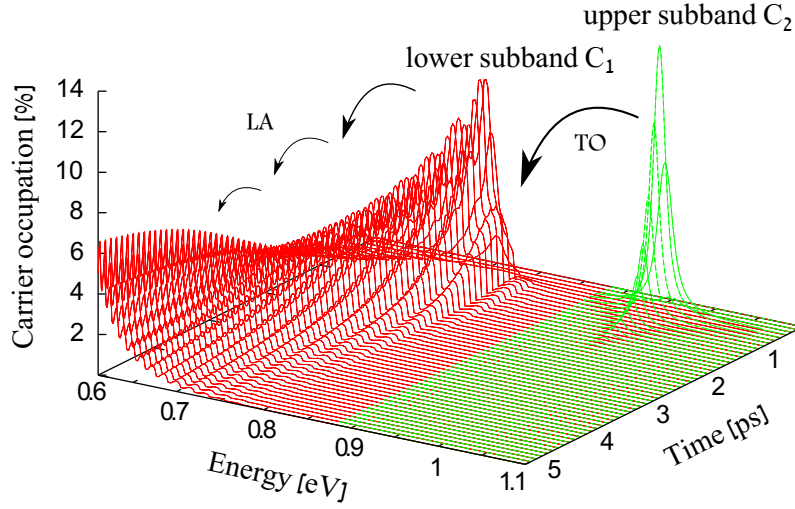


Figure 4.27: Time and momentum resolved inter- and intrasubband relaxation dynamics of the (7,5) tube. Pumped resonantly at E_{22} with a pulse width of $t_{pulse} = 190$ fs and an amplitude $A_0 = 0.05 \left[\frac{eVfs}{e_{0nm}} \right]$. Carriers are injected at the band edge $\epsilon_0^{C_2} = E_{22}/2$ scattering further under emission of Γ TO phonons within a few hundred femtoseconds into C_1 . From there they are finally redistributed via acoustic phonons into a Fermi-like equilibrium on a picosecond timescale, taken from [17].

Thus, a non-equilibrium distribution of electrons is generated at the band edge $\epsilon_0^{C_2}$ and we trace the dynamics of the electronic occupations along C_2 and C_1 . The phonons are treated within a bath approximation as a Bose-Einstein distribution (cp. Appendix) at room temperature, i.e. $T = 300$ K. The phonon-induced dephasing of the microscopic polarization, cp. Eq. (2.39) is approximated via an average dephasing rate $\hbar\gamma = 12.5$ meV. The calculated carrier occupations are depicted in Fig. 4.27 as a function of energy and time for the experimentally investigated (7,5) tube. The generated non-equilibrium distribution at the band edge $\epsilon_0^{C_2}$, i.e. $E_{22}/2 = 1.05$ eV relaxes during the first hundred femtoseconds through intersubband-scattering via Γ TO phonons into the lower subband C_1 decreased by the optical phonon energy $\epsilon_{q_0}^{\Gamma TO}$. The occupation peak evolves at 0.77 eV after 1 ps. This directly reflects the experimental rise time. From this point, intraband scattering within C_1 via Γ TO and simultaneously Γ LA phonons towards the band edge $\epsilon_0^{C_1}$ takes place. The dominant process is the emission of optical phonons. Intraband scattering within the lowest subband C_1 via Γ LA phonons leads to a Fermi distribution on a picosecond timescale, cp. the thermal occupation after 5 ps in Fig. 4.27.

4.4.2 Detuning of the Probe Energy

With the described experimental pump-probe setup it is possible to change the wavelength of the probe beam, i.e. tuning the probe energy between E_{22} and E_{11} . In the experiment two groups of curves have been recorded for the (7,5) tube. Two probe measurements have been performed close

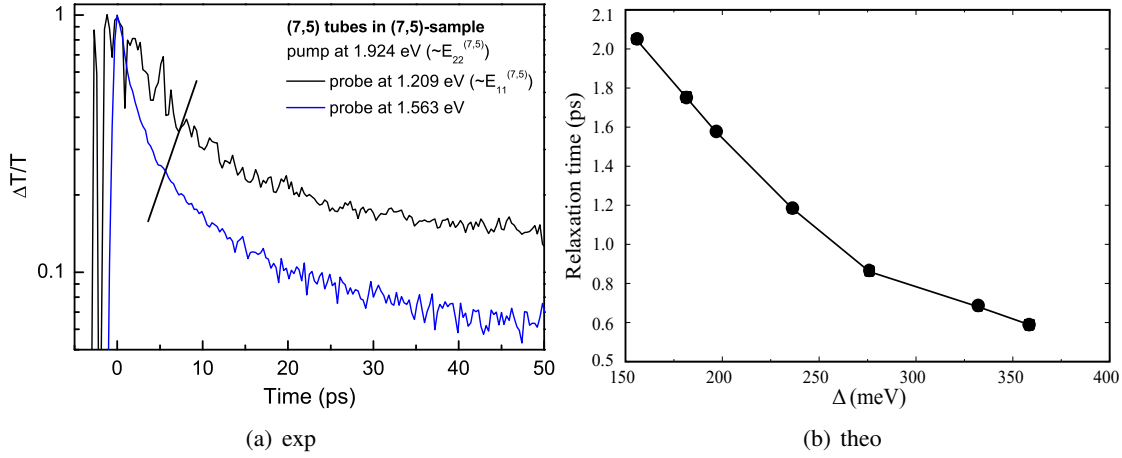


Figure 4.28: Left side: Differential transmission spectrum for sample (A) with the prominent (7,5) tube. The pump energy is set to the second optical transition $E_{22}^{(7,5)}$ to 1.924 eV. The probe pulse is located near to the first optical transition $E_{11}^{(7,5)}$ at 1.209 eV and 1.563 eV, which is 179 meV above the band edge $\epsilon_0^{C_1}$. Right Side: Relaxation time dependence of the probe energy for a pump energy set constant to 1.92 eV corresponding to $E_{22}^{(7,5)}$ displaying an acceleration of the relaxation dynamics towards higher probe energies, adapted from [17].

to $E_{11}^{(7,5)}$: $E_{\text{probe-I}} = 1.21$ eV, $E_{\text{probe-II}} = 1.25$ eV. Furthermore two curves have been recorded by probing approximately 300 meV higher in energy at $E_{\text{probe-III}} = 1.48$ eV and $E_{\text{probe-IV}} = 1.56$ eV. In every measurement the tube has been pumped resonantly to the energy of its second transition energy at $E_{\text{pump}} = 1.924$ eV $\approx E_{22}$. We compare the differential transmission curve obtained by probing at $E_{\text{probe-IV}}$ with the temporal evolution of the electron occupation $\rho_k^{C_2}$ at the corresponding energy in the lower subband. For the theoretical calculations we refer to the conduction bands and therefore to their band edges $\epsilon_0^{C_2}$ and $\epsilon_0^{C_1}$. These are the half of the value of the transition energies E_{22} and E_{11} under the assumption that the valence and conduction bands are symmetric, cp. Sec. 3.1.3. The recorded differential transmission spectra of the (7,5) sample for the highest and the lowest probe energy are displayed in half logarithmic representation, cp. left side of Fig. 4.28. A clear difference to faster relaxation dynamics, i.e. an acceleration of the relaxation dynamics towards higher probe energies is observed. In the theoretical simulation the probe energy can be obtained through fitting the temporal decay of the electronic occupation $\rho_k^{C_s}$ yielding relaxation times between two distinct k values. This implies how the distribution decays from one fixed energy point to the next possible via momentum conserving scattering with the respective phonon modes. Through the variation to larger probe energies, i.e. higher positions of energy in the subband, cp. Fig. 4.26 the transfer of the phonon momentum for a possible scattering process is enhanced. Due to the linear dependence of q occurring in the acoustic electron-phonon matrix element this leads to stronger electron-phonon coupling and therefore the decay of the carrier distribution is fastened up. Since the temporal evolution of ρ_k is connected to the inverse of the relaxation time τ^{-1} , the

4.4. AN EXPERIMENTAL MOTIVATED TWO COLOR PUMP-PROBE STUDY

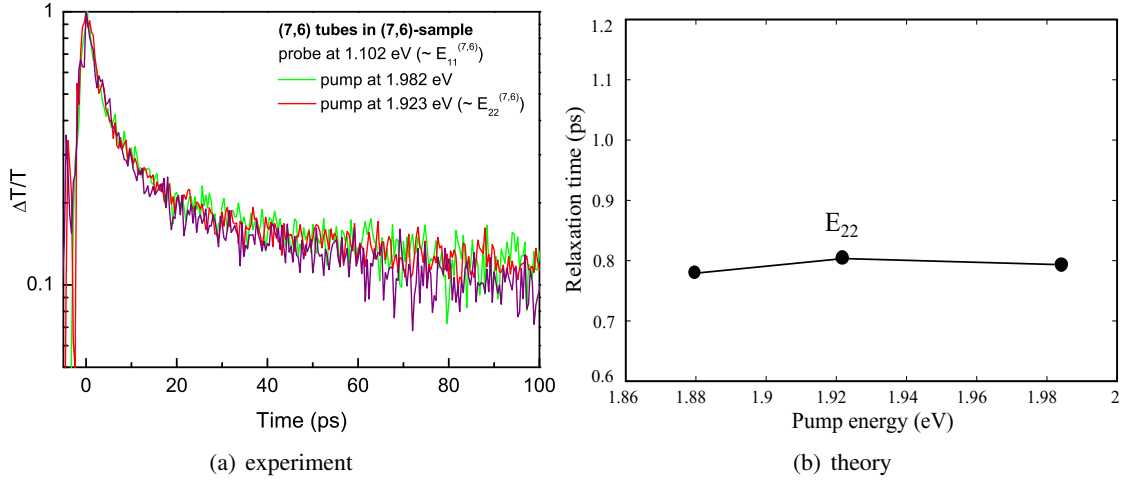


Figure 4.29: Left Side: Differential transmission spectrum measured for sample (B) with the prominent (7, 6) tube. The probe energy is set to $E_{11}^{(7,6)} \approx 1.102$ eV. The pump pulse is tuned around $E_{22}^{(7,6)} \approx 1.923$ eV = E_{VII} to $E_{\text{V}} = 1.982$ eV and $E_{\text{VI}} = 1.880$ eV. Right side: Dependence of the relaxation times for different pump energies at the fixed probe energy 1.3 eV of the (7, 6) tube. The relaxation times are hardly affected under this change, adapted from [17].

latter one decreases to shorter times with increasing phonon momentum transfer, i.e. stronger electron-phonon coupling, which the theoretical curve on the right side of Fig. 4.28 explains.

4.4.3 Detuning of the Pump Energy

For two-color pump-probe spectroscopy it is of interest to exclude influences of the pump energy for the following relaxation dynamics. Therefore, the probe beam was set to a constant energy according to the lowest optical transition energy of the (7, 6) tube. This energy was previously determined via PLE to $E_{11}^{(7,6)} \approx 1.102$ eV. Now the pump beam was tuned to higher and lower excitation energies $E_{\text{V}} = 1.982$ eV and $E_{\text{VI}} = 1.880$ eV around the second allowed optical transition $E_{\text{VII}} = 1.923$ eV $\approx E_{22}^{(7,6)}$. Within this large detuning range of ± 50 meV the observed DTS spectra, shown on the left side in Fig. 4.29 do not differ evidently and no change for the relaxation times can be concluded. Our corresponding calculations support this observation revealing no significant variations for the fastest decay component in the picosecond range, cp. right side Fig. 4.29. This underlines, that the point of energy where the non-equilibrium electrons enter does not effect on the further decay strength of the carrier distribution. Referring to the equations of motion for polarization and carrier occupation (2.17 and 2.18), it is clear that the pump energy $E_{\text{pump}} = E_{\text{exc}}$ enters via the external vector potential $A(t)$ modeling the excitation pulse with the Rabi frequency $\Omega_k^{C_s V_s}$ at a fixed point, cp. Eq. (4.2). Therefore, the pump energy has just an influence on the optical coupling. The further electron-phonon Boltzmann scattering terms are unaffected from the energetic position of the external coupling. Hence, the change of the starting position of the

non-equilibrium carrier distribution has no impact on the following redistribution process and the relaxation times do not alter, which is in agreement with the experimental observations.

4.5 At a Glance

We investigated the non-radiative relaxation dynamics driven by electron-phonon scattering for semiconducting nanotubes within PLE and pump-probe experiments:

- for the interplay between acoustic and optical phonons we state: intraband relaxation is driven initially within the first hundred femtoseconds via optical and on a picosecond timescale via acoustic phonons towards the band edge
- the fastest relaxation times are obtained for both phonon modes taken into account, since every phonon-induced relaxation channel enhances the scattering efficiency
- simulations with a two-band model being close to two-color pump-probe to experiments unveil:
intersubband scattering between the lowest lying subbands is shown to be driven only via optical phonons
- large tube diameters lead to a slow down of the relaxation times through weaker electron-phonon coupling $|g^{\Gamma\text{TO}/\Gamma\text{LA}}|^2 \approx \frac{1}{d}$
- intersubband relaxation times $\tau_{C_2-C_1}^{\text{IE}}$ are unaffected by the phonon species of the subsequent intrasubband relaxation within C_1
- the chiral angle of the tube has a low impact on the relaxation times
- compared to optical, acoustic phonons reveal a more pronounced relaxation time dependence on diameter and chirality
- tuning the probe while the pump energy is held constant reveals:
probing toward the band edge the relaxation time slows remarkably down due to the inverse proportional dependence of the relaxation times to the acoustic phonon momentum
- tuning the pump energy with probing at the same energy yields:
the relaxation times stay unaffected since the change of the starting position of the non-equilibrium carrier distribution has no effect on the following temporal redistribution

4.5. AT A GLANCE

phonon modes	$\tau_{C_1}^{IA}$ [ps]	$\tau_{C_2}^{IA\&IE}$ [ps]	$\tau_{C_2-C_1}^{IE}$ [ps]
Acoustic	0.5-2.2	0.43-0.38	0.85-0.57
Optical	0.4-0.3	0.38-0.18	–”–
Optical & Acoustic	0.26-0.25	0.25-0.15	–”–

Table 4.3: The obtained relaxation times from our two-band model simulation varying the excitation energy E_{exc} for the semiconducting (23,0) tube. We have a clearly faster relaxation within the upper C_2 in contrast to the lower C_1 subband due to additionally intersubband scattering channels. The largest relaxation times are obtained for low E_{exc} with acoustic phonons towards E_{11} .

phonon modes	$\tau_{C_1}^{IA}$ [ps]	$\tau_{C_2}^{IA\&IE}$ [ps]	$\tau_{C_2-C_1}^{IE}$ [ps]
Acoustic	0.43-0.88	0.38-0.73	0.6-1.24
Optical	0.25-0.65	0.23-0.57	–”–
Optical & Acoustic	0.23-0.5	0.18-0.4	–”–

Table 4.4: Relaxation times for the variation of the tube diameter. The main impact of the d^{-1} diameter influence through the optical phonon matrix element can be explicitly seen in the times for the intersubband scattering.

phonon modes	$\tau_{C_1}^{IA}$ [ps]	$\tau_{C_2}^{IA\&IE}$ [ps]	$\tau_{C_2-C_1}^{IE}$ [ps]
Acoustic	0.47-0.6	0.45-0.55	0.75-0.9
Optical	0.34-0.42	0.31-0.39	–”–
Optical & Acoustic	0.25-0.34	0.24-0.29	–”–

Table 4.5: Relaxation times for the variation of the chiral angle. Beside the small change in diameter the relaxation times are nearly unaffected.

5

Field Enhancement Calculations of Plasmonic and Non-Plasmonic Electrodes

The field enhancement calculations describing high electric field intensities created by localized surface plasmons and high curvatures at surfaces is based on the classical theory of electromagnetism. The physics is contained in the dielectric response function $\epsilon(\omega)$ of the material and its geometrical surface properties. The calculated field enhancement distributions to explain the observed effects in surface enhanced resonance Raman (SE(R)R) spectroscopy experiments can be viewed as localized surface plasmons (LSP) since the spatial extension of the area of interest is below the excitation wavelength. The LSPs are considered as an external driven oscillating dipole and thus emitting electromagnetic radiation. With this ansatz we describe the induced surface field enhancement in a coral platinum (Pt) island film [78] via the excitation of LSPs. We modeled a realistic electrode close to the experimentally yielded SEM pictures. Introducing hole-like defects in the platinum coating leads to an increase of the number of the incoming photons onto the lower lying silver (Ag) support. Furthermore, through the defects sharp edges occur within the Pt film creating high field intensities via such geometrical anisotropies. The latter possibility of enhancement origins in the surface morphology of the hybrid electrode. Another recent experiment done in the group of Prof. P. Hildebrandt and Prof. I. M. Weidinger demonstrates the enhancement behavior in a potential dependent SE(R)R study at a nanostructured TiO₂ electrode, a non-plasmonic material, by increasing the surface morphology. We also supported these findings with our calculations [79].

5.1 Enhancement of the Electric Field

The Raman scattering signal measured around the surface of a solid state can be enhanced through resonant coupling to a localized surface plasmonic mode of a nanostructured noble metal. This can be, for example, a sphere, a rod, or an underlying substrate formed as a bulk structure. The theory we apply here is based on classical electrodynamics solving time-harmonic Maxwell equations for a stationary case under boundary conditions between different media. Input parameters are the dielectric function, i.e. the permittivity $\varepsilon = \varepsilon(\omega)$, geometrical aspects of the surface structure and properties of the excitation source (e. g. a laser) like wavelength and polarization of the emitted radiation. We theoretically unveil underlying enhancement mechanisms leading to high electric field intensities explaining the observed increased Raman signals for probe molecules like the heme protein cytochrome c (Cyt-c) or cytochrome b_5 .

5.1.1 Time-Harmonic Maxwell Equations

The electric field \mathbf{E} is calculated from scattering theory for particles being smaller than the wavelength of the external excitation. Classical electromagnetism can be fully described through a coupled system of linear partial differential equations for the four field vectors. These Maxwell field equations are given for an inertia system within resting media written in the SI-system [80]:

$$\nabla \times \mathbf{H} = \partial_t \mathbf{D} + \mathbf{j}, \quad (5.1)$$

$$\nabla \times \mathbf{E} = -\partial_t \mathbf{B}, \quad (5.2)$$

$$\nabla \cdot \mathbf{D} = \rho, \quad (5.3)$$

$$\nabla \cdot \mathbf{B} = 0, \quad (5.4)$$

with \mathbf{E} and \mathbf{B} being the electric and magnetic field strength, \mathbf{D} and \mathbf{H} the electric and magnetic excitation, conventionally called dielectric displacement and magnetic field strength. The first equation (5.1) explains that electric currents including the displacement current are leading to a magnetic excitation while (5.2) describes that the temporal change of the magnetic field strength is creating an electric field. Via these two equations the magnetic and electric field are connected. Equation (5.3) reveals that the source of the electric excitation is the electric charge while Eq. (5.4) states the magnetic field strength is source free, i.e. magnetic monopoles do not exist.

The fields within the solid are described by the material equations:

$$\mathbf{D} = \varepsilon_0 \varepsilon(\mathbf{r}, t) \mathbf{E} = \varepsilon_0 \mathbf{E} + \mathbf{P}, \quad (5.5)$$

$$\mathbf{B} = \mu_0 \mu(\mathbf{r}, t) \mathbf{H} = \mu_0 (\mathbf{H} + \mathbf{M}), \quad (5.6)$$

where \mathbf{P} and \mathbf{M} stand for the macroscopic polarization and magnetization, respectively. The occurring constants are the permittivity $\varepsilon_0 = \frac{1}{c_0^2 \mu_0} \approx 8.854\,188 \times 10^{-12} \frac{\text{As}}{\text{Vm}}$ and the permeability in

vacuum $\mu_0 = 1.256637 \times 10^{-6} \frac{\text{Vs}}{\text{Am}}$. Here, we focus on the enhancements of the electric field \mathbf{E} . Furthermore, we constrain to the stationary behavior of \mathbf{E} , which is applicable through experiment in which the nanostructures are excited by a laser with a fixed wavelength. Therefore, the transient part vanishes on very short timescales. Under these considerations a time-harmonic ansatz can be applied:

$$\mathbf{E}(\mathbf{r}, t) = \mathbf{E}'(\mathbf{r})e^{-i\omega t}, \quad (5.7)$$

leading to an electric field equation separated in time and space:

$$\nabla \times \left[\frac{1}{\mu} [\nabla \times \mathbf{E}'] \right] - \omega^2 \epsilon \mathbf{E}^2 = 0, \quad (5.8)$$

where the curl curl $\nabla \times (\nabla \times)$ operator acts only on the space dependent electric field $\mathbf{E}'(\mathbf{r})$. The material is characterized by its dielectric function $\epsilon(\mathbf{r}, t)$ entering via the complex representation in the frequency domain

$$\epsilon(\mathbf{r}, \omega) = \epsilon_1(\mathbf{r}, \omega) + i\epsilon_2(\mathbf{r}, \omega) = (n + i\kappa)^2, \quad (5.9)$$

with the first part representing intra- and the second interband transitions. From the right hand side it can be seen that $\epsilon(\mathbf{r}, \omega)$ is composed of the refractive index n and the extinction κ representing the real and the imaginary part, respectively. Both wavelength dependent material parameters are taken from tables of the book of Palik [81] for further calculations.

5.1.2 An Electronic Gas in Motion: Collective Behavior of Electronic Density Fluctuations

The idea of introducing the plasmon can be traced back to the work of Bohm and Pines in 1952 when they first defined quantized plasma oscillations in bulk material as a collective excitation of the electron density [82]:

”The valence electron collective oscillations resemble closely the electronic plasma oscillations observed in gaseous discharges. We introduce the term ‘plasmon’ to describe the quantum of elementary excitation associated with this high-frequency collective motion.”

The displacement of the electron gas through an external electric field with respect to the heavy ions which are assumed to be static is preliminary picture in the frame of classical electrodynamics [30], cp. Fig. 5.1. Once the electron gas or plasma is excited in the direction of the applied field the Coulomb interaction between it and the positive background generated by the ionic cores leads to a restoring force and the plasma starts to oscillate. To describe this classically, the Drude-Lorentz model will be sketched briefly following the standard derivations [83] combining the Drude model [84] describing the conductivity of free electrons with the characterization of dipole oscillators within the Lorentz model. The idea starts with Newtons second law [85]:

”Mutationem motus proportionalem esse vi motrici impressae, et fieri secundum lineam rectam qua vis illa imprimitur”,

stating that the change of motion for a body is proportional to the force acting onto it. Or in the more generally valid form that the temporal change of the momentum of a body is caused by a

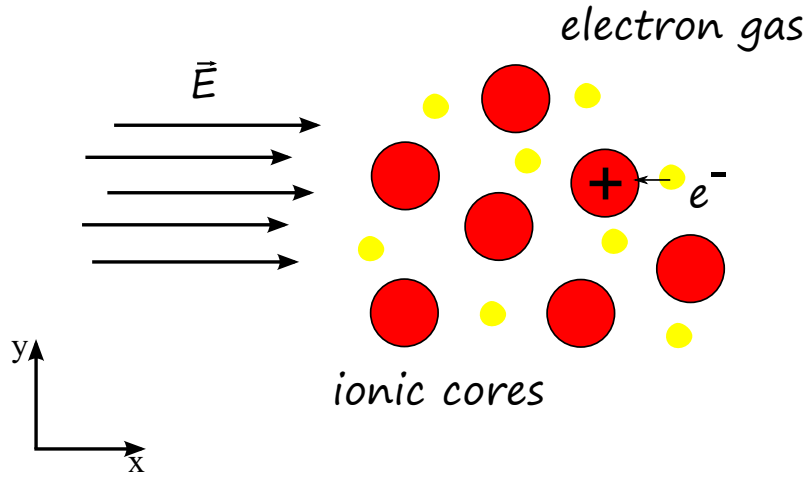


Figure 5.1: Sketch within the classical picture of the oscillating electron gas with respect to the heavy ionic cores.

force. Referring to Fig. 5.1 this force accelerates negative charged point masses, the electrons in x-direction:

$$m_e d_t^2 \mathbf{x} + m_e \gamma d_t \mathbf{x} + m_e \omega_0^2 \mathbf{x} = -e_0 \mathbf{E}(t) = -e_0 \mathbf{E}_0 e^{-i\omega t}, \quad (5.10)$$

with an acceleration term for the electrons and a damping term resulting from the restoring force of the ionic cores. The driving term arises from the electric field strength which is further rewritten as an amplitude \mathbf{E}_0 and an exponential function $e^{-i\omega t}$ with ω being the angular frequency of the exciting light field. Substituting with $\mathbf{x} = \mathbf{x}_0 e^{-i\omega t}$ we have an equation for \mathbf{x}

$$\mathbf{x}(t) = \frac{e_0}{m_e} \frac{1}{(\omega_0^2 + \omega^2 + i\gamma\omega)} \mathbf{E}(t), \quad (5.11)$$

which can be rewritten via the definition for the polarization of a gas

$$\mathbf{P} = -ne_0 \mathbf{x}, \quad (5.12)$$

with n being the density of electrons. Inserting the polarization, cp. Eq. (5.7) we have

$$\mathbf{D} = \epsilon_0 \mathbf{E} \left(1 - \frac{e_0^2 n}{m_e \epsilon_0} \frac{1}{\omega^2 + i\gamma\omega} \right), \quad (5.13)$$

from which we can conclude the expression for the dielectric function

$$\boxed{\epsilon(\omega) = 1 - \frac{\omega_{pl}^2}{\omega^2 + i\gamma\omega}}, \quad (5.14)$$

introducing the plasma frequency of a free electron gas

$$\omega_{pl} = \sqrt{\frac{e_0^2 n}{m_e \epsilon_0}}, \quad (5.15)$$

being a square root function of the density n of the electrons.

5.1.3 Classification of Plasmons

The following considerations are inspired from the book of Le Ru [86]. The original definition above according to Pines does not hit the physical mechanism which is responsible for the field enhancements used and observed in the previous mentioned surface Raman spectroscopy experiments with the wavelength of the laser light ranging in the visible spectrum. Therefore, an electromagnetic wave interacts with the noble metal, i.e. the free-electron plasma. The resulting electromagnetic waves in the metal are mixed photon-plasmon modes called plasmon-polaritons. With focus on the surface of the nanostructure we deal with an interface between a metal (e.g. Au or Ag) and a dielectric medium (e.g. air, vacuum, H₂O, SiO₂,...). At such interfaces propagating longitudinal charge density waves have been predicted later by Ritchi [87] experimentally observed by Powell [88] and quantized as modes in the work of Stern [89]. Since plasmons themselves can exit without coupling to photons (transverse electromagnetic waves), in the case of surface plasmons this is not possible because retardation effects are not negligible. The mixed mode, sharing the energy between the plasmon and photon is strictly speaking a surface plasmon-polariton. From the point, that our calculations will be done in the limit of the electrostatic case we may refer to the pure surface plasmon modes as an approximation of the surface plasmon polariton by neglecting the photon contribution [86]. According to the dimensional comparison between the wavelength of the external excitation and the extension of the nanostructure the localized surface plasmon will be introduced in the following. To come back to the role of the plasmonic effects for the SE(R)R spectroscopy experiments we see, that within the optical response of the solid state its dielectric function $\epsilon(\omega)$ contains all information that needed. This material characterizing function will be the input quantity for our numerical simulations.

Localized Surface Plasmon (LSP)

Surface plasmons are non-localized evanescent waves at planar surfaces. The localized types which cannot propagate are called localized surface plasmon (LSP). The LSP can be viewed classically as a dipole oscillation which is generated through carrier separation alternating in particles smaller than the exciting wavelength, cp. Fig. 5.2. Spheres (10 – 100nm) resonantly excited at their material depending plasma frequency, i.e. $\omega_{exc} = \omega_{pl}$ emit therefore a new electric field which is enhanced in its intensity. The excitation wavelength used in the experiments of Khoa Ly et al. [78] is set to $\lambda = 413$ nm and the average size in the area of interest of the nanostructured electrode is about 50 to 100nm restricting us to the case of localized surface plasmon polaritons.

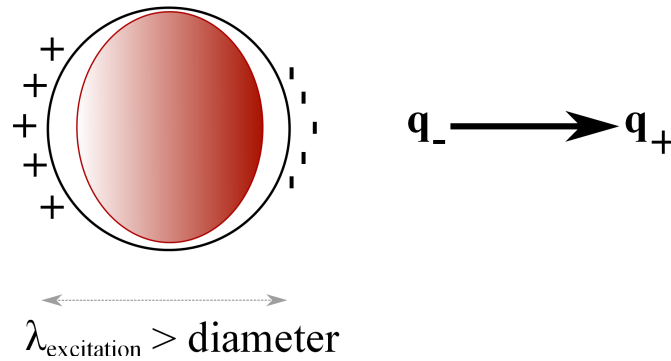


Figure 5.2: When the considered area (e.g. the diameter of a sphere) is smaller than the wavelength of the external excitation the surface plasmon is localized and can be viewed as an oscillating dipole generated through the spatial separation of the electrons from the ionic cores.

5.2 Numerical Simulation of Field Enhancement using the Finite Element Method

5.2.1 Simulation of a Single Nanosphere

In this section we will give an insight how the field enhancement calculations are performed using the Finite Element Solver JCMwave. For detailed technical explanations we refer the reader to the work of Pomplun et al. [90]. To emphasize an example we will model a single gold nanosphere and proceed with two coupled silver spheres covered with a variable platinum coating. The gold

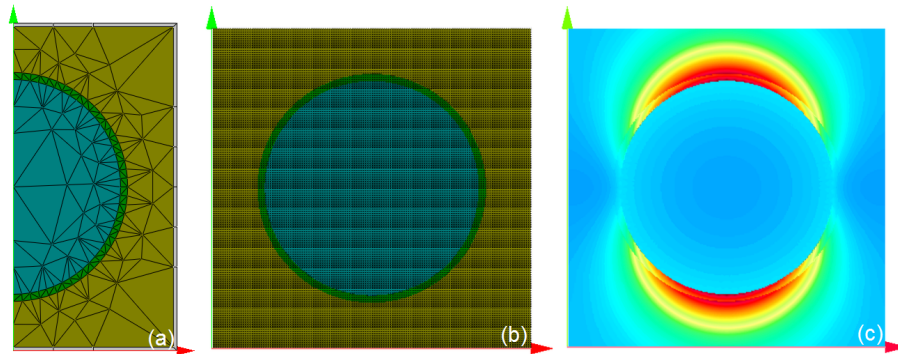


Figure 5.3: Simulation of a gold nanosphere surrounded with H_2O . From left to right are displayed: (a) the triangulated geometry setup of a half-sphere which will be rotated along the y-axis, (b) a cut through the generated sphere in the x-y plane and (c) the distribution of the absolute value of the electric field $|E|$.

nanosphere has a diameter of 60nm with a 2nm thick dielectric SiO_2 spacer and is surrounded with water. As a first step we built up the geometry of the considered structure in the x-y plane

with the y-axis being the rotation axis. The simulation of the sphere can due to the symmetry of the sphere be restricted to a two dimensional problem. This two dimensional layout is further discretized into finite subspaces. Here triangles are used to create a mesh onto the structure via the Finite Element Method, cp. Fig. 5.3 (a). The excitation with light is modeled as planar waves traveling from the front, i.e. along the z-axis into the paper plane. The polarization is chosen to be linear and parallel with respect to the rotation axis. The wave equation (5.8) is further solved on every triangle including the three corner points plus the side lengths. Extrapolating these values to the inner surface of the triangle yields the values for the electric field in all three space components E_x, E_y and E_z for the complete triangle. With these calculated values the rectangular mesh displayed in Fig. 5.3 (b) is generated. The distribution of the absolute value of the electric field strength $|\mathbf{E}| = E_x E_x^* + E_y E_y^* + E_z E_z^*$ is shown in (c) using false colors (blue for low and red for high values of $|\mathbf{E}|$ in $[\frac{V}{m}]$) with respect to a x-y plane cut of the simulated three dimensional nanostructure. The intensity of the field enhancement distributions at the north and south pole of the nanosphere are decaying with further distance which is similar to the oscillation of a dipole. Since the diameter of the sphere is below the wavelength of the excitation we see this effect represented by the localized particle plasmon which we described in the previous section.

5.2.2 Two Coupled Multilayered Nanospheres

As a preliminary stage of the multilayered electrode investigations we simulated two coupled nanospheres with increasing thickness of the platinum coating by lowering at the same time the distance between them. The multilayered structures are composed as follows: two equally separated silver (Ag) spheres with a radius of 30nm with fixed centers and therefore constant distance to each other. Each sphere is surrounded by a 2 nm thick dielectric spacer of SiO₂ and finally covered with a variable platinum coating. The field enhancements are calculated for increasing platinum thicknesses from 1 – 8 nm with a simultaneously decrease of the surface distance between the two spheres from 10 – 2 nm, cp. Fig. 5.4. Like for the single sphere we see a long range plasmon excitation, cp. Fig 5.4 (a). Since the enhancement of the electric field between the spheres is lowered by the screening of the increasing Pt coating the further increase of the Pt thickness leads to a close vicinity between the spheres and a strong increase of the field enhancement appears, cp. Fig. 5.4 (b-c). A direct comparison between the thickness of the Pt coating versus the distance between the sphere surfaces exposes the two counteracting processes: screening versus enhancement. The first arises through the extended Pt coating and the latter via proximity effects of the closer getting surfaces of the two spheres. The proximity effects will be of importance for the interpretation of the experimental observations we are going to describe within our field enhancement calculations in the following sections.

5.3 Surface Enhanced Resonant Raman Spectroscopy

The experiments have been performed in the group of Prof. I. Weidinger by Dr. K. Ly. For their investigations they used the scattered enhanced signal within surface-enhanced resonant Raman

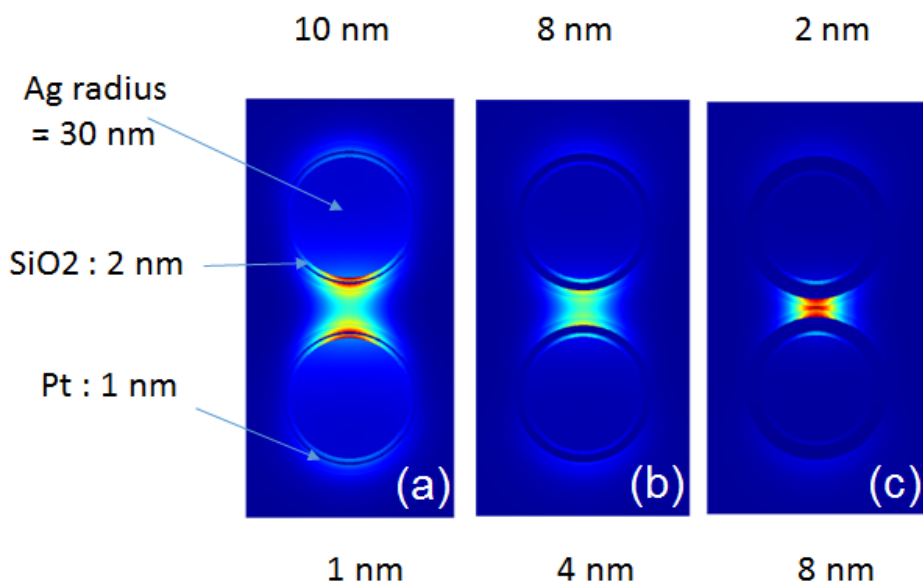


Figure 5.4: Coupled Ag nanospheres with a constant 2 nm dielectric SiO₂ spacer and a from 1 nm to 8 nm variable Pt coating. The increasing Pt thickness leads to a decrease of the surface distance between the spheres from 10 nm to 2 nm while the center of the Ag spheres are fixed for all cases. The simulation sequence from left to right shows two counteracting processes: screening due to rising Pt coating versus enhancement via proximity effects.

spectroscopy (SE(R)RS) to spatially detect and characterize the interaction of probe molecules like mercaptopyridine or the heme protein cytochrome c adsorbed to a multilayered Ag – SiO₂ – Pt electrode [78], cp. Fig. 5.5. These systems are not only interesting for basic research but also open a way to produce biological sensors. We briefly introduce the concept of SE(R)RS for the understanding of the underlying physical mechanisms. The effect that the Raman signal of molecules in close vicinity respectively adsorbed to roughened metal surfaces is enhanced up to 10⁵ times in comparison to unprepared surfaces is described in the work of Fleischmann [92]. Via the gain of the electric field strength amplitude E_0 of the incoming laser light on the surface of the support material the adsorbed probe molecule is excited. Thus a Raman signal is exhibited which is further amplified due to coherent superposition leading to an enhancement factor of the signal corresponding to the absolute value of the electric field amplitude $g = |\mathbf{E}|^4$. In the case of resonantly exciting an electronic transition of the probe molecule (resonant Raman spectroscopy) this leads to further amplification of the Raman signal intensity.

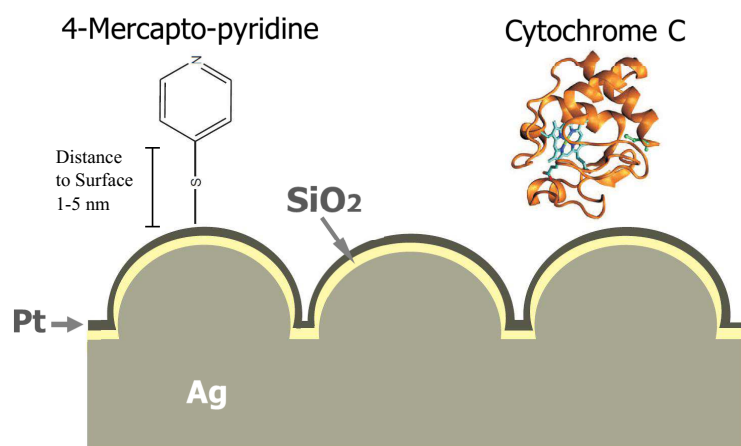


Figure 5.5: Adsorption of the probe molecules mercaptopyridine and protein cytochrome c on the multilayered Ag – SiO₂ – Pt electrode. Picture adapted from [91].

5.4 A Nanostructured Multilayer Electrode : Field Enhancement via Plasmonic Material Features

After the preliminary studies we apply the introduced model to describe and interpret the observed effects in SE(R)RS experiments with probe molecules attached to an Ag-SiO₂-Pt electrode. The following description of our theoretical work in cooperation with the above mentioned experimental group and is published in [78]. The production process of the Ag – SiO₂ – Pt electrode proceed as

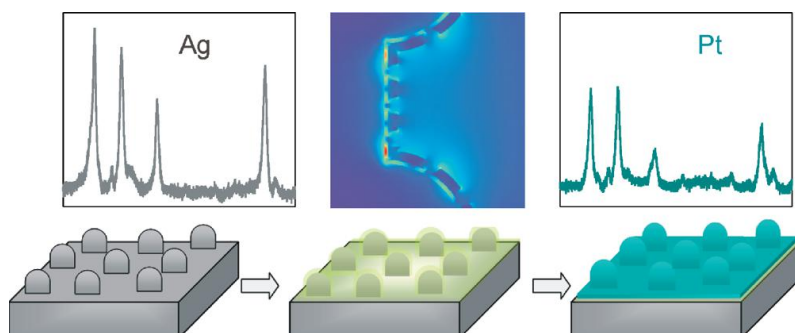


Figure 5.6: Process of preparation of the multilayered Ag – SiO₂ – Pt electrode. From left to right: electrochemically roughening of the Ag bulk, coating with the SiO₂ dielectric spacer and deposition of a Pt island film. Picture adapted from [78].

follows: first a cylindrical Ag bulk electrode was roughened electrochemically and coated with a SiO₂ dielectric spacer of controlled thickness. Completing the structure, the whole electrode was

5.4. A NANOSTRUCTURED MULTILAYER ELECTRODE : FIELD ENHANCEMENT VIA PLASMONIC MATERIAL FEATURES

covered via electrochemical deposition with Pt creating a coral-like structured island film, cp. Fig. 5.6. Since the size of the Pt corals is smaller than that of the Ag support a non perfectly closed surface is resulting. The scanning electron microscope (SEM) picture of the final electrode, cp. Fig. 5.7 compares the Ag with the final Pt coated electrode. From this, one can estimate the size of the Pt nanocorals up to $(30 \pm 10) \text{ nm}$. The theoretical modeling of the geometry layout is shown in Fig.

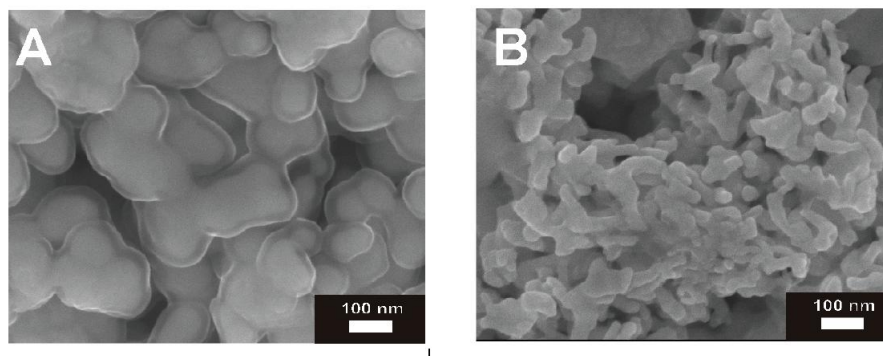


Figure 5.7: Scanning electron microscope picture showing (A) an Ag – SiO₂ and (B) an Ag – SiO₂ – Pt electrode. In comparison the coral size of the final electrode (B) is smaller indicating a non-perfectly closed surface. Picture taken from [78].

5.8. In y-direction we have an infinite long Ag bulk with a height of 100 nm. On this bulk we added three half spheres (bumps) with a radius of $r_0 = 42.5 \text{ nm}$ resembling the average Ag coral size. To account the asymmetry of the real electrode two spheres have been set close together within 6 nm while a third one was placed further away in a distance of 62.5 nm with respect to the center of the second half-sphere. This Ag structure is accordingly to the above described electrode layered by a 2 nm thin dielectric SiO₂ spacer and covered with a Pt coating of 5 nm thickness. To simulate the excitation of the external electromagnetic field we model plane waves propagating along the x direction incoming from the right side. The polarization is linear and parallel respective to the y-axis. According to the experiment, the wavelength is set to $\lambda = 413 \text{ nm}$ and the vector amplitude $|\mathbf{E}_0| = 1 \left[\frac{\text{V}}{\text{m}} \right]$. Through the choice of E_0 , the absolute value of the electric field resembles the total field enhancement. The previous described application of SE(R)R spectroscopy on different probe molecules and silica coating thicknesses revealed, that a non perfect coating of the Pt island film promotes the efficiency of the induced SER activity [78]. The field enhancement distributions obtained from the calculated values of $|\mathbf{E}|$ for the modeled structure shown in Fig. 5.8, reveal the impact of a non-perfectly closed surface, cp. Fig. 5.9. On the left side the closed defect free Pt film exhibit a strong field enhancement between the bumps being in close vicinity, while no surface enhancement in the wider gap and at the top of the half spheres occurs. In comparison with the simulation of the non-perfectly closed Pt surface hybrid electrode, being more realistic concerning to the SEM picture of the created Ag – SiO₂ – Pt structure, cp. Fig. 5.7 (B), a different pattern of the field enhancement distribution shows up. The overall field enhancement increase remarkably,

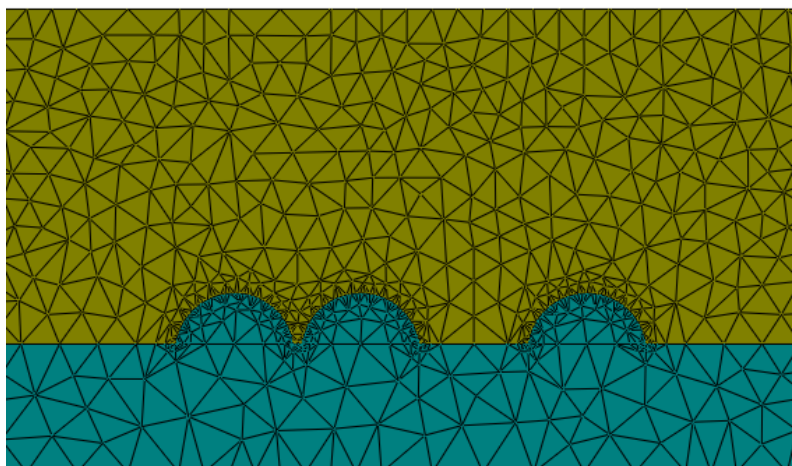


Figure 5.8: Two dimensional layout of the simulated Ag – SiO₂ – Pt electrode after the triangulation process. The asymmetric distribution of the bumps in close vicinity (6nm) and wider range (42.5nm) is not chosen arbitrary for the field enhancement simulation.

mainly in contrast to the closed defect free Pt film. Large enhancements, so called Hot Spots occur at areas where no surface enhancement has been observed before: at the top of the half spheres as also within the wider gap between the second and the third bump. This can be traced back to the fact, that through the non-perfectly closed Pt coating the incoming light reaches now the plasmonic active underlying Ag support creating localized surface plasmons, being responsible for field enhancements. Extremely high local enhancements are observed at the sharp edges, which have been introduced through the hole like defects in the geometry of the hybrid electrodes. Comparing both structures we read out the absolute value of the electric field $|\mathbf{E}|$ 1 nm above the Pt surface at equidistant coordinates. For the adsorbents used in the experiments being attached within this distance the measured enhancement of the Raman signal can be expressed via $g = |\mathbf{E}^4|$. Therefore, we can state, that for the non-perfect Pt film the average SE(R)RS enhancement per surface area is approximately 80% higher. In conclusion two mechanisms of the field enhancement can be identified: Through the induced hole-like defects in the Pt coating localized surface plasmons at the Ag substrate are excited from the incident electromagnetic excitation which enhance the electric field around the Pt surface. Furthermore, the geometrical structure of the coral-like islands produces sharp edges leading to an anisotropic shape creating strong local field enhancements in the sense of the lightning rod effect [93, 94].

5.5. A STUDY OF A NANOSTRUCTURED (TiO₂) ELECTRODE:
FIELD ENHANCEMENT BY RAISING THE ANISOTROPY OF THE MORPHOLOGY

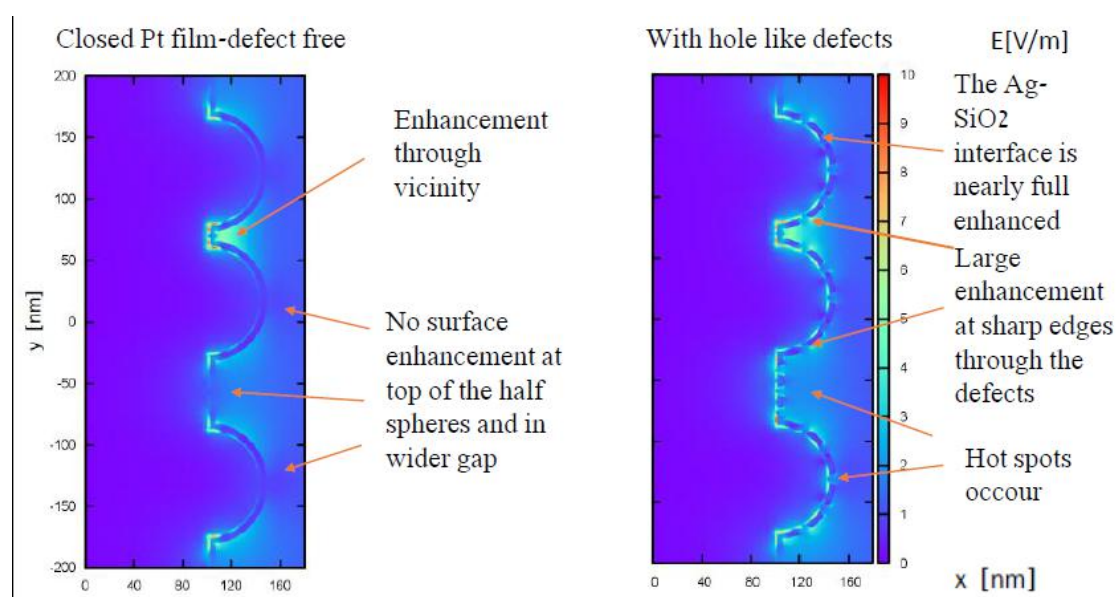


Figure 5.9: Comparison of the calculated field enhancement distributions for two cases: A perfectly closed Pt film (left) and the more close to experiment hybrid electrode (right) with hole like defects resembling the SEM picture with coral islands, cp. Fig. 5.7 (B). Picture modified from [78].

5.5 A Study of a Nanostructured (TiO₂) Electrode: Field Enhancement by Raising the Anisotropy of the Morphology

The electrode which will now be investigated is made of nanostructured titanium dioxide TiO₂, which is in contrast to Ag or Au a non-plasmonic material [79]. Since TiO₂ is semiconductive, plasmons cannot be excited due to the fact that the prerequisite of a free electron gas is not given. TiO₂ shows a high biocompatibility being nontoxic and environmentally friendly and is therefore of great interest for biomedical applications [95, 96]. As a probe molecule in this study the heme domain of human sulfite oxidase cytochrome *b*₅ (cyt *b*₅) is taken. The observed SE(R)R effect in contrast to the previous described findings for the multilayered Ag – SiO₂ – Pt electrode has been suggested to result from a chemical mechanism [97, 98] and not from a surface plasmon resonance. The SEM images of the anodized TiO₂ electrode are shown in Fig. 5.10. While (A) displays the electrode under an applied anodization voltage of 10V, (C) is recorded after the voltage was doubled to 20V. The respective magnifications (B) (10V) and (D) (20V) document the increase of the surface roughness, i.e. the accumulation of the anisotropy by raising the anodization voltage. It can be seen that during this process the surface roughness of TiO₂ is highly increased and therefore the electrode exhibits a larger surface. Also the shape of the nanostructured surface is getting more anisotropic. The SE(R)R measurements done in the group of Prof. I. Weidinger

and Prof. P. Hildebrandt revealed that by the change of the surface properties via the described anodization process the enhancement factor raise up from 2.4 to 8.6. The above suggested chemical mechanism is depends on the fact that the probe molecules are bound directly to the TiO_2 surface. This is not the case here, which is rationalized in previous measurements of Weidinger et al. [99] where the average distance between the surface and the edge of the heme protein such as cyt b_5 is approximately 1.5 nm. So the induced charge transfer transition taking place within (sub)picoseconds presume a shorter distance than the measured one, thus making a fast electron transfer unrealistic. From this we proposed another explanation based on electromagnetic effects enabling the surface morphology of the TiO_2 electrode being responsible for the enhanced intensity of the SE(R)R signal. The previous mentioned lightning rod effect [93, 94] depending on the stage of anisotropy of the considered nanostructured electrode could explain the occurrence of large electric field intensities in the vicinity of high curvatures of the surface of the electrode even the material is a not plasmonic active. To check this hypothesis, calculations of the electric field enhancement were performed using the dielectric function of rutile TiO_2 [100]. An electrode-like surface was approximated by ellipsoidal half spheres on a flat bulk electrode which was expanded to infinity along the y -axis. A plane wave with a wavelength of $\lambda_0 = 413$ nm propagating along the x direction, incident from the right side and parallel polarized to the y - (rotation) axis represented the external electromagnetic field. Two half ellipsoids were set in close distance to each other, while a third one was positioned further away. The only parameter that has been varied was the aspect ratio of the two half axes of the half ellipsoids. For an aspect ratio of 1 no significant field

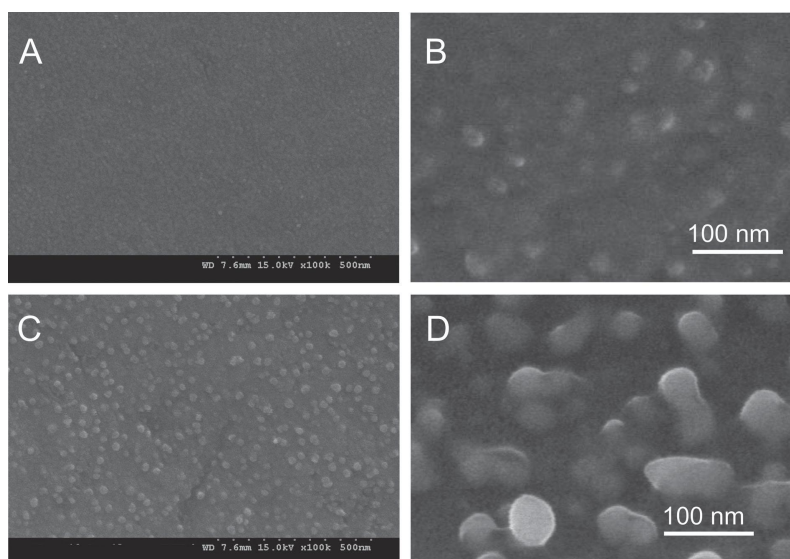


Figure 5.10: SEM images of the TiO_2 electrode at different stages of anodization: (A) with 10 V and (C) with 20 V. The pictures (B) and (D) are magnified images of (A) and (C), respectively. Picture taken from [79].

5.5. A STUDY OF A NANOSTRUCTURED (TiO₂) ELECTRODE:
FIELD ENHANCEMENT BY RAISING THE ANISOTROPY OF THE MORPHOLOGY

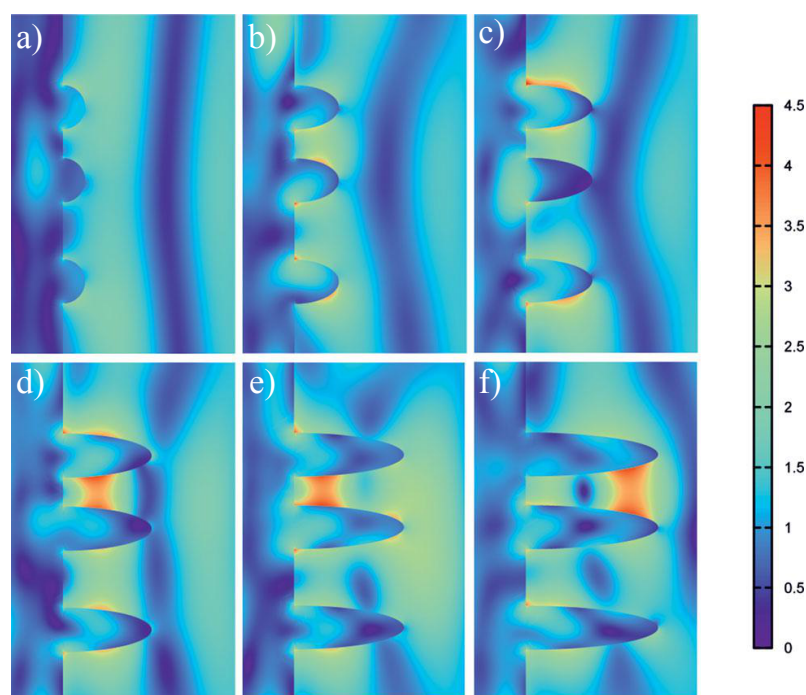


Figure 5.11: Dependence of the field enhancement from the stage of anisotropy. The incoming electric field amplitude $|E_0| = 1 \left[\frac{V}{m} \right]$ allows direct comparison of the displayed enhancement. The TiO₂ electrode modeled as half ellipsoids with varying aspect ratios from 1 to 6 according to (a) to (f). Picture modified from [79].

enhancement can be seen, cp. Fig. 5.11 (a). The local field close to the TiO₂ surface is increased for aspect ratios of 2 (b) and 3 (c). Here, no difference between the two closely adjacent half ellipsoids and the isolated are found. When the aspect ratio is further increased to 4 (d), a strong electric field enhancement is evaluated in the gap between the two adjacent half ellipsoids. Extending the aspect ratio to 5 (e) and finally 6 (f) does not alter the overall field enhancement but the position of the Hot Spot in the gap changes. Assuming that the enhancement of the electric field is the same for the incident light ($|\mathbf{E}_0|$) as for the Raman scattered light, the forth power of the calculated values correspond to the enhancement factor of the Raman scattering. This leads to a broad distribution of the local Raman enhancement ranging from 1 to approximately 400. Therefore, the experimentally determined enhancement factors of up to 10 referring to the average value of all adsorbed molecules contributing to the detected intensity can be well rationalized by the calculations.

5.6 At a Glance

We investigated the origin of experimentally observed enhanced Raman signals for the probe molecules heme protein cytochrome *c* (Cyt-*c*) and cytochrome *b*₅ adsorbed to a multilayered Ag – SiO₂ – Pt electrode and a nanostructured titanium dioxide TiO₂, respectively. The experimental observed effects are rationalized by the performed calculations by solving the full Maxwell equations within a finite-element method. We reveal with our investigations mainly two effects of leading to field enhancements:

- through the excitation of localized surface plasmons (LSPs) (depends on the electronic material properties)
- influence of high curvature effects increasing the anisotropy of the surface morphology originating from the lightning rod effect [94]

5.6. *AT A GLANCE*

6

Photoluminescence Enhancement of CNTs via Coupling to Noble Metal Nanoparticles -An Outlook-

Not only to hybrid electrode structures like the one investigated in the last chapter different probe-molecules have been attached creating strictly speaking a new physical system with its own special properties. Through the adsorption of molecules to the surface of carbon nanostructures, for example a new field of hybrid systems with distinct and controllable properties was opened [101]. This chapter tries to build a bridge between the special properties of single walled carbon nanotubes studied within the PLE process in the prior chapters 3 and 4 and the influences of nanostructured noble metals leading to intense field enhancements. The experiments done by Dr. A. Setaro and M. Glaeske in the group of Prof. S. Reich created a new type of nanostructures called π -hybrids. They are composed of semiconducting single-walled carbon nanotubes combined with gold nanorods of different size, cp. Fig. 6.1. The novel structure exhibits an enhancement in the intensity of PLE emission spectra and a measured blue shift with respect to the spectra of the pristine carbon nanotube. The strength of both effects depend on the specific properties of the tube. We will introduce and describe the experiments and further make the attempt to formulate which underlying enhancement mechanisms could explain the findings.

6.1 π -Hybrids Exhibiting Novel Properties of Enhancement Mechanisms

In general carbon nanotubes show a very low Photoluminescence yield within the the process of PLE which we extensively studied in our work on relaxation dynamics. The values range from 0.05 % for CNTs in solution [102] to 3 % for suspended [103] up to 20 % for tubes dispersed with special oxygen-excluding surfactants [104]. Experiments performed with CNTs deposited on Au films showed ten-folds enhancements in the emission spectra of the tubes whose E_{22} transition matched with the plasmonic frequencies of the Au surface [105]. In the work of Setaro and Glaeske a novel approach leading to an enormous PLE enhancement up to factors of 8 for the (7,6) and 20 for the (8,4) tube has been made. The authors combined gold nanorods (AuNR) with average lengths and diameters of 100nm and 20nm with single walled carbon nanotubes being up to a few micrometers in length, cp. Fig. 6.1. This has been achieved by a variant of the micelle swelling technique [106] where to non water soluble SWCNTs have been added gold nanorods (AuNR) stabilized with micelles in water, cp. Fig 6.2. To point out the plasmonic character of the system, the nanoplasmonic colloidal dispersion have been called π -hybrids. The π -hybrids have further been investigated within photoluminescence excitation experiments and compared to samples only containing nanotubes without the AuNR, labeled CTAB. The CTAB sample shows prominent intensity peaks from which the (9,4), (7,5), (7,6) and (8,4) tubes have been identified, cp. the PLE charts in Fig. 6.3. Further, the PLE chart for the π -hybrid sample shows an extensive

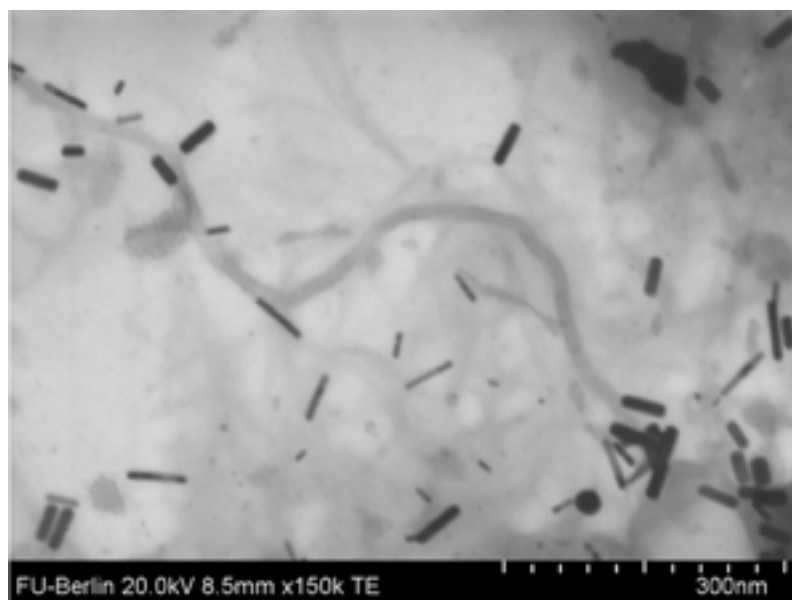


Figure 6.1: SEM picture of the π -hybrid deposited on a grid substrate, [107]. The size scale difference between the nanorods and the nanotubes indicates that the coupling is a local effect.

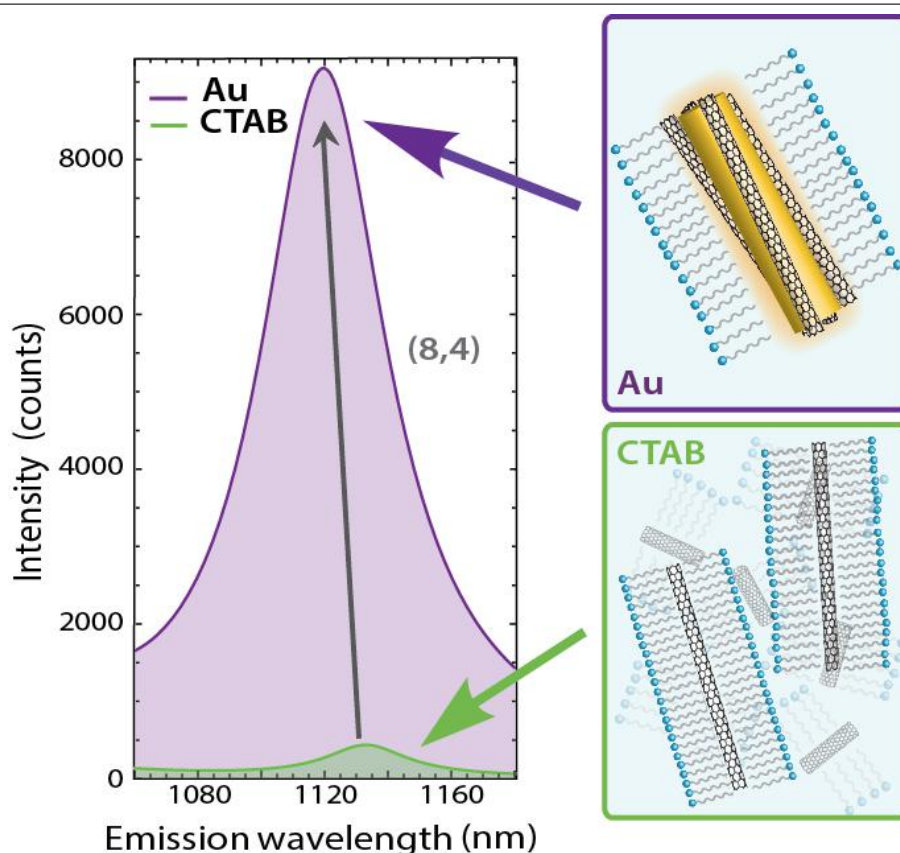


Figure 6.2: A new class of hybrids composed of gold nanorods of 100nm in proximity to carbon nanotubes being up to a few μm in length. Picture taken from [20].

enhancement of the intensity for mainly the π -hybrids composed from the (7,6) and (8,4) tubes. By considering a single excitation and a single emission wavelength a comparison of the emission and excitation spectra of both samples show interesting results. In the excitation spectra different enhancements of the maximal intensities for the tube transitions $E_{22}^{(8,4)}$, $E_{22}^{(7,6)}$ and $E_{22}^{(9,4)}$ lying along the fixed emission wavelengths are observed. In the emission spectra beside the intensity enhancement a blue shift for the hybrid with respect to the comparative sample shows up. The same position of the intensities in the excitation spectra indicate that the E_{22} transition for these tubes do not alter in the π -hybrid formation. In contrast, the shifting of the intensity peaks to larger energies within the emission spectra of the π -hybrid sample exhibit, that the E_{11} transition energy changes. In other words the band gap energy E_{11} is exceeding to larger values or the radiative recombination of the electrons with the holes starts at higher energies and the relaxation of the excited carriers does not reach the E_{11} transition, i.e. the lifetime of the excitons is shortened.

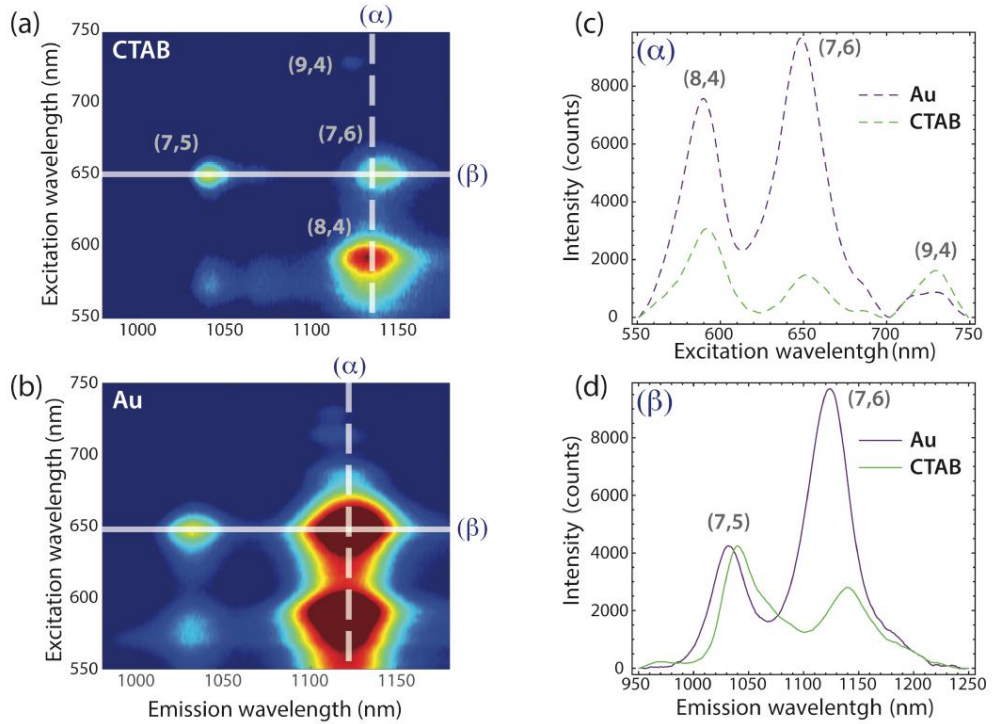


Figure 6.3: PLE charts obtained for the sample containing (a) only CNTs denoted with CTAB and (b) the π -hybrid samples. Along a constant excitation energy including the maximum intensities of the (7,5) and (7,6) tubes, i.e. their E_{22} transition energies a cutting line (β) of the PLE chart yield the emission spectra shown in (d). An analogue cut (α) at a constant emission wavelength passing the intensity maxima of the (8,4), (7,6) and (9,4) tube provide the excitation spectra shown in (c). Within the excitation and emission spectra an intensity enhancement is observed comparing the π -hybrid with the CTAB sample. Interestingly in the emission spectra also a blue shift towards smaller wavelengths, i.e. larger energies of the π -hybrid with respect to CTAB sample occurs, taken from [20].

6.2 Discussion of the Origins of the Observed Effects

The investigation of the π -hybrids revealed two effects:

- enhancement of the excitation and emission intensities depending on the specific tube
- blue shift in the range of 20 meV in the emission spectra for the π -hybrid with respect to the pristine tube, i.e. a change of E_{11} to higher energies.

We now discuss the observed effects and try to give an interpretation of the possible physical origins with the knowledge gained from our results of the relaxation dynamics in CNTs and the field enhancement calculations from the previous chapters.

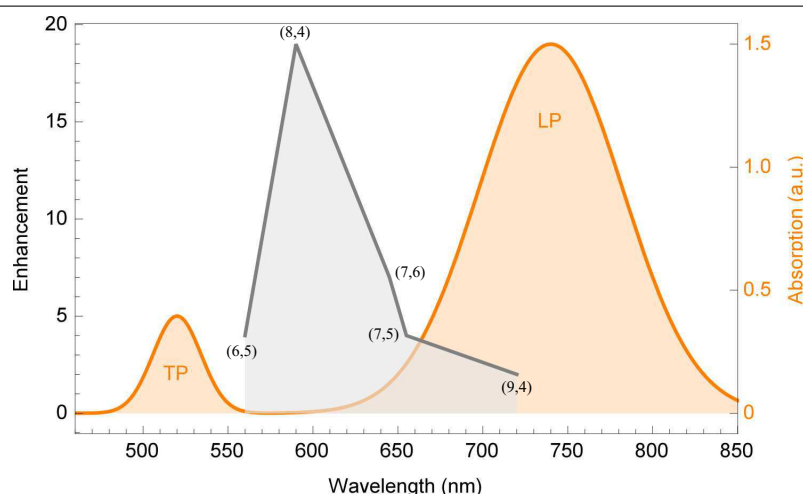


Figure 6.4: Absorption spectra for gold nanorods (AuNR) exhibiting the transverse (TP) and longitudinal (LP) plasmon absorption bands. The gray shaded area displays the range in which the enhancement of the tubes contained in the π -hybrids is observed. That the range of main enhancement does not cover the area of maximum absorption of the plasmonic gold nanorods indicates that the enhancement does not rely on the plasmonic features of the AuNR, [108].

6.2.1 Enhancement Effect

As mentioned, the enhancements differ remarkably with respect to the considered chiral species. It can be seen that the enhancement of the PLE intensity for the (8,4) tube in comparison with the (7,5) tube is about 5 times larger, cp. Fig. 6.4. Thus we compare the density of states for both tubes, cp. Fig. 6.5. For the (8,4) tube the density of states of the E_{11} and E_{22} transition is about 3.4 and approximately 3 times larger with respect to the (7,5) tube. This reveals that the tube specific density of states could be a feature which would be transferred to the π -hybrid being therefore responsible for the different strengths of enhancements. Furthermore, comparing the absorbance of the gold nanorods with the enhancement of the tubes emission it can be seen, cp. Fig. 6.4 that the wavelength range for the maxima of the transverse and longitudinal plasmon frequencies of the AuNR do not cover the area in which the enhancement of the PLE intensities is observed. From this, we can conclude that the plasmonic features of the AuNR are not the only contribution for the observed enhancement of the π -hybrid. That implies that other mechanisms come into play behind this phenomena. As the separation between the maximum of the enhancement and the plasmon band is approximately 200 meV the phonon modes of the CNT could be responsible for the mediation of the excitation from the AuNR. We plan to extend our previous relaxation studies (see Chap. 4) to the case where coupling to noble metal nanostructures will assume a keyrole in the optical process.

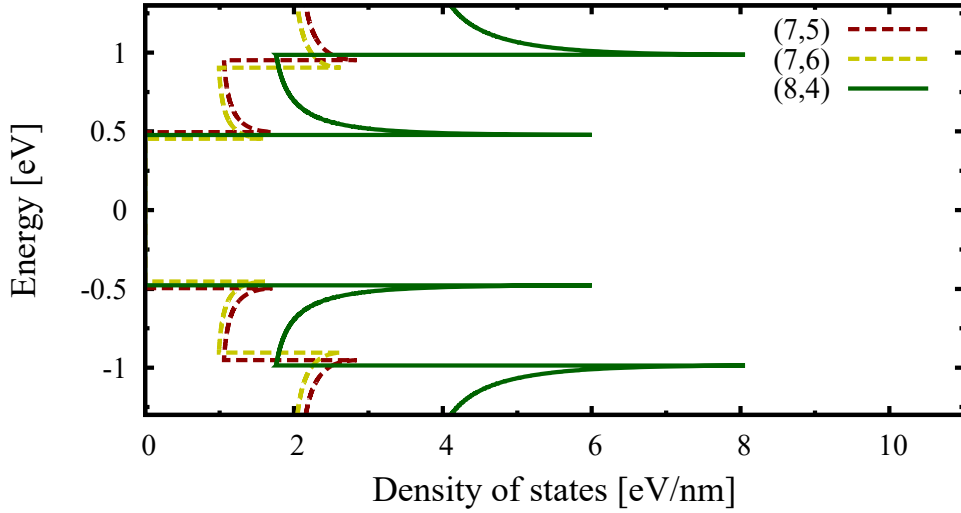


Figure 6.5: Density of States for the investigated (7,5), (7,6) and (8,4) tube. The DOS is plotted over energy for the first and second optical transition energies E_{11} and E_{22} , respectively [46].

6.2.2 Energy Shift of the E_{11} Transition

The second effect of shifting the lowest energy transition towards higher energies for the π -hybrid can have several explanations which we try to sketch in the following. The surface plasmon properties of the AuNR alone cannot fully explain the experimental observations, we shall take into account. The proximity effect like the one we studied within our field enhancement calculations in the previous chapter could be considered. By bringing several noble metal nanostructures in close vicinity to the nanotube high electric fields would arise from. These fields could now have an remarkable influence the electronic properties of the involved nanotube. It has been shown, that such high intense local fields could alter the band structure of a semiconductor such a way, that so called subband gaps can open up constituting a forbidden area within the band structure where the carriers cannot relax any further [109]. Thus these subband gaps could reduce the excitonic lifetime through recombination of electron and holes before they would have been relaxed through carrier-phonon scattering towards the band edges of the lowest lying subbands. This could result in a blue shift in the optical spectra and an enhanced Raman signal indicating a change in the electron-phonon coupling. In [110] the authors describe via exciton dynamic calculations for nanowire assemblies with Au nanoparticles that in the emission spectra of their produced hybrid

superstructure the observed occurring blue shift results from a shortening of the excitonic lifetimes.

6.3 At a Glance

We presented the novel designed Π -hybrids from Setaro et al. exhibiting an enormous enhancement depending on the specific tube and a measurable blue-shift with respect to the pristine tube. For the first observation the tube specific DOS could be a key feature that is transferred to the π -hybrids and furthermore the phonon modes of the CNT could be responsible for the mediation of the excitation from the AuNR. The effect of shifting to higher energies could result from proximity effects arising from the close vicinity of the AuNR, creating high intense local fields that subband gaps can open up reducing the excitonic lifetime.

6.3. *AT A GLANCE*

7

Conclusion

In the above thesis we have investigated ultrafast relaxation processes of optically excited carriers in semiconducting single-walled carbon nanotubes (SWCNTs) via the density matrix formalism. Time- and momentum-resolved relaxation dynamics have been calculated by including the phonon-induced intra- and inter-subband scattering channels [15]. This enables us to deduce the pathways of non-equilibrium carriers that are traced back to within the lowest lying conduction subbands for a variety of semiconducting CNTs. We found that the different scattering dynamics resulting from the respective phonon mode lead to experimentally-distinguishable relaxation times. Our calculations unveil that optical phonon modes -with their large discrete energies, give rise to relaxation times within a few hundred femtoseconds. In contrast, acoustic phonons lead to relaxation times in the range of only a few picoseconds. This may be ascribed to the restrictions imposed by energy and momentum conservation; the smaller slope of the acoustic phonons versus the relevant electronic bands only allows scattering processes with small momentum transfer. Since the acoustic carrier-phonon coupling element scales linearly with the phonon momentum, its dynamics are slower in relation to the optical phonons [76]. Using a recent experimental two-color pump-probe study revealing a bi-exponential decay, we were able to assign the observed faster picosecond decay time τ_1 to intraband scattering with acoustic phonons in the vicinity of the E_{11} transition [16]. Moreover, through an extensive analytical treatment of the equations of motion we were able to investigate a large variety of semiconducting tubes with a view towards global relaxation time-dependencies like diameter and chirality. We unveiled the impact of tube specific parameters like the conduction subband gap and their respective curvatures. Our investigation of the diameter and chirality dependence revealed that the fastest dynamics occur primarily for zig-zag tubes of relatively small diameter. We observed a partially contrasting behavior for acoustic and optical phonons due to their correspondingly different phonon dispersion relations, resulting in different

scattering efficiencies. On enabling intersubband channels in an extended two-band model we demonstrated that intersubband scattering processes may only be mediated via optical phonons; the energy of acoustic modes is not large enough to pass the energetic separation between the subbands. A recent experiment with chirality-enriched CNT samples of (7,6) and (7,5) tubes pumped and probed resonantly to E_{22} and E_{11} , respectively, found a fast component τ_1 in the range between 6 and 15 ps. This fast relaxation time was found to be in excellent accord with our theoretically predicted relaxation times stemming from intraband scattering with acoustic phonons. Furthermore, we computed the diameter dependence of this relaxation time. On probing energies just below the E_{11} transition while keeping the pump energy constant at E_{22} , a slowing-down behavior has been observed experimentally. This observation was successfully rationalized via our theoretical model, thereby proving the impact of acoustic phonons and revealing relaxation times in the picosecond range towards E_{11} , [17]. It actually originates from the linear acoustic phonon momentum transfer deriving from the electron-phonon matrix element. This linear dependence leads to a weaker coupling between the scattering processes near the band edge and therefore to a slowing-down of the corresponding relaxation. Remarkably, varying the pump energy, while keeping the probe energy constant, revealed relatively constant relaxation times. We rationalized this observation by arguing that the pump energy acts via the optical coupling and does not have an impact on subsequent relaxation process. We believe that these insights shall aid the understanding of scattering processes important for the relaxation dynamics of photoluminescence excitation process driven by acoustic and optical phonons. Overall, the study of the close competition between intra- and intersubband scattering is found to be critical in interpreting pump-probe experiments. Towards the goal of designing optimal geometries for field enhancement in experimentally-investigated hybrid systems, the full Maxwell equations were solved using a finite element method employing the Maxwell Solver JCMsuite (in collaboration with the Konrad-Zuse Institut Berlin). This led to the calculation of the field enhancement distribution for a multilayered platinum covered silver (Ag – SiO₂ – Pt) electrode. Such a model system closely corresponds to SE(R)RS experiments for molecules attached to silica coated nanostructured Ag electrodes. We were able to successfully trace the experimental results to hole-like defects in the Pt film that generated field hot-spots raising the average SE(R)RS enhancement to approx. 80%, as elucidated in Ref.[78]. The induced defects in the Pt island film gave rise to incident electromagnetic excitation onto the underlying Ag substrate creating localized surface plasmons (LSPs) leading to an enhancement of the electric field in the vicinity of the Pt coating. Additionally, the geometrical structure of the coral-like islands were observed to produce sharp edges resulting in an anisotropic shape creating strong local field enhancements akin to the lightning rod effect [93, 94]. Next, we fruitfully applied our model to a titanium dioxide (TiO₂) electrode allowing the probing of the cofactor of immobilized cyt *b*₅ by SE(R)R spectroscopy. The observed increasing enhancement factor dependence relying on the anodization voltage was rationalized from our calculations, revealing that this trend stems from the burgeoning anisotropy of the surface morphology, as detailed in [79]. Finally, we presented a current experiment on novel nanostructures called π -hybrids [20, 107]. It exhibits an enhancement in the intensity of PLE emission spectra and a measured blue-shift with respect to the spectra of the pristine carbon nanotube. The strength of both effects depend

on the specific properties of the tube. Our insight to the relaxation dynamics of semiconducting CNTs and field enhancement processes shall facilitate the future work on such novel π -hybrids in order to comprehend the exhibited enhancement of their emission spectra. The appreciation of the underlying mechanisms shall enable the optimization of the morphology of the π -hybrids for targeted optoelectronic applications.

8

Appendix

8.1 Approximations

8.1.1 Instantaneous Scattering-Markovian Dynamics

To perform the analytic integration of the phonon assisted quantities we use the Markov Approximation. For a differential equation

$$i\hbar d_t y(t) = y(t) \cdot \Delta E + f(t), \quad (8.1)$$

we yield through integration

$$i\hbar y(t) = y_0 \cdot e^{i\Delta E \cdot t} + \int_{t_0}^t dt' f(t') \cdot e^{i\Delta E \cdot t}. \quad (8.2)$$

Setting the initial value y_0 to zero, meaning that at the initial point in time no coherences exist and letting the lower integration limit go to $t_0 = -\infty$ we can transform the integral to:

$$i\hbar y(t) = \int_{-\infty}^t dt' \tilde{f}(t') \cdot e^{iE_{\tilde{f}} \cdot t'} \cdot e^{i\Delta E \cdot (t-t')} = \int_{-\infty}^t dt' \tilde{f}(t') \cdot e^{i(\Delta E - E_{\tilde{f}}) \cdot (t-t')} \cdot e^{iE_{\tilde{f}} \cdot t}. \quad (8.3)$$

Substituting the integration variable with $s = t - t'$, $ds = -dt'$ and $-\infty \rightarrow \infty, t \rightarrow 0$ we have:

$$i\hbar y(t) = \int_0^{\infty} ds \tilde{f}(t-s) \cdot e^{i(\Delta E - E_{\tilde{f}}) \cdot s} \cdot e^{iE_{\tilde{f}} \cdot t}. \quad (8.4)$$

The essence of this approximation is the negligence of the memory kernel of the integral, i.e. $\tilde{f}(t-s) \approx \tilde{f}(t)$. Physically a particle retains memory of previous scattering events with other

8.1. APPROXIMATIONS

carriers in the system. Within the Markov approximation we neglect all these memory effects, which means that only processes that fulfill the energy conservation, expressed by the δ -function are taken into account:

$$y(t) = -\frac{i}{\hbar} \tilde{f}(t) \cdot e^{iE_f t} \int_0^\infty ds e^{i(\Delta E - E_f) \cdot s} = -\frac{i}{\hbar} f(t) \int_0^\infty ds e^{i(\Delta E - E_f) \cdot s}. \quad (8.5)$$

Using the relation for the δ -function [111] we have

$$\frac{1}{i} \int_0^\infty dk e^{ikx - \varepsilon k} = \frac{1}{x + i\varepsilon} = \frac{x - i\varepsilon}{x^2 + \varepsilon^2} = P \frac{1}{x} - i\pi \delta(x), \quad (8.6)$$

with P being the principal value of the integral, demanding that for the integration over $\frac{1}{x}$ the negative and positive area parts (which become infinite) have to compensate each other. In general this value is neglected and only the δ -function represents the integral. Finally the integration of the differential equation within the Markov approximation yields:

$$y(t) = -\frac{i}{\hbar} \pi \cdot \delta(\Delta E) \cdot f(t) \quad (8.7)$$

8.1.2 Bath Approximation for the Phononic System

Within this approximation the phonons are treated as a thermal bath surrounding the fermionic electrons. The phononic system cannot be influenced through the transferred scattering energy of the electrons. Therefore, the bath is not driven out of equilibrium. The expectation values of the creation and annihilation operators define the phononic occupation number which is given via the Bose-Einstein distribution. Thus the phonon distribution depends on the temperature of the bath:

$$n_q^\gamma = \langle b_{-q\gamma}^+ b_{q\gamma} \rangle = \frac{1}{\exp\left(\frac{\hbar\omega}{k_b T}\right) - 1}. \quad (8.8)$$

With this assumption the expectation values vanish

$$\langle b_{q\gamma} \rangle = 0, \quad (8.9)$$

$$\langle b_{-q\gamma}^+ \rangle = 0, \quad (8.10)$$

$$\langle b_{-q\gamma}^+ b_{-q\gamma}^+ \rangle = 0, \quad (8.11)$$

$$\langle b_{q\gamma} b_{q\gamma} \rangle = 0, \quad (8.12)$$

because coherences don't exist in thermal equilibrium. This approximation is used within our calculations with at room temperature $T = 300$ K.

8.2 Phonon Dynamics

The equation of motion for the dynamics of the phonon distributions reads:

$$\dot{n}_{\mathbf{q}}^{\gamma}|_{sc} = \frac{2\pi}{\hbar} \sum_{\lambda\lambda'\mathbf{k}} |g_{\mathbf{kq}}^{\lambda\lambda'\gamma}|^2 \delta(\varepsilon_{\mathbf{k}+\mathbf{q}}^{\lambda} - \varepsilon_{\mathbf{k}}^{\lambda'} - \hbar\omega_{\mathbf{q}}^{\gamma}) Z_{\mathbf{kq}}^{\lambda\lambda'\gamma}, \quad (8.13)$$

with

$$Z_{\mathbf{kq}}^{\lambda\lambda'\gamma} := \rho_{\mathbf{k}+\mathbf{q}}^{\lambda} (1 - \rho_{\mathbf{k}}^{\lambda'}) (n_{\mathbf{q}}^{\gamma} + 1) - (1 - \rho_{\mathbf{k}+\mathbf{q}}^{\lambda}) \rho_{\mathbf{k}}^{\lambda'} n_{\mathbf{q}}^{\gamma}. \quad (8.14)$$

We note, that now the summation runs over the electronic momenta \mathbf{k} and different bands $\lambda\lambda'$. Analogous to the electronic distribution expectation values for two electronic and one phononic operator occur which are treated similarly within the Hartree-Fock factorization. This leads to a Boltzmann scattering equation displaying the emission and absorption of phonons between two electronic states represented by a single delta-function. For the electronic dynamics three different states have to be considered. Because the emission and absorption of phonons are equal processes, two states are sufficient. The choice of $\delta(\varepsilon_{\mathbf{k}-\mathbf{q}}^{\lambda} - \varepsilon_{\mathbf{k}}^{\lambda'} + \hbar\omega_{\mathbf{q}}^{\gamma})$ would also have been possible. For the phonon distributions considering the dynamics in and between the two lowest lying conduction subbands the summation of $\lambda\lambda'$ runs over C_1, C_2 . To obtain the analytical solution of the phonon occupation dynamics we have to solve now the δ -function depending on the electronic momentum k . Therefore, the zero points of $f(k)$ have to be calculated which is done for different phonon modes in the following. The general analytic solution of the phonon dynamics states for an arbitrary phonon mode γ :

$$\dot{n}_{\tilde{q}}^{\gamma}|_{sc} = -\frac{L}{\hbar} \sum_{\lambda\lambda'} |g_{k_0q}^{\lambda\lambda'\gamma}|^2 \frac{1}{|\mathfrak{Z}_q^{\lambda\lambda'\gamma}|} Z_{k_0\tilde{q}}^{\lambda\lambda'\gamma}, \quad (8.15)$$

with $\tilde{q} = k \mp k_0$.

8.2.1 Optical Modes

For optical phonon modes the electronic zero points

$$k_0 = k_q^{\lambda\Gamma\text{TO}} = \frac{q}{2} \left(\frac{\hbar\omega^{\Gamma\text{TO}}}{\alpha_{\lambda} q^{-2}} \right), \quad (8.16)$$

depend on the inverse square of the phonon momentum. The resulting prefactors

$$\mathfrak{Z}_q^{\lambda\Gamma\text{TO}} = 2\alpha_{\lambda} q, \quad (8.17)$$

scale linear with the phonon momentum q . This scattering transfer for the electronic distributions reflects the constant phonon energy, whereas for the electron dynamics the scattering transfer contains a root dependence reflecting the approximation of a parabolic band structure.

8.2.2 Acoustic Modes

The zero points calculated for an acoustic mode state

$$k_0 = k_q^{\lambda \Gamma LA} = \alpha_\lambda q^2 \left(\frac{\beta}{\alpha_\lambda} \frac{|q|}{q^2} - 1 \right). \quad (8.18)$$

The prefactor in contrast does not change since the first derivation $d_k f(k)$ is constant. Therefore, the prefactors for optical and acoustic phonons emphasizes to be the identical:

$$\boxed{\mathfrak{Z}_q^{\lambda \Gamma LA} = \mathfrak{Z}_q^{\lambda \Gamma TO}}. \quad (8.19)$$

8.3 Solution of the δ -Function

In the following we will describe the procedure how the δ -function can be solved in the case of one-dimensional structures like nanotubes and discuss the emerging scattering prefactors and jump amplitudes. Through the δ -function the energy between two fermionic levels under emission or absorption of a boson is conserved:

$$\delta(\varepsilon_{1\pm 2}^x - \varepsilon_1^y \pm \varepsilon_2^z). \quad (8.20)$$

The Boltzmann scattering equations have the same structure given through a summation over the momenta of the scattering partners. They include the electron phonon coupling element $g_{\mathbf{k}\mathbf{g}}^{\lambda\lambda'\gamma}$ in second order perturbation theory, a function $P(k)$ containing the Pauli blocking terms of the fermions and occupations of the bosons and the momentum dependent energy conserving δ -function. The latter we can rewrite, as it represents a function $f(k)$, as sum of δ -functions of the difference between its variable and the zero points of the inner function weighted with the absolute value of the first derivation at the zero points k_n [111]

$$\sum_k \delta(f(k)) P(k) = \sum_k \sum_n |d_k f(k)|^{-1} \delta(k - k_n) P(k). \quad (8.21)$$

The discrete summation over the variable can be transferred into an integration

$$\sum_k = \frac{1}{\Delta k} \sum_k \Delta k \longrightarrow \frac{L}{2\pi} \int dk, \quad (8.22)$$

with $\Delta k = \frac{2\pi}{L}$ or $L \Delta k = 2\pi$ with L standing for the length of the solid, which in case of CNTs is the length of the tube. Using the definition of the δ -function [111]

$$\int dk \delta(k - k_0) P(k) = P(k_0), \quad (8.23)$$

leads to the analytical expression

$$\sum_k \delta(f(k)) P(k) = \frac{L}{2\pi} |d_k f(k_0)|^{-1} P(k_0), \quad (8.24)$$

in which sense the above derived Boltzmann-like scattering equations are now formulated.

8.4 Basic Constants Used in the Thesis

physical constant	symbol	SI units	eV-K-nm-fs- e_0 units
Planck constant	\hbar	$1.054573 \cdot 10^{-34}$ Js	0.658212 eVfs
speed of light in vacuum	c	$2.997925 \cdot 10^8$ m/s	$2.997925 \cdot 10^2$ nm/fs
elementary charge	e_0	$1.602177 \cdot 10^{-19}$ C	1. e_0
Boltzmann constant	k_B	$1.380658 \cdot 10^{-23}$ J/K	$8.617386 \cdot 10^{-5}$ eV/K
electron mass	m_0	$9.109390 \cdot 10^{-34}$ kg	5.685631 fs ² eV/nm ²
mass of carbon C_{12}	$M_{C_{12}}$	$1.994425 \cdot 10^{-26}$ kg	$1.244812 \cdot 10^{-7}$ fs ² eV/nm ²

Table 8.1: The natural constants are given in SI-units as also in *eV-K-nm-fs- e_0* units. The latter one have been used within the simulation of the relaxation dynamics in CNT dimensions.

Bibliography

- [1] R. P. Feynman. *The Character of Physical Law*. BBC, 1965.
- [2] E. Malic and A. Knorr. *Graphene and Carbon Nanotubes: Ultrafast Optics and Relaxation Dynamics*. Wiley-VCH, Berlin, 2013.
- [3] Sumio Iijima. Helical microtubules of graphitic carbon. *Nature*, 354(8):56–58, 1991.
- [4] M.S. Dresselhaus, G. Dresselhaus, and R. Saito. Physics of carbon nanotubes. *Carbon*, 33(7):883 – 891, 1995. Nanotubes.
- [5] P. Avouris, M. Freitag, and V. Perebeinos. Carbon-nanotube photonics and optoelectronics. *Nature Photonics*, (2):341–350, 2008.
- [6] Dresselhaus M. S. Dresselhaus G. Jorio, A. *Carbon Nanotubes -Advanced Topics in the Synthesis, Structure, Properties and Applications*. Springer, Berlin Heidelberg, 2007.
- [7] S. Reich, C. Thomson, and J. Maultzsch. *Carbon Nanotubes - Basic Concepts and Physical Properties*. Springer, Berlin Heidelberg, 2003.
- [8] Avouris P. Dresselhaus M. S., Dresselhaus G. *Carbon Nanotubes -Synthesis, Structure, Properties, and Applications*. Springer, Berlin Heidelberg, 2001.
- [9] Robert Lee Petri. Fly-fishing. *Encyclopdia Britannica*, 2015.
- [10] Stephen Trimble. Lockheed martin reveals f-35 to feature nanocomposite structures. *Flight International*.
- [11] R. Martel, V. Derycke, C. Lavoie, J. Appenzeller, K. K. Chan, J. Tersoff, and Ph. Avouris. Ambipolar electrical transport in semiconducting single-wall carbon nanotubes. *Phys. Rev. Lett.*, 87:256805, Dec 2001.
- [12] S. J. Wind, J. Appenzeller, R. Martel, V. Derycke, and Ph. Avouris. Vertical scaling of carbon nanotube field-effect transistors using top gate electrodes. *Applied Physics Letters*, 80(20):3817–3819, 2002.
- [13] Thomas Rueckes, Kyounggha Kim, Ernesto Joselevich, Greg Y. Tseng, Chin-Li Cheung, and Charles M. Lieber. Carbon nanotube-based nonvolatile random access memory for molecular computing. *Science*, 289(5476):94–97, 2000.

BIBLIOGRAPHY

- [14] Sergei M. Bachilo, Michael S. Strano, Carter Kittrell, Robert H. Hauge, Richard E. Smalley, and R. Bruce Weisman. Structure-assigned optical spectra of single-walled carbon nanotubes. *Science*, 298(5602):2361–2366, 2002.
- [15] C. Köhler, T. Watermann, A. Knorr, and E. Malic. Microscopic study of temporally resolved carrier relaxation in carbon nanotubes. *Phys. Rev. B*, 84:153407, Oct 2011.
- [16] Olga A. Dyatlova, Christopher Köhler, Ermin Malic, Jordi Gomis-Bresco, Janina Maultzsch, Andrey Tsagan-Mandzhiev, Tobias Watermann, Andreas Knorr, and Ulrike Woggon. Ultrafast relaxation dynamics via acoustic phonons in carbon nanotubes. *Nano Letters*, 12(5):2249–2253, 2012.
- [17] Olga A. Dyatlova, Christopher Koehler, Peter Vogel, Ermin Malic, Rishabh M. Jain, Kevin C. Tvrdy, Michael S. Strano, Andreas Knorr, and Ulrike Woggon. Relaxation dynamics of carbon nanotubes of enriched chiralities. *Phys. Rev. B*, 90:155402, Oct 2014.
- [18] David J. Bergman and Mark I. Stockman. Surface plasmon amplification by stimulated emission of radiation: Quantum generation of coherent surface plasmons in nanosystems. *Phys. Rev. Lett.*, 90:027402, Jan 2003.
- [19] T.J. Echtermeyer, L. Britnell, P.K. Jasnós, A. Lombardo, R.V. Gorbachev, A.N. Grigorenko, A.K. Geim, A.C. Ferrari, and K.S. Novoselov. Strong plasmonic enhancement of photovoltage in graphene. *Nature Communications*, 2.
- [20] Mareen Glaeske and Antonio Setaro. Nanoplasmonic colloidal suspensions for the enhancement of the luminescent emission from single-walled carbon nanotubes. *Nano Research*, 6(8):593–601, 2013.
- [21] K. Kneipp, M. Moskovits, and H. Kneipp. *Surface-Enhanced Raman Scattering: Physics and Applications*. Springer, Berlin Heidelberg, 2006.
- [22] J. von Neumann. Wahrscheinlichkeitstheoretischer aufbau der quantenmechanik. *Nachrichten von der Gesellschaft der Wissenschaften zu Göttingen, Mathematisch-Physikalische Klasse*, 1927:245–272, 1927.
- [23] Ugo Fano. Density matrices as polarization vectors. *Rendiconti Lincei*, 6(2):123–130, 1995.
- [24] L. D. Landau. The damping problem in wave mechanics. *Z. Phys.*, 45.
- [25] F. Bloch. Nuclear induction. *Phys. Rev.*, 70:460–474, Oct 1946.
- [26] F. Rossi and T. Kuhn. Theory of ultrafast phenomena in photoexcited semiconductors. *Rev. Mod. Phys.*, 74:895–950, Aug 2002.
- [27] M. Kira and S. W. Koch. Many-body correlations and excitonic effects in semiconductor spectroscopy. *Progress in Quantum Electronics*, 30(5):155 – 296, 2006.

-
- [28] Marlan O. Scully and M. Suhail Zubairy. *Quantum Optics*. Cambridge University Press, 1997.
- [29] Wolfgang Pauli. *Pauli Lectures on Physics Volume 5: Wave Mechanics*. Dover Publ Inc, 2000.
- [30] H. Haken. *Quantenfeldtheorie des Festkörpers*. B. G. Teubner Stuttgart, 1973.
- [31] T. Kuhn. *Ladusträger fern vom Gleichgewicht*. Habilitation, 1992.
- [32] P. Ehrenfest. Bemerkung ueber die angenaeherte gueltigkeit der klassischen mechanik innerhalb der quantenmechanik. *Zeitschrift fuer Physik*, 45:455–457, Jul 1927.
- [33] Martin Schaarschmidt. *Theory of Light Propagation in Nano-Structured Materials and Semiconductors*. Phd Thesis TU Berlin, 2006.
- [34] H. Haug and S. W. Koch. *Quantum Theory of the Optical and Electronic Properties of Semiconductors*. World Scientific, 2009.
- [35] Ermin Malic, Torben Winzer, and Andreas Knorr. Efficient orientational carrier relaxation in optically excited graphene. *Applied Physics Letters*, 101(21):213110, 2012.
- [36] R. Zimmermann. Transverse relaxation and polarization specifics in the dynamical stark effect. *physica status solidi (b)*, 159(1):317–326, 1990.
- [37] Hartmut Haug and Stephan W. Koch. *Quantum theory of the optical and electronic properties of semiconductorss*. World Scientific, Berlin, 2004.
- [38] W.-K. Tse and S. Das Sarma. Energy relaxation of hot dirac fermions in graphene. *Phys. Rev. B*, 79:235406, Jun 2009.
- [39] M.S. Dresselhaus, G. Dresselhaus, and R. Saito. Physics of carbon nanotubes. *Carbon*, 33(7):883 – 891, 1995. Nanotubes.
- [40] S. Reich, J. Maultzsch, C. Thomsen, and P. Ordejón. Tight-binding description of graphene. *Phys. Rev. B*, 66:035412, Jul 2002.
- [41] N. W. Ashcroft and N. D. Mermin. *Solid State Physics*. Cengage Learning Emea, 1976.
- [42] P. R. Wallace. The band theory of graphite. *Phys. Rev.*, 71:622–634, May 1947.
- [43] V. Zólyomi and J. Kürti. First-principles calculations for the electronic band structures of small diametersingle-wall carbon nanotubes. *Phys. Rev. B*, 70:085403, Aug 2004.
- [44] D. Connétable, G.-M. Rignanese, J.-C. Charlier, and X. Blase. Room temperature peierls distortion in small diameter nanotubes. *Phys. Rev. Lett.*, 94:015503, Jan 2005.

BIBLIOGRAPHY

- [45] E. Malic. *Many-particle theory of optical properties of low-dimensional nanostructures - Dynamics in single-walled carbon nanotubes and semiconductor quantum dots*. PHD Thesis, TU Berlin, 2008.
- [46] Liu Yang, M. P. Anantram, Jie Han, and J. P. Lu. Band-gap change of carbon nanotubes: Effect of small uniaxial and torsional strain. *Phys. Rev. B*, 60:13874–13878, Nov 1999.
- [47] J. Maultzsch, S. Reich, C. Thomsen, H. Requardt, and P. Ordejón. Phonon dispersion in graphite. *Phys. Rev. Lett.*, 92:075501, Feb 2004.
- [48] S. Piscanec, M. Lazzeri, F. Mauri, A. C. Ferrari, and J. Robertson. Kohn anomalies and electron-phonon interactions in graphite. *Phys. Rev. Lett.*, 93:185503, Oct 2004.
- [49] M. Machón, S. Reich, H. Telg, J. Maultzsch, P. Ordejón, and C. Thomsen. Strength of radial breathing mode in single-walled carbon nanotubes. *Phys. Rev. B*, 71:035416, Jan 2005.
- [50] A. Grüneis, R. Saito, G. G. Samsonidze, T. Kimura, M. A. Pimenta, A. Jorio, A. G. Souza Filho, G. Dresselhaus, and M. S. Dresselhaus. Inhomogeneous optical absorption around the K point in graphite and carbon nanotubes. *Phys. Rev. B*, 67:165402, Apr 2003.
- [51] J. Jiang, R. Saito, and A. Gr. Optical absorption matrix elements in single-wall carbon nanotubes. *Carbon*, 42(15):3169 – 3176, 2004.
- [52] Hannah Funk. *Theorie der optischen Eigenschaften von Graphen*. Bachelor Thesis TU Berlin, 2011.
- [53] Ermin Malić, Matthias Hirschschulz, Frank Milde, Andreas Knorr, and Stephanie Reich. Analytical approach to optical absorption in carbon nanotubes. *Phys. Rev. B*, 74:195431, Nov 2006.
- [54] Hiroshi Ajiki and Tsuneya Ando. Electronic states of carbon nanotubes. *Journal of the Physical Society of Japan*, 62(4):1255–1266, 1993.
- [55] Ge G Samsonidze, AR Saito, DA Jorio, EMA Pimenta, Filho Souza, FA Gruneis, DG Dresselhaus, MS Dresselhaus, et al. The concept of cutting lines in carbon nanotube science. *Journal of nanoscience and nanotechnology*, 3(6):431–458, 2003.
- [56] S. Piscanec, M. Lazzeri, J. Robertson, A. C. Ferrari, and F. Mauri. Optical phonons in carbon nanotubes: Kohn anomalies, peierls distortions, and dynamic effects. *Phys. Rev. B*, 75:035427, Jan 2007.
- [57] J. Maultzsch, H. Telg, S. Reich, and C. Thomsen. Radial breathing mode of single-walled carbon nanotubes: Optical transition energies and chiral-index assignment. *Phys. Rev. B*, 72:205438, Nov 2005.

-
- [58] C. Manzoni, A. Gambetta, E. Menna, M. Meneghetti, G. Lanzani, and G. Cerullo. Inter-subband exciton relaxation dynamics in single-walled carbon nanotubes. *Phys. Rev. Lett.*, 94:207401, May 2005.
- [59] J. Jiang, R. Saito, Ge. G. Samsonidze, S. G. Chou, A. Jorio, G. Dresselhaus, and M. S. Dresselhaus. Electron-phonon matrix elements in single-wall carbon nanotubes. *Phys. Rev. B*, 72:235408, Dec 2005.
- [60] G. N. Ostojic, S. Zaric, J. Kono, M. S. Strano, V. C. Moore, R. H. Hauge, and R. E. Smalley. Interband recombination dynamics in resonantly excited single-walled carbon nanotubes. *Phys. Rev. Lett.*, 92:117402, 2004.
- [61] Y. Ma, J. Stenger, J. Zimmermann, S. M. Bachilo, R. E. Smalley, R. B. Weisman, and G. R. Fleming. Ultrafast carrier dynamics in single-walled carbon nanotubes probed by femtosecond spectroscopy. *J. Chem. Phys.*, 120(7):3368, 2004.
- [62] J.-P. Yang, M. M. Kappes, H. Hippler, and A.-N. Unterreiner. Femtosecond transient absorption spectroscopy of single-walled carbon nanotubes in aqueous surfactant suspensions: Determination of the lifetime of the lowest excited state. *Phys. Chem. Chem. Phys.*, 7:512–517, 2005.
- [63] Y. Z. Ma, M. W. Graham, and G. R. Fleming. Ultrafast exciton dephasing in semiconducting single walled carbon nanotubes. *Phys. Rev. Lett.*, 101:217402, 2008.
- [64] L. Lüer, G. Lanzani, J. Crochet, T. Hertel, J. Holt, and Z. V. Vardeny. Ultrafast dynamics in metallic and semiconducting carbon nanotubes. *Phys. Rev. B*, 80:205411, 2009.
- [65] M. W. Graham, T. R. Calhoun, A. A. Green, M. C. Hersam, and G. R. Fleming. Two-dimensional electronic spectroscopy reveals the dynamics of phonon-mediated excitation pathways in semiconducting single-walled carbon nanotubes. *Nano Letters*, 12(2):813–819, 2012.
- [66] *private communications with Olga A. Dyatlova*. 2014.
- [67] E. Malic, M. Hirschschulz, J. Maultzsch, S. Reich, and A. Knorr. Environmental influence on linear optical spectra and relaxation dynamics in carbon nanotubes. *Phys. Status Solidi (b)*, 246(11-12):2592–2597, 2009.
- [68] O. A. Dyatlova, J. Gomis-Bresco, E. Malic, H. Telg, J. Maultzsch, G. Zhong, J. Geng, and U. Woggon. Dielectric screening effects on transition energies in aligned carbon nanotubes. *Phys. Rev. B*, 85:245449, Jun 2012.
- [69] J. Maultzsch, R. Pomraenke, S. Reich, E. Chang, D. Prezzi, A. Ruini, E. Molinari, M. S. Strano, C. Thomsen, and C. Lienau. Exciton binding energies in carbon nanotubes from two-photon photoluminescence. *Phys. Rev. B*, 72:241402, Dec 2005.

BIBLIOGRAPHY

- [70] F. Wang, G. Dukovic, L. E. Brus, and T. F. Heinz. The optical resonances in carbon nanotubes arise from excitons. *Science*, 308(5723):838–841, 2005.
- [71] Ermin Malic, Matthias Hirtschulz, Frank Milde, Marten Richter, Janina Maultzsch, Stephanie Reich, and Andreas Knorr. Coulomb effects in single-walled carbon nanotubes. *physica status solidi (b)*, 245(10):2155–2158, 2008.
- [72] Ermin Malić, Matthias Hirtschulz, Frank Milde, Yang Wu, Janina Maultzsch, Tony F. Heinz, Andreas Knorr, and Stephanie Reich. Theory of rayleigh scattering from metallic carbon nanotubes. *Phys. Rev. B*, 77:045432, Jan 2008.
- [73] Ermin Malic, Janina Maultzsch, Stephanie Reich, and Andreas Knorr. Excitonic absorption spectra of metallic single-walled carbon nanotubes. *Phys. Rev. B*, 82:035433, Jul 2010.
- [74] Ermin Malic, Janina Maultzsch, Stephanie Reich, and Andreas Knorr. Excitonic rayleigh scattering spectra of metallic single-walled carbon nanotubes. *Phys. Rev. B*, 82:115439, Sep 2010.
- [75] Christopher Köhler, Tobias Watermann, and Ermin Malic. Relaxation dynamics via acoustic phonons in carbon nanotubes. *physica status solidi (b)*, 249(12):2483–2486, 2012.
- [76] Christopher Köhler, Tobias Watermann, and Ermin Malic. Time- and momentum-resolved phonon-induced relaxation dynamics in carbon nanotubes. *Journal of Physics: Condensed Matter*, 25(10):105301, 2013.
- [77] F. Prengel and E. Schöll. Delayed intersubband relaxation in quantum wires due to quantum kinetic coulomb scattering. *Phys. Rev. B*, 59:5806–5816, Feb 1999.
- [78] H. Khoa Ly, Christopher Köhler, Anna Fischer, Julia Kabuss, Felix Schlosser, Mario Schoth, Andreas Knorr, and Inez M. Weidinger. Induced surface enhancement in coral pt island films attached to nanostructured ag electrodes. *Langmuir*, 28(13):5819–5825, 2012.
- [79] Xiao Xia Han, Christopher Köhler, Jacek Kozuch, Uwe Kuhlmann, Lars Paasche, Arumugam Sivanesan, Inez M. Weidinger, and Peter Hildebrandt. Potential-dependent surface-enhanced resonance raman spectroscopy at nanostructured tio₂: A case study on cytochrome b5. *Small*, 9(24):4175–4181, 2013.
- [80] Ernst Schmutzer. *Relativitätstheorie aktuell - Ein Beitrag zur Einheit der Physik*. Teubner, 1996.
- [81] edited by E. Palik. *Handbook of Optical Constants of Solids*. Academic Press Inc, 1985.
- [82] David Pines and David Bohm. A collective description of electron interactions: Ii. collective vs individual particle aspects of the interactions. *Phys. Rev.*, 85:338–353, Jan 1952.
- [83] Mark Fox. *Optical Properties of Solids*. Oxford University Press, 2010.

-
- [84] P. Drude. Zur elektronentheorie der metalle. *Annalen der Physik*, 306(3):566–613, 1900.
- [85] Isaac Newton. *Philosophiae Naturalis Principia Mathematica*. Innys, Londini, editio tertia aucta emendata edition, 1726.
- [86] Eric Le Ru and Pablo Etchegoin. *Principles of Surface-Enhanced Raman Spectroscopy: and related plasmonic effects*. Elsevier, 2008.
- [87] R. H. Ritchie. Plasma losses by fast electrons in thin films. *Phys. Rev.*, 106:874–881, Jun 1957.
- [88] C. J. Powell and J. B. Swan. Origin of the characteristic electron energy losses in aluminum. *Phys. Rev.*, 115:869–875, Aug 1959.
- [89] E. A. Stern and R. A. Ferrell. Surface plasma oscillations of a degenerate electron gas. *Phys. Rev.*, 120:130–136, Oct 1960.
- [90] Jan Pomplun, Sven Burger, Lin Zschiedrich, and Frank Schmidt. Adaptive finite element method for simulation of optical nano structures. *physica status solidi (b)*, 244(10):3419–3434, 2007.
- [91] Hoang Khoa Ly. *Dissertation: Application of Surface Enhanced Raman Spectroscopy to Biological Systems*. TU Berlin, 2013.
- [92] M. Fleischmann, P.J. Hendra, and A.J. McQuillan. Raman spectra of pyridine adsorbed at a silver electrode. *Chemical Physics Letters*, 26(2):163 – 166, 1974.
- [93] Joel Gersten and Abraham Nitzan. Electromagnetic theory of enhanced raman scattering by molecules adsorbed on rough surfaces. *The Journal of Chemical Physics*, 73(7), 1980.
- [94] P. F. Liao and A. Wokaun. Lightning rod effect in surface enhanced raman scattering. *The Journal of Chemical Physics*, 76(1), 1982.
- [95] Poulomi Roy, Steffen Berger, and Patrik Schmuki. Tio₂ nanotubes: Synthesis and applications. *Angewandte Chemie International Edition*, 50(13):2904–2939, 2011.
- [96] Kaiyong Cai, Yanhua Hou, Yan Hu, Li Zhao, Zhong Luo, Yisong Shi, Min Lai, Weihua Yang, and Peng Liu. Correlation of the cytotoxicity of tio₂ nanoparticles with different particle sizes on a sub-200-nm scale. *Small*, 7(21):3026–3031, 2011.
- [97] Xiaotian Wang, Wensheng Shi, Guangwei She, and Lixuan Mu. Surface-enhanced raman scattering (sers) on transition metal and semiconductor nanostructures. *Phys. Chem. Chem. Phys.*, 14:5891–5901, 2012.

BIBLIOGRAPHY

- [98] Anthony Musumeci, David Gosztola, Tara Schiller, Nada M. Dimitrijevic, Vladimiro Mujica, Darren Martin, and Tijana Rajh. Sers of semiconducting nanoparticles (tio₂ hybrid composites). *Journal of the American Chemical Society*, 131(17):6040–6041, 2009. PMID: 19364105.
- [99] Tillmann Utesch, Murat Sezer, Inez M. Weidinger, and Maria Andrea Mroginski. Adsorption of sulfite oxidase on self-assembled monolayers from molecular dynamics simulations. *Langmuir*, 28(13):5761–5769, 2012. PMID: 22385217.
- [100] *Optical Data from Sopra SA* <http://www.sspectra.com.html>, accessed February, 2013. 2013.
- [101] E. Malic, C. Weber, M. Richter, V. Atalla, T. Klamroth, P. Saalfrank, S. Reich, and A. Knorr. Microscopic model of the optical absorption of carbon nanotubes functionalized with molecular spiropyran photoswitches. *Phys. Rev. Lett.*, 106:097401, Mar 2011.
- [102] Lisa J. Carlson, Sara E. Maccagnano, Ming Zheng, John Silcox, and Todd D. Krauss. Fluorescence efficiency of individual carbon nanotubes. *Nano Letters*, 7(12):3698–3703, 2007. PMID: 17997586.
- [103] Marcus Jones, Chaiwat Engtrakul, Wyatt K. Metzger, Randy J. Ellingson, Arthur J. Nozik, Michael J. Heben, and Garry Rumbles. Analysis of photoluminescence from solubilized single-walled carbon nanotubes. *Phys. Rev. B*, 71:115426, Mar 2005.
- [104] Sang-Yong Ju, William P. Kopcha, and Fotios Papadimitrakopoulos. Brightly fluorescent single-walled carbon nanotubes via an oxygen-excluding surfactant organization. *Science*, 323(5919):1319–1323, 2009.
- [105] Guosong Hong, Scott M. Tabakman, Kevin Welsher, Hailiang Wang, Xinran Wang, and Hongjie Dai. Metal-enhanced fluorescence of carbon nanotubes. *Journal of the American Chemical Society*, 132(45):15920–15923, 2010. PMID: 20979398.
- [106] Randy K. Wang, Wei-Chiang Chen, Daisy K. Campos, and Kirk J. Ziegler. Swelling the micelle core surrounding single-walled carbon nanotubes with water-immiscible organic solvents. *Journal of the American Chemical Society*, 130(48):16330–16337, 2008. PMID: 18998688.
- [107] Mareen Glaeske and Antonio Setaro. Effect of hybrid isolation on the luminescence enhancement of carbon nanotubegold nanorod composites. *physica status solidi (b)*, 2014.
- [108] *private communications with A. Setaro, figure displaying experimental findings is courtesy of A. Setaro.* 2014.
- [109] N. Tzoar and J. I. Gersten. Theory of electronic band structure in intense laser fields. *Phys. Rev. B*, 12:1132–1139, Aug 1975.

- [110] Jaebeom Lee, Pedro Hernandez, Jungwoo Lee, Alexander O. Govorov, and Nicholas A. Kotov. Exciton-plasmon interactions in molecular spring assemblies of nanowires and wavelength-based protein detection. *Nature Materials*, 6(291):1476–1122, 2007.
- [111] H. Schulz. *Physik mit Bleistift, Das analytische Handwerkzeug der Naturwissenschaftler*. Harri Deutsch, 2006.